

**Advances in Autonomous Ground Traverses of the Earth's Polar Regions**

A Thesis  
Submitted to the Faculty  
in partial fulfillment of the requirements for the  
degree of

Doctor of Philosophy

in

Engineering Sciences

by Austin Lines

Thayer School of Engineering  
Guarini School of Graduate and Advanced Studies  
Dartmouth College  
Hanover, New Hampshire

November 2020

Examining Committee:

Chairman \_\_\_\_\_  
Laura Ray, Ph.D.

Member \_\_\_\_\_  
Mary Albert, Ph.D.

Member \_\_\_\_\_  
James Lever, Ph.D.

Member \_\_\_\_\_  
Minh Phan, Ph.D.

Member \_\_\_\_\_  
Sally Shoop, Ph.D.

---

F. Jon Kull, Ph.D.  
Dean of Guarini School of Graduate and Advanced Studies



# ABSTRACT

Ground-based measurements of the Arctic and Antarctica are critical in validating data from satellite and airborne sensors. The expense, logistics, and danger of collecting these data via manned traverses mean that the scope and frequency of these traverses is limited. While the concept of replacing manned traverses with automated rovers has been shown to be an alternative, several improvements need to be made to render robots as a viable replacement for human operated vehicles in this role. This thesis focuses on three crucial advances in automated ground traverses. The first improvement is in processing large sets of ground penetrating radar (GPR) data collected on long distance traverses. Typically, GPR data has been analyzed using manual layer picking techniques which is time consuming and subject to human bias and error. A hybrid layer picking method was developed that allows for automated tracing of layers of interest, with human input only required for correcting areas of poor quality data. The second area of improvement is in modifying the tractive element design of the robot to allow for maximum mobility in the majority of snowpack conditions using existing terramechanics models. This work resulted in new wheels for a robot prototype, and these wheels have been shown to enhance mobility on snow. The final focus of improvement is on incipient immobilization detection in real time. Models of the rover's motors' operating points were developed from data collected from a suite of proprioceptive sensors on a rover driven on unmodified snow. Clear separation between nominal mobility and nascent stages of immobilization allowed for a multiple model estimation (MME) algorithm to be utilized to preemptively warn of the loss of mobility. The parallel development of a truth model allowed for this new detection algorithm's effectiveness to be assessed on simulations of conditions outside those that were directly tested with the rover *in situ*.

## Acknowledgements

First, I would like to acknowledge that this work was supported by a NASA EPSCoR grant, award number NNX15AM80A, and a grant from the NSF's program in the division of Civil, Mechanical and Manufacturing Innovation (CMMI) for Dynamics, Control and System Diagnostics (DCSD), award number 1824687.

Second, I would like to express my appreciation for the people that directly impacted this work. My advisor, Dr. Laura Ray, provided invaluable guidance, support, and encouragement throughout my time at the Thayer School of Engineering. Her expansive knowledge of the field and her innovative ideas helped drive all aspects of this project. I also owe a huge debt of gratitude to my lab partner, Joshua Elliott, who recruited me to Dartmouth, had the initial idea to build a new rover and name it *FrostyBoy*, and who has helped me in all aspects of this endeavor, from soldering every connector to helping to deploy the robot at field sites around the world. I would also like to thank my committee members, Dr. Mary Albert, Dr. James Lever, Dr. Sally Shoop and Dr. Minh Phan for their advice and suggestions for my thesis.

Finally, on a more personal note, I would like to recognize my partner, Valerie, who inspires me every day, and my father David, my mother Lori, and my brother Eric, for their ceaseless support. Thank you.

# Contents

<b>1</b>	<b>Introduction</b>	<b>1</b>
1.1	Background and Motivation . . . . .	1
1.2	Scope of Work . . . . .	3
1.3	Contributions . . . . .	5
<b>2</b>	<b>Ground Penetrating Radar</b>	<b>7</b>
2.1	Introduction . . . . .	7
2.2	Background . . . . .	9
2.3	Methods . . . . .	9
2.3.1	Data . . . . .	9
2.3.2	Data Processing . . . . .	10
2.3.3	Layer Picking System . . . . .	11
2.4	Results . . . . .	13
2.5	Conclusion . . . . .	15
<b>3</b>	<b>Tractive Element Design</b>	<b>17</b>
3.1	Introduction . . . . .	17
3.2	Background . . . . .	18
3.3	Sinkage . . . . .	20
3.4	Traction . . . . .	25
3.5	Balance of Forces . . . . .	29
3.6	Other Factors . . . . .	30
3.7	New Wheel Design . . . . .	32
<b>4</b>	<b>Mobility Prediction</b>	<b>41</b>
4.1	Introduction . . . . .	41
4.2	Existing Methods . . . . .	42
4.2.1	Terrain Models to Predict Mobility . . . . .	42
4.2.2	Drawbacks of Terrain Models . . . . .	46
4.2.3	Other Methods . . . . .	48
4.3	New Mobility Prediction Method . . . . .	49

---

Chapter 2 is a copy of [1] with minor edits

<b>5 Methodology and Findings</b>	<b>51</b>
5.1 Introduction . . . . .	51
5.2 Instrumentation . . . . .	51
5.3 Data Collection . . . . .	54
5.4 Results . . . . .	57
5.5 Summary . . . . .	67
<b>6 Truth Model Development</b>	<b>69</b>
6.1 Introduction . . . . .	69
6.2 Modeling Approach . . . . .	70
6.3 Model Development . . . . .	71
6.3.1 Dynamics . . . . .	71
6.3.2 Motor Model . . . . .	74
6.3.3 Terrain Model . . . . .	77
6.3.4 Simulation Process . . . . .	83
6.4 Simulating Immobilizations . . . . .	84
6.5 Summary . . . . .	95
<b>7 Incipient Immobilization Detection</b>	<b>98</b>
7.1 Introduction . . . . .	98
7.2 Hypothesis Generation . . . . .	99
7.3 Bayesian Multiple Model Estimation Method . . . . .	102
7.4 Detection Results . . . . .	106
7.4.1 Collected Data . . . . .	106
7.4.2 Simulated Data . . . . .	111
7.5 Summary . . . . .	118
<b>8 Conclusion</b>	<b>120</b>
<b>A Detection Results - Collected Data</b>	<b>123</b>
A.1 Event 1-1 . . . . .	124
A.2 Event 1-2 . . . . .	125
A.3 Event 1-3 . . . . .	126
A.4 Event 1-4 . . . . .	127
A.5 Event 1-5 . . . . .	128
A.6 Event 1-6 . . . . .	129
A.7 Event 1-7 . . . . .	130
A.8 Event 1-8 . . . . .	131
A.9 Event 1-9 . . . . .	132
A.10 Event 2-1 . . . . .	133
A.11 Event 2-2 . . . . .	134
A.12 Event 2-3 . . . . .	135
A.13 Event 2-4 . . . . .	136
A.14 Event 2-5 . . . . .	137
A.15 Event 2-6 . . . . .	138

A.16 Event 2-7 . . . . .	139
A.17 Event 2-8 . . . . .	140

**B Code Repository on GitHub** **141**

# List of Tables

3.1	Pressure-sinkage terrain parameters for three different types of snow for the Bekker model. Parameters for Bekker 1 and 3 are from Wong [2] and those for Bekker 2 are from Harrison [3]. . . . .	23
3.2	Pressure-sinkage terrain parameters for five different snows using the Preston-Thomas model [4]. Parameters for Preston 1 were measured near Summit Station, Greenland [5] and parameters for Preston 2 - 5 were measured in Lebel-sur-Quévillon, Québec, Canada (see Ch. 5). . . . .	24
3.3	Parameters used to compare a low stiffness, poorly bonded snow to a high stiffness, well bonded snow. The well bonded, high stiffness snow uses the well bonded shear stress-shear displacement model (3.8) and the Bekker pressure-sinkage model (3.2). The poorly bonded, low stiffness snow uses the poorly bonded shear stress-shear displacement model (3.9) and the Preston-Thomas pressure-sinkage model (3.6). Cells with no number mean that the parameter is not used in the models that describe this type of snow.	29
5.1	Comparison of the best-fit Preston-Thomas (3.6) and Bekker (3.2) pressure-sinkage parameters and coefficients of determination collected with the GP at test site #2. . . . .	62
6.1	Values for parameters measured from <i>FrostyBoy</i> and used in the truth model to simulate its behavior. . . . .	72
6.2	Final terrain parameters used to simulate low stiffness, poorly bonded, low cohesion snow. . . . .	82
7.1	Results from applying the MME algorithm on data collected from immobilization events in Lebel-sur-Quévillon. The first number of the event number corresponds to the test site. The "early" entries mean that an immobilization was flagged by the algorithm before the start of the immobilization event that actually resulted in the rover's complete loss of mobility and are not included in the results' statistics. . . . .	107

# List of Figures

2.1	Map of the GreenTrACS 2017 route. The section analyzed with ALPS lies between the sites of Cores 13 and 14. . . . .	10
2.2	10 km segment of a radargram acquired from 400 MHz antenna before filtering (left) and after filtering (right). . . . .	11
2.3	Control panel of ALPS . . . . .	12
2.4	Approximately 35 km of 400 MHz data with manual (dotted green) and ALPS (solid red) traces of IRHs. . . . .	14
3.1	Forward and backward flow of soil beneath a driven wheel [2]. . . . .	21
3.2	Stress distribution below a rigid wheel in deformable terrain [6]. . . . .	22
3.3	Range of pressure vs. sinkage profiles obtained in snow. . . . .	25
3.4	Comparison of <i>well bonded</i> (3.8) and <i>poorly bonded</i> (3.9) snow traction models for the two types of snow defined by the parameters in Table 3.3. . .	28
3.5	Logarithmic spiral curve that approximates additional sinkage due to slip [7].	31
3.6	Modeled decrease in compaction resistance of a single wheel with changes in the wheel's dimensions. Wheel width, $b$ , increases from 0.1 m to 0.4 m. Radius, $r_w$ , increases from 0.2 m to 0.5 m. All other variables, including the assumed 60 kg mass of the rover, are kept constant. . . . .	34
3.7	Effect of changing wheel dimensions on resistance torque in two different snow types. In both figures, the wheel width, $b$ , was increased from 0.1 m to 0.5 m and the wheel radius, $r_w$ , was increased from 0.2 m to 0.5 m. Note that the x-axis scale is reversed, with left to right corresponding to a decrease in sinkage and an increase in wheel dimensions. Three different robot masses, $m$ , were evaluated, seeing as changing wheel radius or wheel width would impact the rover's mass. . . . .	35
3.8	Effect of changing wheel dimensions on the <i>mobility efficiency</i> factor (draw-bar pull per torque required [N/Nm]) in two different snow types. In both figures, the wheel width, $b$ , was increased from 0.1 m to 0.5 m and the wheel radius, $r_w$ , was increased from 0.2 m to 0.5 m. Note that the x-axis scale is reversed, with left to right corresponding to a decrease in sinkage and an increase in wheel dimensions. Three different robot masses, $m$ , were evaluated, seeing as changing wheel radius or wheel width would impact the rover's mass. . . . .	36
3.9	Prototype of new wheel design with a 4x increase in wheel width compared to previous snow rovers. . . . .	38

3.10	Sinkage comparison of snowmobile track (from top of photo to bottom left), <i>FrostyBoy</i> wheel track (from right to left side of photo - double wide), and a person's boot track (lower right). The boot sinkage is estimated to be about 3 to 4 cm, the snowmobile track $\sim$ 1 cm, and the <i>FrostyBoy</i> wheels appear to sink less than the snowmobile. While this appears to be high stiffness snow, the relative sinkages serve as a sinkage test to understand <i>FrostyBoy</i> 's surface pressure. . . . .	39
4.1	Flow pattern beneath driven wheel at 100% slip [2]. . . . .	47
4.2	Immobilization of <i>Cool Robot</i> due to slip-sinkage effect. . . . .	48
5.1	<i>FrostyBoy</i> shown in Greenland during the 2018 field season in the dry snow zone towing a sled carrying solar panels and a GPR unit. . . . .	53
5.2	Labeled drawing of Ground Pounder device to measure pressure-sinkage profile. . . . .	54
5.3	Body-fixed reference frame convention, with $x$ , $y$ , and $z$ defining the longitudinal, lateral, and vertical axes, respectively, and $\psi$ , $\beta$ , and $\rho$ defining the yaw, pitch, and roll angles. . . . .	58
5.4	Data from a typical immobilization event, with the top graph showing longitudinal velocity of the rover, $v_x$ , and the four subsequent graphs showing wheel speed, $\omega$ , wheel torque, $T$ , and wheel slip, $i$ , for each of the four wheels. This example clearly shows that the front left and rear right wheels stalled and the front right and rear left wheels reached 100% slip. . . . .	60
5.5	Top view of <i>FrostyBoy</i> after becoming immobilized at test site #2. Data for this immobilization are presented in Fig. 5.4. Note the build up of excavated snow behind the front right and rear left wheels. . . . .	61
5.6	Side view of <i>FrostyBoy</i> after becoming immobilized at test site #2. Data for this immobilization are presented in Fig. 5.4. Note the front of the robot (antenna side) is clearly pitched up relative to the horizon line. . . . .	62
5.7	Pressure-sinkage data from the Ground Pounder collected at test site #2 in Lebel-sur-Quévillon, with the best-fit Preston-Thomas curve (3.6) shown for each data set. Data sets 1 and 2 are taken $\sim$ 10 meters apart before the immobilization trials started. Data sets 3 and 4 are taken immediately after an immobilization event, just to the left and right sides of the front rover wheels. The Preston-Thomas curve parameters and measures of fit are presented in Table 5.1. . . . .	63
5.8	Recorded GPS track of the rover making nine passes over the same $\sim$ 16 m stretch of terrain at the wooded test site (#1) in Lebel-sur-Quévillon. An outline drawing of <i>FrostyBoy</i> is shown for reference. . . . .	64
5.9	Comparison of torques for the first and ninth pass over the same terrain at test site #1. Multiple passes in the same tracks are shown not to significantly reduce the torque required in the loose, unconsolidated, and low stiffness snow with ambient temperatures remaining below 0° C. . . . .	65

5.10 Comparison of torques for the first and second pass in the same tracks on the lake (test site #2) after ambient temperatures were approaching 0° C. This shows the clear reduction of resistance torque due to compaction of the terrain from one pass to the next. This trend can even be seen by comparing the front wheel torques to the rear wheel torques of the first pass. . . . .	66
6.1 Robot body-fixed coordinate conventions and relevant dimensions. . . . .	72
6.2 Diagram showing conventions and variables involved in calculating the normal force for front and rear axles. . . . .	74
6.3 These plots show how the motor operating points move in open-loop and closed-loop modes. <b>(a)</b> In open-loop mode, the applied voltage is fixed and the motor operating point moves along the torque-speed curve defined by this voltage. This figure shows an example if the applied voltage is set to 18V (38% of the 48V design voltage) and the load on the wheel varies. The torque-speed curves at 12V, 15V, 21V, and 24V are shown for reference. <b>(b)</b> In closed-loop mode, the motor controller changes the applied voltage (represented by the color gradient in the arrow) to maintain a constant speed over a wide range of loads. In this figure, a speed setpoint of ~3 rad/sec is being maintained. . . . .	75
6.4 Comparison of the calculated torque-speed slope with measured data points during steady-state operation of <i>FrostyBoy</i> . This data is pulled from a run where the rover was driving on the lake (test site #2), tracking relatively straight, with all four motors sent the same commanded voltage of 18V. . . . .	76
6.5 Sensitivity study to understand the effects of cohesion, $c$ , angle of internal friction, $\phi$ , and shear deformation modulus, $K_s$ , on drawbar pull and torque for a single wheel. The data points, repeated on each plot, are from measurements taken during steady-state operation of <i>FrostyBoy</i> on the lake (test site #2). Note that plots (a) and (b) have differently scaled y-axes than the other plots due to the significant impact of the cohesion parameter on drawbar pull and torque. . . . .	78
6.6 Modified slip-sinkage factor. . . . .	81
6.7 Curves generated using final set of terrain parameters that roughly approximate measured data. . . . .	82
6.8 Separation of high torque and high slip operating points during immobilizations from those during nominal steady-state mobility. The dots represent nominal mobility, the circles show divergence from nominal mobility in the direction of high slip and lower torque, and the diamonds demonstrate divergence from nominal mobility in the direction of low slip and higher torque. The colors are used to denote from which of the four wheels the data point was measured. . . . .	85
6.9 A typical example of a wheel's sinkage after an immobilization event. . . . .	86
6.10 Simulation of abrupt increase in $k$ at $t = 4$ seconds for the front left and rear right wheels. . . . .	88
6.11 Simulation of abrupt decrease in $c$ at $t = 4$ seconds for the front right and rear left wheels. . . . .	89

6.12	Simulation of abrupt increase in $k$ at $t = 4$ seconds for the front left and rear right wheels, with excavation considered for the front right and rear left wheels. . . . .	92
6.13	Simulation of varying terrain causing immobilization, with $k$ taking on values based on a random walk model, shown in the bottom plot. . . . .	94
6.14	Example of a roll-compliant rover becoming immobilized during a turn due to excessive slip, evidenced by the snow buildup behind the right side wheels and the deep ruts created by the left side wheels. . . . .	96
7.1	Plots of the hypothesis values to show separability of model values during nominal, steady-state operation and during an immobilization. . . . .	101
7.2	Longitudinal velocity and each wheel's speed, applied torque, and slip shown for Event 1-7. The first black vertical band marks the start of the immobilization, the second black vertical band indicates when the vehicle has become fully immobilized, with the dashed red line showing the time of detection. All immobilization events from Lebel-sur-Quévillon can be found in Appendix A. . . . .	108
7.3	Simulation and detection of an immobilization caused by varying terrain parameters $k$ and $c$ , with motors in open-loop speed control. . . . .	112
7.4	Simulation and detection of an immobilization with motors in closed-loop speed control. The variation of terrain parameters $k$ and $c$ are identical to those presented in Fig. 7.3. . . . .	114
7.5	Simulation of a turning robot that becomes immobilized during the turn. . .	116
7.6	Simulation of a turning robot, commanded straight once incipient immobilization is detected. The same terrain variability was introduced into the simulation as was for Fig. 7.5. . . . .	117
7.7	X and Y position of the rover tracked for turning simulations with and without immobilization detection. . . . .	118

# Nomenclature

## Ground Penetrating Radar Variables

Variable	Description	Units
$h$	Offset from center of shift window, in number of samples	-
$H$	Shift window - total number of samples over which the search window, $N$ , will be shifted	-
$i$	Center of search window's sample number	-
$n$	Current sample number being evaluated	-
$N$	Search window - total number of samples over which the differences will be summed and averaged	-
$P$	Peak window - total number of samples within which to search for max value	-
$R_{ASDF}$	Cost function value of average square difference function	-
$s$	Adjacent trace number, to the initially selected trace, $x$	-
$x$	Initially selected trace number	-

## Terramechanics and Immobilization Detection Variables

Variable	Description	Units
$a$	Hypothesis number	-
$A_{imm}$	Number of immobilization hypotheses	-
$A_{nom}$	Number of nominal mobility hypotheses	-
$A_{total}$	Sum of number of immobilization and nominal mobility hypotheses	-
$b$	Wheel width	m
$B_\omega$	Mechanical damping constant	Nm/(rad/s)
$c$	Cohesion	kPa
$c_1$	Coefficient 1 used to determine location of $\theta_m$	-
$c_2$	Coefficient 2 used to determine location of $\theta_m$	-
$c_q$	Cohesion, varying along the longitudinal axis of motion according to a discrete random walk model	kPa
$d_f$	Distance from center of mass to front axle	m
$d_r$	Distance from center of mass to rear axle	m
$F_x$	Drawbar pull	N

$F_{xfl}$	Drawbar pull of front left wheel	N
$F_{xfr}$	Drawbar pull of front right wheel	N
$F_{xrl}$	Drawbar pull of rear left wheel	N
$F_{xrr}$	Drawbar pull of rear right wheel	N
$F_z$	Normal force on wheel	N
$F_{zf}$	Total normal force on both wheels of front axle	N
$F_{zfl}$	Normal force on front left wheel	N
$F_{zfr}$	Normal force on front right wheel	N
$F_{zr}$	Total normal force on both wheels of rear axle	N
$F_{zrl}$	Normal force on rear left wheel	N
$F_{zrr}$	Normal force on rear right wheel	N
$g$	Acceleration due to gravity	$\text{m/s}^2$
$h$	Height of center of mass above axles	m
$\hat{h}$	Grouser height normalized to wheel radius	m
<b>H</b>	State space output matrix	-
<b>H</b>	Measurement model matrix	-
$i$	Slip ratio	-
$I_{zz}$	Moment of inertia of rover about the z-axis at its center of mass	$\text{kg m}^2$
$I_\omega$	Wheel moment of inertia about its center of rotation	$\text{kg m}^2$
$j$	Shear displacement	m
$k$	Terrain stiffness	$\text{kPa/m}$
$k_c$	Cohesive modulus, Bekker pressure-sinkage model	$\text{kN/m}^{n+1}$
$k_q$	Terrain stiffness, varying along the longitudinal axis of motion according to a discrete random walk model	$\text{kPa/m}$
$k_\phi$	Friction modulus, Bekker pressure-sinkage model	$\text{kN/m}^{n+2}$
$K_c$	Cohesive component of soil bearing capacity factor	-
$K_r$	Ratio of the residual shear stress to the maximum shear stress, well bonded shear stress-shear displacement model	-
$K_s$	Shear deformation modulus, poorly bonded shear stress-shear displacement model	m
$K_\gamma$	Specific weight component of soil bearing capacity factor	-
$K_\omega$	Shear displacement at maximum shear stress, well bonded shear stress-shear displacement model	m
<b>K</b>	Kalman filter gain	-
$m$	Mass of rover	kg
$M_{res}$	Restoring moment constant	$\text{Nm}/(\text{rad/s})$
$n$	Exponent, modifying sinkage in pressure-sinkage equations	-
$n_c$	Noise parameter defining the random walk model of the cohesion variable	$\text{kPa/m}$
$n_g$	Number of grousers	-
$n_k$	Noise parameter defining the random walk model of the terrain stiffness variable	$\text{kPa/m}^2$
$N_c$	Cohesive bearing capacity factor	-

$N_\gamma$	Specific weight bearing capacity factor	-
$p$	Pressure	kPa
$\mathbf{P}^-$	<i>A priori</i> state estimate covariance matrix	-
$\mathbf{P}^+$	<i>Posteriori</i> state estimate covariance matrix	-
$q$	Distance step number for random walk models	-
$\mathbf{Q}$	Process disturbance covariance matrix	-
$r_w$	Wheel radius	m
$\mathbf{r}$	Measurement residual vector	-
$R_b$	Bulldozing resistance force	N
$R^2$	Coefficient of determination for best-fit curve	-
$\mathbf{R}$	Measurement noise covariance matrix	-
$s$	Time step number in discrete state space model	-
$S$	Slip-sinkage coefficient	-
$\mathbf{S}$	Residual covariance matrix	-
$t$	Time	s
$t_w$	Track width	m
$T$	Torque applied by wheel	Nm
$T_{fl}$	Torque applied by front left wheel	Nm
$T_{fr}$	Torque applied by front right wheel	Nm
$T_{rl}$	Torque applied by rear left wheel	Nm
$T_{rr}$	Torque applied by rear right wheel	Nm
$T_r$	Resistive torque	Nm
$T_{rfl}$	Resistive torque applied by terrain to front left wheel	Nm
$T_{rfr}$	Resistive torque applied by terrain to front right wheel	Nm
$T_{rll}$	Resistive torque applied by terrain to rear left wheel	Nm
$T_{rrr}$	Resistive torque applied by terrain to rear right wheel	Nm
$\mathbf{u}$	Input vector	-
$v_L$	Velocity of left wheels along longitudinal axis of motion	m/s
$v_R$	Velocity of right wheels along longitudinal axis of motion	m/s
$v_x$	Velocity along longitudinal axis of motion	m/s
$\dot{v}_x$	Acceleration along longitudinal axis of motion	$m/s^2$
$W$	Weight on each wheel	N
$x$ -axis	Longitudinal axis of motion	m
$\mathbf{x}$	State vector	-
$\hat{\mathbf{x}}^-$	<i>A priori</i> state estimate	-
$\hat{\mathbf{x}}^+$	<i>Posteriori</i> state estimate	-
$\Delta x$	Step size of random walk model for both the terrain stiffness and cohesion variables	m
$y$ -axis	Lateral axis of motion	m
$\mathbf{y}$	Output vector	-
$z$	Sinkage, distance from terrain surface to BDC of wheel	m
$z_0$	Sinkage, without taking into account effect of slip-sinkage	m
$z_{actual}$	Sinkage, taking into account effect of slip-sinkage	m
$z_f$	Sinkage of front axle wheels	m
$z_m$	Maximum sinkage, Preston-Thomas pressure-sinkage model	m

$z_r$	Sinkage of rear axle wheels	m
$z_t$	Depth of transition point of forward region and rear region flow regimes	m
$\hat{z}$	Sinkage normalized to wheel radius	m
$z\text{-axis}$	Vertical axis of motion	m
$\mathbf{z}$	Measurement vector	-
$\Delta z$	Additional sinkage due to slip	m
$\beta$	Pitch	radians
$\Gamma$	State space input matrix	-
$\gamma$	Specific weight of snow or soil	kN/m <sup>3</sup>
$\theta$	Angle from BDC of wheel	radians
$\theta_1$	Angle from BDC of wheel to surface of the terrain in front region	radians
$\theta_2$	Angle from BDC of wheel to where wheel exits the terrain in rear region	radians
$\theta_m$	Angle from BDC of wheel at which the pressure is at its maximum	radians
$\lambda$	Wheel sinkage ratio	-
$\Lambda$	State space disturbance matrix	-
$\mu$	Hypothesis matrix	-
$\xi$	Wheel nominal mobility value	-
$\Xi$	Wheel pairing nominal mobility value	-
$\rho$	Roll	radians
$\sigma$	Normal stress	kPa
$\tau$	Shear stress	kPa
$\phi$	Angle of internal friction	radians
$\Phi$	State space system matrix	-
$\psi$	Yaw	radians
$\dot{\psi}$	Yaw rate	radians/s
$\ddot{\psi}$	Yaw angular acceleration	radians/s <sup>2</sup>
$\omega$	Angular wheel speed	radians/s
$\omega_{fl}$	Angular wheel speed of front left wheel	radians/s
$\omega_{fr}$	Angular wheel speed of front right wheel	radians/s
$\omega_{rl}$	Angular wheel speed of rear left wheel	radians/s
$\omega_{rr}$	Angular wheel speed of rear right wheel	radians/s
$\dot{\omega}_{fl}$	Angular wheel acceleration of front left wheel	radians/s <sup>2</sup>
$\dot{\omega}_{fr}$	Angular wheel acceleration of front right wheel	radians/s <sup>2</sup>
$\dot{\omega}_{rl}$	Angular wheel acceleration of rear left wheel	radians/s <sup>2</sup>
$\dot{\omega}_{rr}$	Angular wheel acceleration of rear right wheel	radians/s <sup>2</sup>

## Abbreviations

ALPS	Average square difference function Layer Picking System
ASDF	Average Square Difference Function

ATV	All-Terrain Vehicle
BDC	Bottom Dead Center
BLDC	Brushless Direct Current (motor)
CAD	Computer Aided Design
CPR	Counts Per Revolution
CVA	Canonical Variate Analysis
DEM	Digital Elevation Model
DTKF	Discrete Time Kalman Filter
EKBF	Extended Kalman-Bucy Filter
ERDC	Engineer Research and Development Center
FEA	Finite Element Analysis
FIR	Finite Impulse Response
GP	Ground Pounder
GPR	Ground Penetrating Radar
GreenTrACS	Greenland Traverse for Accumulation and Climate Studies
GSSI	Geophysical Survey Systems, Inc.
ICESat	Ice, Cloud, and land Elevation Satellite
IDeA	Immobilization Detection Algorithm
IIR	Infinite Impulse Response
IMU	Inertial Measurement Unit
INS	Inertial Navigation System
IRH	Internal Reflection Horizon
LiDAR	Light Detection and Ranging
MCSA	Motor Current Signature Analysis
MER	Mars Exploration Rover
MME	Multiple Model Estimation
NASA	National Aeronautics and Space Administration
NATO	North Atlantic Treaty Organization
NRMM	NATO Reference Mobility Model
NSF	National Science Foundation
NWVPM	Nepean Wheeled Vehicle Performance Model
OIB	Operation Ice Bridge
PI	Proportional Integral (controller)
SVM	Support Vector Machine
TARDEC	Tank Automotive Research, Development, and Engineering Center
USB	Universal Serial Bus
WMR	Wheeled Mobile Robot

# **Chapter 1**

## **Introduction**

### **1.1 Background and Motivation**

The ice sheets of Greenland and Antarctica have a significant impact on the overall global climate and serve as an indicator of trends in climate change. Measurements of conditions in these remote areas, such as albedo, snow temperature, and mass balance, are necessary to develop and refine climate models and predict sea-level rise [8] [9]. Due to the difficulty and expense of accessing these areas, a large portion of data is collected using satellite or aircraft-mounted sensors. These methods allow for effective spatiotemporal variation in measurements with minimal human involvement. In many cases, ground-based measurements are still required to validate and calibrate the remote sensors. These ground-based measurements provide higher resolution data or can continue sensing either when cloud cover occludes certain measurements or when weather prevents an aircraft from flying. For example, NASA's Ice, Cloud, and Land Elevation Satellite (ICESat), while having very fine resolution and wide coverage, still requires ground-based elevation measurements for validation [10]. Similarly, ground penetrating radar (GPR) data collected during NASA's airborne Operation Ice Bridge (OIB) campaign has a lower along-track resolution than a ground-based GPR unit [11]. Matching the spatial and temporal coverage of remote sens-

ing proves difficult with ground-based measurements. Typically ground-based measurements are *in situ* point measurements with high temporal resolution, as is the case for the automatic weather stations throughout Greenland and Antarctica, continuously collecting meteorological data. Ground-based measurements are also taken during traverses by scientists collecting data over hundreds, if not thousands of kilometers. However, the high cost, extensive logistics, and serious danger of operating a mobile camp in such harsh conditions mean that these traverses occur infrequently. NASA's 750 km traverse around the south pole at 88 degrees latitude to validate ICESat only happens once a year [12]. The Greenland Traverse for Accumulation and Climate Studies (GreenTrACS), while collecting over 2000 km of GPR data each year, only operated for two years [13] [14]. Therefore, a means of collecting ground-based measurements with high spatial and temporal resolution in the Arctic and in Antarctica would improve the scientific knowledge of these regions and help in monitoring and predicting changes in the global climate.

Through NASA and NSF funded projects, previous Dartmouth students have shown that autonomous rovers, built for traversing snow, can serve as an ideal platform for this continual collection of data over long transects or in grid patterns of a significant size. With the ability to tow a low friction sled over the snow surface, these robots can be outfitted with a suite of instruments, similar to the instrumented sleds pulled by snowmobiles or snowcats on science traverses. However, removing humans from these expeditions removes the need for towing food, water, camping equipment, and survival gear. It also improves route following error, increases the number of hours of data collection per day, and eliminates human exposure to crevasse and cold weather danger. Two robots have been built and deployed to both Greenland and Antarctica to prove out this concept. *Cool Robot* was built through a National Science Foundation Small Grant for Exploratory Research. This 66 kg robot, with an independent electric motor for each of its four wheels, runs on lithium-ion batteries that are charged by a 5-solar-panel box surrounding the chassis [15]. It was designed to drive and collect data continuously at extreme latitudes on days with 24 hours of

solar insolation. The functionality of this robot was first proven in 2005 when the robot performed a five and an eight hour driving test on the ice sheet around Summit Station, Greenland [16]. In 2013, *Cool Robot* completed over 200 km of autonomous operation, with its batteries being recharged by the solar panel array, while towing a 900 MHz GPR antenna and an air-sampling instrument [15]. The other robot, *Yeti*, was developed by Dartmouth students under a NASA Jet Propulsion Lab Future Rocket Scientists sponsorship. This rover, while still a four-wheel drive, battery powered, electric motor, autonomous robot, was slightly heavier than *Cool Robot*, with a mass of 77 kg. It was also able to handle rougher terrain and operate in higher winds due to its central articulation that allows rotation about the roll axis and by being exclusively battery powered, with no integrated solar panels for recharging during operation [17]. *Yeti*'s purpose is to tow a heavier GPR setup (around 68 kg) on 15 to 20 km surveys over hazardous terrain, before entering a safe zone where its batteries can be swapped or recharged. Both these robots prove the value and feasibility of autonomous ground-based data collection across ice sheets.

## 1.2 Scope of Work

This work is focused on two aspects of autonomous rover data collection in the Arctic and Antarctica to progress beyond a mere proof of concept and toward implementing robotic surveys on a scale comparable to remote sensing in these regions. The GPR data collected on long, overland traverses quickly becomes an overwhelming data set due to the very high spatial resolution this ground-based measurement provides. For the over 4000 km of GPR data collected on GreenTrACS, the layers in the data were traced manually using a spline smoothing function to interpolate the layers between human picked points along the transect [14]. Manual picking also reduces the number of distinct layers traced in the radargram, since only the layers most obvious to the human eye are picked, further reducing the value of such a detailed ground survey. Therefore, a hybrid GPR layer picking method

was developed to extract more detailed layer information from ground-based GPR records, using the average square difference function to trace layers over thousands of kilometers with manual modification for areas of high noise.

Another issue encountered with the Dartmouth robots, and one on which this thesis is focused, is their intermittent immobilization. Both robot bodies have been optimized for their specific tasking. The majority of engineering work on *Cool Robot* was focused on fabricating a lightweight body and selecting the lightest components to reduce surface pressure and the total sinkage in even the lowest density snow. Therefore, *Cool Robot*'s chassis is constructed from honeycomb composite panels, primarily used in the aircraft industry, with thin hollow aluminum shafts used to transmit torque from the motors to the custom lightweight aluminum wheel hubs [18]. *Yeti*'s chassis was designed to handle the undulating terrain of Antarctica and needed greater drawbar pull. Therefore, the body of *Yeti* was designed with a heavier, welded aluminum frame with the central articulation described above [17]. However, there was no engineering design of the tractive elements interacting with the snow surface. Both robots use off-the-shelf ATV tires that are designed and manufactured primarily for off-road use on soil. While these tires function reasonably well on most snowy terrain encountered in Greenland and Antarctica, the robots irregularly become immobilized depending on snow conditions. In the 2013 season in Greenland, *Cool Robot* became stuck roughly once every 50 km [15]; in the 2017 season in Greenland, *Cool Robot* became immobilized about once every kilometer. In Antarctica, *Yeti* has been rendered immobile only four times in its 2000 km of towing the GPR sled over the course of multiple years. While this is satisfactory for proof-of-concept prototypes, this is unacceptable for rovers designed to replace manned traverses of the ice sheets over long time periods (days to weeks). In the least consequential of cases, immobilization can be solved by simply snowmobiling out to the site and manually pushing the robot out of soft snow. However, if this loss of traction would occur in a crevasse field, the recovery effort is dangerous and resource intensive, with the need for helicopters and safety personnel to

retrieve it. Therefore, the second section of this thesis is devoted to two methods to reduce the likelihood of the rover becoming immobilized. The first method is the redesign of the rover’s tractive elements by using terramechanics theory to improve their trafficability over the full range of snow’s terrain properties while also evaluating the impact of design changes to the whole rover system. To test this theory, a new rover is built with the redesigned wheels and tested on unmodified terrain. The second approach to minimize the risk of immobilization is to instrument the robot and develop a method by which a future loss of mobility can be detected in real time using proprioceptive sensor data before the rover is completely immobilized. Enough warning time would potentially allow for evasive maneuvers to be performed to avoid the hazardous terrain or allow the rover to enter a traction control sequence to maintain mobility. This work uses the collected data to investigate how the dynamics of the vehicle are altered by interactions with variable terrain. From these models, algorithms that detect incipient immobilization are developed and then tested on collected data as well as on simulations of scenarios not measured in the field.

### 1.3 Contributions

While the contributions from this work extend across various fields of research, including glaciology, terramechanics, and robotics, they are all made in an effort to improve autonomous data collection capabilities in the Earth’s polar regions. Therefore, this thesis is not only meant to discuss the modeling done in these areas, but also make clear the practical applications of this research and make accessible the tools and algorithms developed.

To improve layer picking efficiency and accuracy, Ch. 2 outlines an effective sequence of processing steps that can be widely used for filtering GPR data of snow and ice. It also describes an interactive desktop application developed for tracing multiple layers within the GPR data over long distances. The code for this MATLAB application can be found in the GitHub repository for this project [19], described in Appendix B. Also included in the

repository are example GPR records of unprocessed and processed files, as well as traced layer metadata corresponding to these files. This application can be immediately employed to track layers on other GPR files, and the source code is provided to allow for adaptation to meet other researcher's needs.

Chapter 3 outlines a new method of evaluating wheel design and provides a framework for assessing the impact of changing wheel dimensions on a rover's mobility. This sensitivity study can be used by researchers in the design phase of a rover to approximate the performance of the tractive elements and appropriately size motors given the geometry of the wheels and the range of terrains expected. The code for generating these data, and for the underlying terramechanics models, is also located in the GitHub repository [19] described in Appendix B.

Chapters 6 and 7 describe a terramechanics model of wheel-terrain interaction combined with a rigid-body dynamics model of the rover that leads to a method for real-time incipient immobilization detection. Similar to the wheel sensitivity study, the simulation of various robot configurations operating in deformable terrain can be used to help engineers make informed design decisions. In addition, the code for detecting an imminent loss of traction can be easily adapted for real-time implementation on mobile rovers. This has the potential to enhance mobility of a robot through control rather than necessitating a significant change in its scale, mass, or energy budget. Both the model and the detection algorithm are made available on GitHub [19] (see Appendix B).

The final contribution is the prototype rover *FrostyBoy* itself. While developed to test the theories in this dissertation, it is also a tool available to researchers for autonomous data collection on snowy terrain. With the ability to tow a sled, the rover is highly modular in what sensors it can move around the ice sheet. Also, due to the systematic improvements in its mobility, *FrostyBoy* can maintain traction on a much wider range of terrains than previous snow rovers, making it a viable alternative to human data collection activities in these regions.

# **Chapter 2**

## **Ground Penetrating Radar**

### **2.1 Introduction**

The ability to understand the history of the Greenland and Antarctic ice sheets allows for more accurate glacial models and predictions of the future climate. Ground penetrating radar (GPR) is a common technique for accessing this preserved climate record and for observing how climate and environmental factors have shaped the underlying firn and ice stratigraphy. Most of the information gleaned from these data relies on the fact that layers in the ice are typically isochronous [20]. Therefore, evidence of past climate can be extracted through accurate picking of ice or firn layers. This technique has been used to study accumulation history by linking ice core measurements at various depths from one location to ice cores drilled at locations hundreds, if not thousands of kilometers away [13] [21] [22]. This allows for age, depth, and layer thickness relationships from the ice core data to be extrapolated over large areas. Compaction rates of firn, an important variable in estimating water equivalent held in the ice sheet and for translating surface elevation measurements to surface mass balance, can also be obtained by tracing isochronous layers. Compaction rates can be mapped to entire regions by taking limited numbers of single point depth-density profiles from year to year and tracing layers in a gridded GPR survey

around these points [23]. Tracking folding and undulations in GPR layers also gives insight into glacial dynamics and historical forcings [11] [24].

A large quantity of GPR data has already been collected to various depths over vast areas of the Greenland and Antarctic ice sheets in airborne, snowmobile, and most recently robotic campaigns [13] [15] [21] [22]. However, the methods by which informative, isochronal layers are traced in this large data set vary greatly. One common approach is manually tracing layers, which is tedious and time-consuming, but allows for easy resolution of discontinuities in the traced layer or interpolation through noisy sections. Due to the amount of effort and hours required in manual picking, some automated and semi-automated methods of picking have been developed. Some of these methods only work for obvious layers with minimal noise in deep GPR records that penetrate hundreds of meters into the ice. In these cases, a threshold can be applied to convert a radargram image to a binary data set [25] or simple peak-following, commonly available in commercial GPR analysis packages, can be used to trace the layers [23]. Other, more complex algorithms, like Fahnestock's use of cross-correlation to track a layer's signature from airborne measurements over Greenland [26] were considered to be too computationally slow for implementation for the high, along-track resolution of ground-based measurements. Also, most of these methods that rely on full automation are unable to follow the isochrone through areas of high noise or where there are interfering diffractions [27] [28]. Therefore, a hybrid approach can be highly effective, combining the efficiency of auto tracing algorithms with the ability for the user to manually correct sections where it fails to follow the layer. The system presented in this thesis is intended to leverage this user interaction and combine it with a more accurate and faster layer picking algorithm than previously developed. The software is also packaged in a user friendly and publicly available application to allow for easy isochrone picking in GPR records collected in a range of frequencies.

## **2.2 Background**

Ground penetrating radar records, known as echograms or radargrams, are collected by transmitting radar pulses into the ground and recording the strength and travel time of the reflected pulse. The pulse is reflected where it transitions through layers with different permittivities, with the greater the difference in dielectric properties, the stronger the return. In ice and firn, these differences in dielectric properties result from different density layers, which occur naturally on an annual, seasonal cycle due to formation of hoar frost and ice crusts [20]. Depth of these internal reflection horizons (IRH) can be calculated by knowing the two-way travel time of the pulse and the speed at which electromagnetic radiation travels through the ground material. It is the extraction of these data, IRHs vs. travel time, that can be expedited and enhanced with the Average square difference function Layer Picking System (ALPS).

## **2.3 Methods**

### **2.3.1 Data**

The system was tested with data collected in the 2017 Greenland Traverse for Accumulation and Climate Studies (GreenTrACS). This team towed both 900 MHz and 400 MHz GPR antennas behind their snowmobiles traveling at approximately 4.6 m/s. The GPR data were collected with a GSSI SIR-30E system, at 4096 samples per trace and a listening window of 200 and 800 ns respectively for the two different frequencies, corresponding to a penetration depth of approximately 21 and 85 meters (assuming a dielectric constant of 2.0). The files were geolocated using a Garmin 19x GPS receiver. The GreenTrACS project collected over 2400 km of data in 2017; however, only a small subset of approximately 175 km was processed and analyzed to test the auto tracing algorithm and user interface. The section analyzed lies between the sites of Cores 13 and 14, which can be seen in Fig. 2.1.

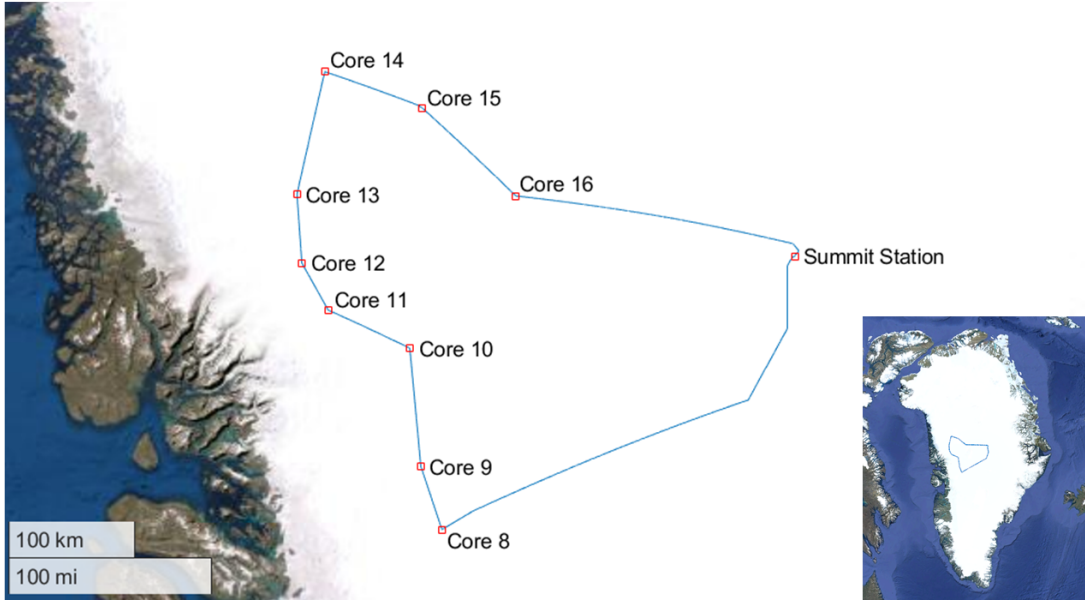


Figure 2.1: Map of the GreenTrACS 2017 route. The section analyzed with ALPS lies between the sites of Cores 13 and 14.

### 2.3.2 Data Processing

Due to the variable speed of data collected via a snowmobile traverse, the first step in processing the 400 and 900 MHz data is distance normalization. For the 175 km analyzed, the GPS record and the haversine formula were used to average/stack all traces within +/- 2.5 meters of one another into a single trace of 4096 samples, resulting in an echogram with one trace every 5 meters. Typical GPR processing techniques were applied after distance normalization using GSSI's RADAN 7 software. This included a time zero offset to determine what sample number corresponds to the snow surface, which was chosen to be 0.53 ns earlier than the rise of the direct coupling wave due to the 16 cm separation of the transmitter and receiver antennas. An IIR bandpass filter with a high pass set to 250 MHz and a low pass set to 550 MHz was applied to remove noise, and a horizontal FIR boxcar filter with a length of 501 scans was employed to eliminate artifacts throughout the radargram. RADAN's eight point auto-gain function was used to compensate for the attenuation of the signal as it penetrates deeper into the firn. Finally, the profile was Hilbert transformed to convert wavelets into overall envelope amplitudes and stacked by a factor of seven to in-

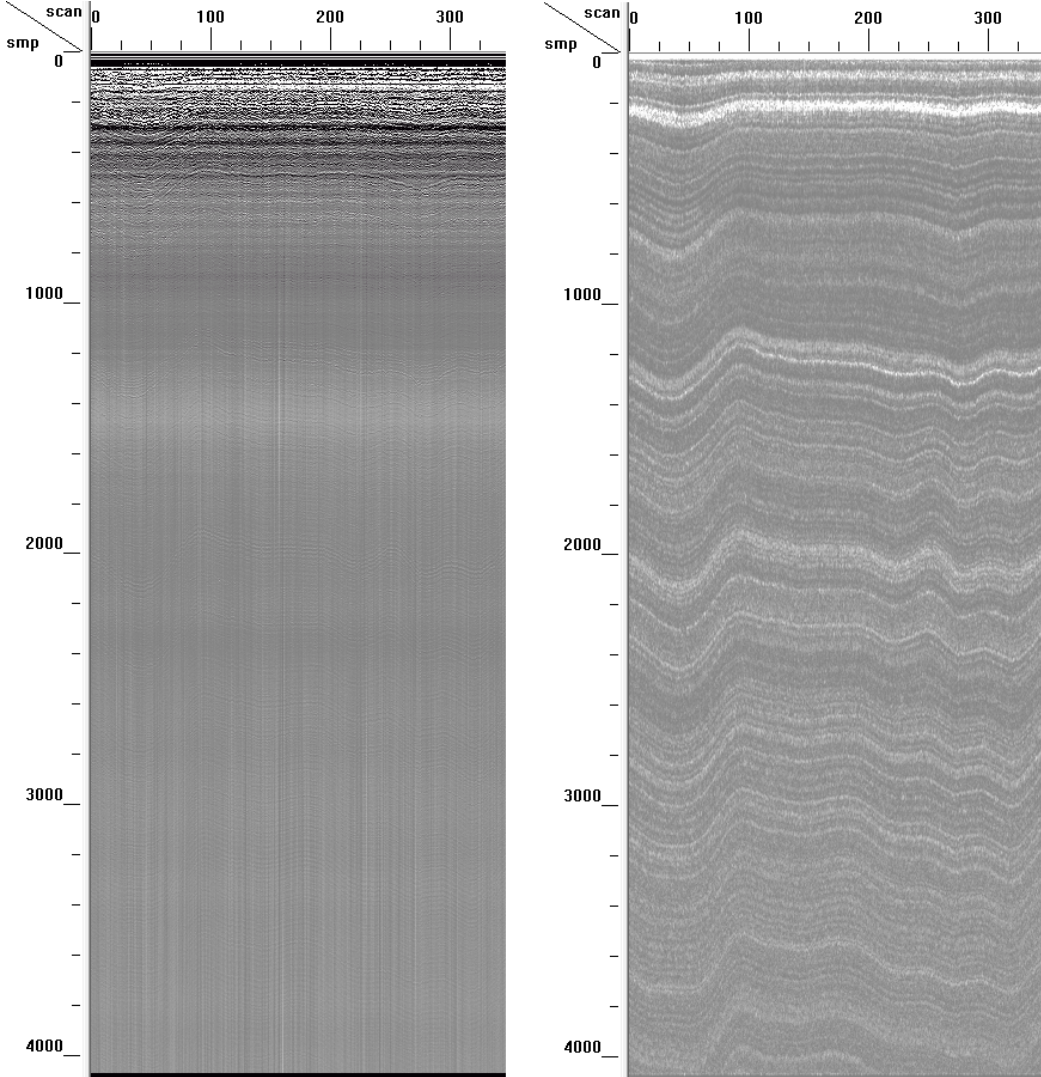


Figure 2.2: 10 km segment of a radargram acquired from 400 MHz antenna before filtering (left) and after filtering (right).

crease the signal-to-noise ratio, resulting in one trace every  $\sim$ 35 meters. Figure 2.2 shows an example radargram before and after the filtering, automatic gain, and Hilbert transform steps are applied.

### 2.3.3 Layer Picking System

The ALPS interface allows users to automatically trace IRHs across a radargram, and displays the results so the user can modify any departures from the intended layer. The

user begins the layer tracing process by first loading a GPR file that can be as basic as a MATLAB matrix or as detailed as a geolocated GSSI file. Once properly displayed as a grayscale image of trace number/distance vs. sample number/depth, the user can add layers by clicking on, or nearby, a seemingly continuous layer. In the case of the GreenTrACS data, these layers can be initialized by knowing the depth of a noteworthy segment of an ice core and clicking near this depth at the right location in the image. The software then searches within the trace selected for the maximum return in a user settable range, known as the *peak window*,  $P$ , around the selected location. A cost function

$$R_{ASDF}(h) = \frac{1}{N+1} \sum_{n=i-\frac{N}{2}}^{i+\frac{N}{2}} [x(n) - s(n+h)]^2 \quad (2.1)$$

is then evaluated with this max value's sample number,  $i$ , set to the center of the user settable *search window*,  $N$ . The average of the square of the differences between the trace initially selected,  $x$ , and the adjacent trace,  $s$ , is calculated over this range. This average value,  $R$ , is then calculated for each value of  $h$ . The range of  $h$  is determined by a user settable *shift window* parameter,  $H$ , with  $h$  taking on all integer values from  $-H/2$  to  $H/2$ . The  $h$  corresponding to the minimum  $R_{ASDF}$  value describes the number of samples the IRH shifts up or down relative to the original pick of the previous trace. The maximum return within the peak window of this new sample number becomes the new  $i$  and the process is repeated for each subsequent trace without human intervention.

All three user settable parameters can be modified for each layer being tracked. Finding

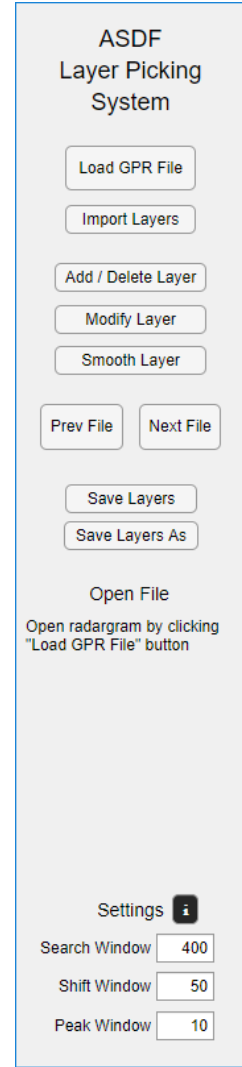


Figure 2.3: Control panel of ALPS

the right values for  $N$ ,  $H$ , and  $P$  is somewhat iterative and depends on how the slope of the layers and the spacing between layers vary with depth and distance. A radar record where layers vary significantly with increasing depth would require a smaller search window,  $N$ , than a record with more consistent slope variation with depth. Similarly, an IRH that is relatively flat would need a smaller shift window,  $H$ , than one that undulates drastically over short distances. The peak window,  $P$ , is set to a smaller value when layers are close together to minimize the possibility of jumping to a nearby layer with a higher return than the layer of interest. Once a layer has been traced across an entire echogram, the user has the option to delete the layer, in order to try again with different parameters, or modify the layer locally, to fix areas of inaccurate tracing. In order to modify a layer, the user simply selects the region to be recalculated and a point within this section that corresponds to the layer of interest. ALPS then automatically traces this subsection using the same method described above. If necessary, the user can manually modify the location of individual points of a traced layer in areas of high noise.

Once all layers of interest for the first file are adequately picked, the user can save the geolocated layers and then open the next file in the GPR transect, which will display adjacent to the open radargram. The layers from the first file are automatically propagated across the next file using their respective settings. The user is then able to modify these propagated layers before moving on to the next file. All subsequent files are treated in this manner, allowing the user to monitor each step of the layer picking process and ensure accuracy while saving time. Fig. 2.3 shows the graphical user interface for the processes described above.

## 2.4 Results

ALPS is evaluated for ease of use, accuracy, and speed by comparing it to the manual layer picking on the GreenTrACS data. Lewis [13] manually traced nine layers in the top 1500

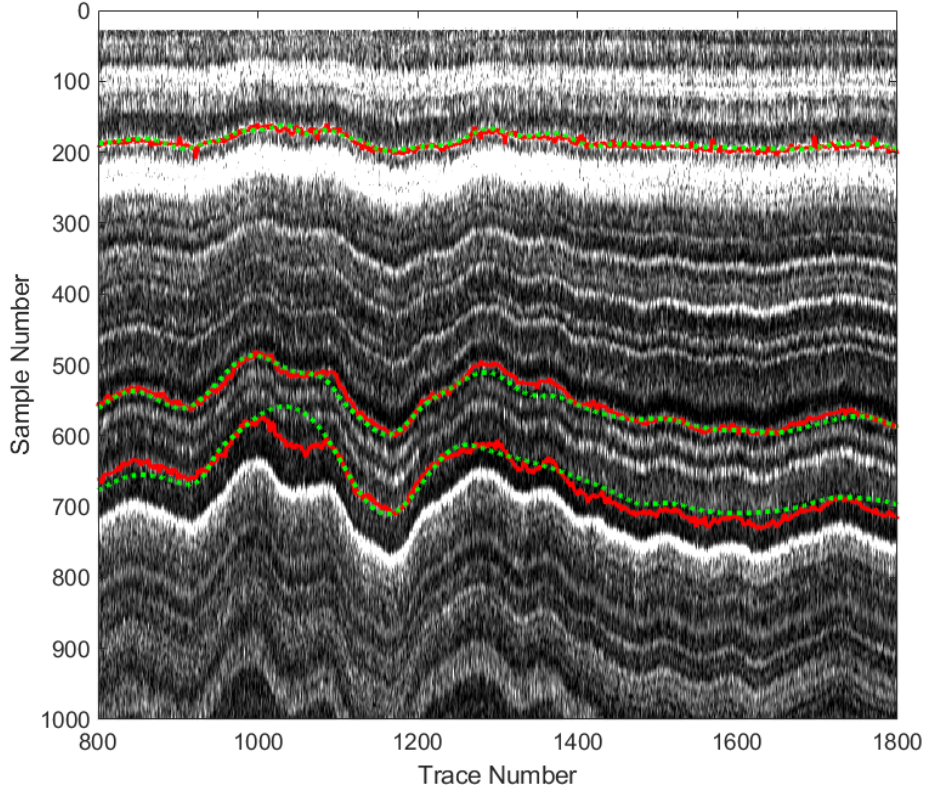


Figure 2.4: Approximately 35 km of 400 MHz data with manual (dotted green) and ALPS (solid red) traces of IRHs.

samples (depth of approximately 40 meters) of the 400 MHz GPR data in order to track isochrones between ice core samples for accumulation measurements. This layer picking for accumulation measurements was performed over distances on the order of thousands of kilometers, without distance normalization, and with different processing steps. Therefore, these picks could not be examined in the relevant file sizes for ALPS of approximately 15km. Lewis then manually retraced three layers in a 175 km subsection of the 400 MHz data, processed as described above, using his previous, manual layer picking method for the purpose of comparing it to ALPS. The results from this comparison can be seen in Fig. 2.4 showing a random selection of approximately 35 km of the 175 km processed. The manually picked layers are in green and the ALPS layers are in red.

Without ground truth, only the relative differences can be calculated and the accuracy of the picking is verified by visual inspection. This inspection shows that the ALPS layers

track the peaks of the IRH's very accurately, while the manually picked smoothed splines do not accurately capture the undulations on the scale of 2 to 4 km ( $\sim$ 60 to 120 traces), especially when looking at layers deeper in the snowpack and further from the flat surface. This is evident in the standard deviations of the manually picked layers relative to the ALPS layers increasing with depth; the standard deviations of the first three layers picked are 4.6 samples, 7.8 samples, and 16.3 samples, respectively. Using an average dielectric permittivity value of 2.0 for the relevant top 20 meters of firn, these standard deviations in samples correspond to standard deviations in depth of 0.10 m, 0.16 m, and 0.33 m, respectively. The amount of time taken to pick these layers is also improved, with Lewis spending approximately 30 minutes and the ALPS system requiring only 15 minutes total, even with recalculating sections. In addition, the time required to track additional layers increases linearly with manual picking but requires only slightly more time using ALPS in the initial pick and any section modification that is required in subsequent files.

## 2.5 Conclusion

The goal of ALPS is to create a more effective means of tracking IRHs in GPR records by combining an automatic tracing algorithm with an easy-to-use interface for modification in areas of low signal-to-noise ratio. It has been shown to dramatically decrease the time required to pick many layers over hundreds of kilometers with increased resolution over traditional manual layer picking methods. It is therefore ideally suited for long distance, continuous isochrones, as can be found in the GreenTrACS data traversing the non-coastal Greenland ice sheet. A limitation of the software is that it would not be able to accurately track layers through the discontinuities inherent in data collected closer to the ice margin or in heavily crevassed terrain. Also, even though it is a primarily automated tracing system, it does not eliminate the subjectivity of a user picking layers. In fact, ALPS relies on the user to distinguish what constitutes a continuous layer and approve of all automatically

traced sections. ALPS is also not meant to be a full suite of tools with which to process and analyze GPR data. Instead, it is a robust, effective, and easy-to-use method of tracing isochrones over long distances with high accuracy. The ALPS application can be found in the GitHub repository for this project [19], described in Appendix B.

# Chapter 3

## Tractive Element Design

### 3.1 Introduction

To design tractive elements for a snow rover, the basics of mobility and terramechanics must be understood. A rover's mobility on flat, deformable terrain is defined as generating enough forward thrust at the interface between the wheels and snow surface to overcome all resistance forces. These resistance forces include wind resistance, internal friction losses, and gravity forces on a slope, but this study focuses primarily on compaction and bulldozing resistances that result when the rover sinks into and compresses the terrain. The difference between tractive forces and resistance forces is termed drawbar pull and it serves as the quantitative indicator of a vehicle's ability to traverse a given terrain. While it may seem like drawbar pull should therefore be maximized in order to increase the load that can be towed, the slope that can be climbed, and obstacles that can be overcome, drawbar pull needs to be optimized for the use case of the rover in order to minimize power consumption. This is especially important when the robot is to be solar powered.

This discussion of terramechanics models focuses on rigid wheels, rather than tracks or pneumatic tires, and their interaction with deformable terrain. Track systems result in much greater frictional energy losses in the drive train compared to wheels and add significant

weight and complexity to an otherwise basic and simple robot. Also, from tire studies on deformable terrain [29] and observations of pneumatic tires on snow, there is no significant deformation of the ATV tires used on *Cool Robot* and *Yeti* that would lead to a patch of constant pressure. Therefore, all models presented in this section are for a rigid-wheeled vehicle.

The goal of understanding the underlying terramechanics theory is to develop a framework for designing wheels customized for the terrain they are expected to encounter. This design framework must show how modifications to the wheel width and diameter will not only impact torque and drawbar pull, but also the rover as a system, with their effects on component sizing, rover weight, and energy use also being considered. Ultimately, the goal is to use these principles in designing and building new wheels for a prototype rover, making it less susceptible to immobilization on a wide range of snow types.

## 3.2 Background

The fundamental concepts that serve as the foundation for a rigid wheel interacting with a deformable terrain were introduced by Bekker in the 1950's [30] and were expanded upon by Wong and Reece in the late 1960's [31] [32]. The semi-empirical equations, in what's known as the Bekker-Wong model, defined the basics of how a wheel sinks into the terrain, how this sinkage resists forward motion, and how the pressure distribution below the wheel impacts its ability to gain traction and convert torque to forward velocity. However, this work focused on a larger class of off-road vehicles with Bekker himself specifically noting that these models would lose accuracy in predicting performance of lighter-weight vehicles with wheel diameters less than 50 cm [2]. Therefore, modifications to these equations have been proposed to better predict the mobility of a lighter-weight, smaller-wheeled vehicle.

As interest in sending wheeled mobile robots (WMRs) to explore other planets increased, researchers focused on single-wheel experiments to better define the semi-empirical

equations and the associated terrain parameters defining a rigid wheel's interaction with deformable terrain. In these experiments, testbeds are filled with a homogeneous terrain type, typically sand or a Mars or Lunar simulant, and an instrumented single-wheel traversed the testbed, with the wheel speed, its longitudinal velocity, applied torque, and normal load being controlled and/or measured. In some studies, pressure sensors mounted within the rim of the wheel allowed for direct measurement of the shear and normal stress profiles developed under a rigid wheel [33] [34] [35]. Other studies employed transparent testbed walls and high-speed cameras to track soil particle movement beneath the wheels [33] [36] [37]. With this controlled test environment, researchers began recommending modifications to the Bekker-Wong model equations by introducing additional parameters. Meirion-Griffith and Spenko looked at pressure-sinkage curves in a single-wheel testbed for small diameter wheels and proposed a new model that took wheel diameter into account, finding a strong dependence on wheel curvature [38]. Similarly, Ding studied the pressure-sinkage relationship for lightweight vehicles and proposed an empirically determined, dynamic modification of the sinkage exponent parameter rather than having this be a static descriptor of a terrain type [39]. In addition, Jayakumar suggested making modifications to the pressure-sinkage curves and the shear equations to account for nonlinear effects seen with lighter vehicles [34]. While these updated models have been shown to have a good fit with the single-wheel experimental data from which they were derived, there has been no universal adoption of these new models by terramechanics researchers. Values for the additional terrain parameters are highly specific and tuned to the terrain being used in the single-wheel testbed, and yet none of these studies have been performed with snow. Only the common Bekker-Wong parameters can be found in the literature for snow. For this reason, the original equations and parameter set of the Bekker-Wong model serve as the principal method by which the performance of a lightweight, small-wheel-diameter rover in snow is evaluated in this thesis. This is justified as a reasonable approach seeing as Senatore found that predictions of torque, drawbar pull, and sinkage for lightweight vehicles

(defined as having an average surface pressure below 20 kPa) using only the Bekker-Wong model were reliably within 11% of experimental data collected in a testbed of Mojave Martian Simulant [33]. Ishigami could also replicate four-wheel testbed studies in loose soil by using these equations in a multi-body model to simulate a 35 kg rover's behavior, with four 0.18 m diameter and 0.11 m width wheels [40]. This approximation is bound to be less accurate for snow, as different snow surfaces can have drastically different characteristics. As a result, the design of the tractive elements cannot be precisely optimized, but rather performance improvements can be evaluated and estimated by using the range of terrain parameters found in the literature and the most widely accepted terramechanics equations to constrain the design problem.

### 3.3 Sinkage

The interaction of rigid wheels and deformable terrain is largely based on the compression of the soil and the resultant sinkage. The amount of sinkage and the pressure distribution under the wheel determine the forces resisting the robot's motion as well as the shear stress that can be applied to the terrain to propel the robot forward. Terramechanics models are often differentiated by their determination of contact pressure vs. wheel sinkage relationships. These semi-empirical equations are developed by performing plate indentation tests, in which different sized plates of known area are driven vertically down into the terrain while logging force and displacement, allowing for a curve of pressure vs. sinkage to be generated. Most models are based on the original Bernstein-Goriatchkin model [30]

$$p = kz^n \quad (3.1)$$

which shows that pressure,  $p$ , is a nonlinear function of sinkage,  $z$ , dependent on an exponent,  $n$ , and a sinkage modulus,  $k$ . Bekker then expanded on this equation, showing that

the pressure-sinkage curve varied depending on the plate size used in the indentation test

$$p = \left( \frac{k_c}{b} + k_\phi \right) z^n \quad (3.2)$$

where  $k_c$  is the cohesive modulus,  $k_\phi$  is the friction modulus, and  $b$  is the smaller dimension of the plate being used [30]. In rigid-wheel pressure-sinkage studies, the width of the wheel serves as the parameter  $b$ . This equation is widely accepted as a valid relationship for relating pressure and sinkage, therefore the cohesive and friction moduli as well as the exponent  $n$  have been empirically determined for a variety of terrains [2]. Although, this relationship has also been shown to be too simple. From Bekker's equation, it follows that

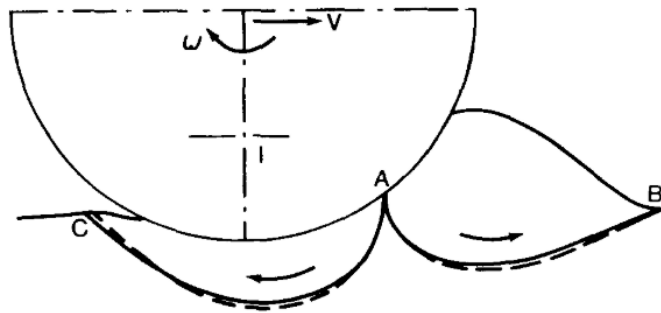


Figure 3.1: Forward and backward flow of soil beneath a driven wheel [2].

the pressure distribution under a rigid wheel would be highest at the lowest point, directly below the axle of the wheel, but Wong showed that this is not the case. In studying flow of soil underneath a driven wheel, he found that there are two regimes [2]. In the front region, ahead of a point, labeled A in Fig. 3.1, the soil actually flows forward in the direction of robot travel, and the soil beneath the rear region flows backward. Where the two failure zones meet is the location of the maximum normal pressure, which moves forward with increasing slip [31]. Denoting  $\theta_2$  as the angle from bottom-dead-center (BDC) at which the back end of the wheel exits the soil,  $\theta_m$  as the angle from BDC at which the pressure is maximum, and  $\theta_1$  as the angle from BDC to the surface of the terrain,  $\theta_m$  can be calculated

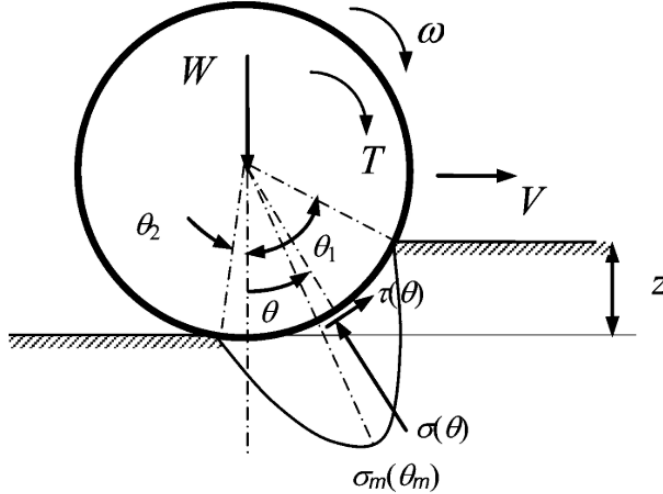


Figure 3.2: Stress distribution below a rigid wheel in deformable terrain [6].

from the equation

$$\theta_m = (c_1 + c_2 i) \theta_1 \quad (3.3)$$

where  $c_1$  and  $c_2$  are empirically determined coefficients and  $i$  is the slip ratio. Using this nomenclature, the pressure distribution from  $\theta_1$  to  $\theta_m$  is determined according to the Bekker pressure-sinkage model (3.2), rewritten below in terms of  $\theta$

$$\sigma(\theta) = \left( \frac{k_c}{b} + k_\phi \right) r_w^n (\cos \theta - \cos \theta_1)^n \quad (3.4)$$

From  $\theta_m$  to  $\theta_2$ , Reece found that the normal pressure around the rim of the wheel decreased to zero, with the stress at any position in the rear region matching the stress at the corresponding relative position in the front region [31]. The equation of the stress distribution below the rear region is thus

$$\sigma(\theta) = \left( \frac{k_c}{b} + k_\phi \right) r_w^n \left[ \cos \left( \theta_1 - \left( \frac{\theta - \theta_2}{\theta_m - \theta_2} \right) (\theta_1 - \theta_m) \right) - \cos \theta_1 \right]^n \quad (3.5)$$

A representation of this stress distribution can be seen in Fig. 3.2. Single-wheel studies with force transducers mounted on the rim of the wheel have confirmed that these equations

Pressure-Sinkage Parameters - Bekker Model			
Terrain Parameter	Bekker 1	Bekker 2	Bekker 3
$n$	1.6	1.6	1.44
$k_c$ [kN/m <sup>n+1</sup> ]	4.37	2.49	10.55
$k_\phi$ [kN/m <sup>n+2</sup> ]	196.72	245.90	66.08

Table 3.1: Pressure-sinkage terrain parameters for three different types of snow for the Bekker model. Parameters for Bekker 1 and 3 are from Wong [2] and those for Bekker 2 are from Harrison [3].

serve as an accurate predictor of the stress distribution below a wheel traveling at a steady-state forward velocity [31] and the assumption of a constant pressure profile across the width of the wheel is valid for slip ratios up to 70% [33]. This is also assuming that the values of  $c_1$  and  $c_2$  have been chosen appropriately. For this analysis,  $c_1$  and  $c_2$  will be fixed to be 0.18 and 0.32 respectively to represent low cohesion snow, since no single-wheel studies have been performed to determine these parameters for snow, and these are commonly used values from the literature for modeling rigid wheels in loose, low cohesion sand [31].

These equations describing pressure-sinkage curves have also been shown to fit well with homogeneous terrains, such as sand (both dry and wet), sandy loam, clays, and a homogeneous snowpack [2]. But since snow is such a variable substance, with slight changes in density, morphology, and temperature histories causing drastic changes in structure, there is no tightly controlled range of values for  $n$ ,  $k_c$ , and  $k_\phi$  in the literature. Wong references parameters that define pressure-sinkage from three studies performed in snow [2] [3]. The parameter values are shown in Table 3.1 and the resultant pressure-sinkage curve is graphically shown in Fig. 3.3.

While the Bekker model (3.2) has been shown to fit a wide range of terrains' pressure-sinkage curves through manipulating its three parameters, and while Table 3.1 quotes accepted values for these parameters in snow, it has been shown to inadequately fit the curve of most bevameter tests performed in snow [4] [5] [41]. Therefore, other pressure sinkage models have been proposed specifically for deep snow, which is seen to have a linear

Pressure-Sinkage Parameters – Preston-Thomas Model					
Terrain Parameter	Preston 1	Preston 2	Preston 3	Preston 4	Preston 5
$k$ [kPa/m]	59	65	56.4	27.3	19.2
$z_m$ [m]	0.06	0.29	0.35	0.50	0.54

Table 3.2: Pressure-sinkage terrain parameters for five different snows using the Preston-Thomas model [4]. Parameters for Preston 1 were measured near Summit Station, Greenland [5] and parameters for Preston 2 - 5 were measured in Lebel-sur-Quévillon, Québec, Canada (see Ch. 5).

regime for small sinkage and a sharp increase in pressure as the snow compacts against a much denser layer within the snowpack. This general paradigm makes sense when thinking about how a layer of snow, exposed to an extended period of sunlight and wind, could form a sintered, dense crust over which a series of precipitation events deposit fresh, unconsolidated snow.

Wong and Preston-Thomas described this relationship to be

$$p(z) = k \left[ -\ln \left( 1 - \frac{z}{z_m} \right) \right] \quad (3.6)$$

where the terrain stiffness parameter,  $k$ , defines the linear portion where pressure is proportional to sinkage, and  $z_m$  is the depth of the denser layer [4]. This equation can be substituted for the Bekker model in Reece's equations above, to get an equation for  $\sigma$  in terms of  $\theta$ . Similar to the parameters in the Bekker model, the two parameters in the Preston-Thomas equation also vary widely for snow, shown in Table 3.2, with the parameters determined in what's labeled Preston 1 from measurements near Summit Station, Greenland [5], and those determined in Preston 2 through 5 measured in Québec, Canada and described in detail in Ch. 5.

One can begin to understand the difficulty in encapsulating the problem of designing tractive elements for snow by looking at the splay of pressure-sinkage curves in Fig. 3.3 and recognizing that this only describes the results from a limited set of experiments in just one subset of terramechanics theory. While this impedes attempts to converge on an

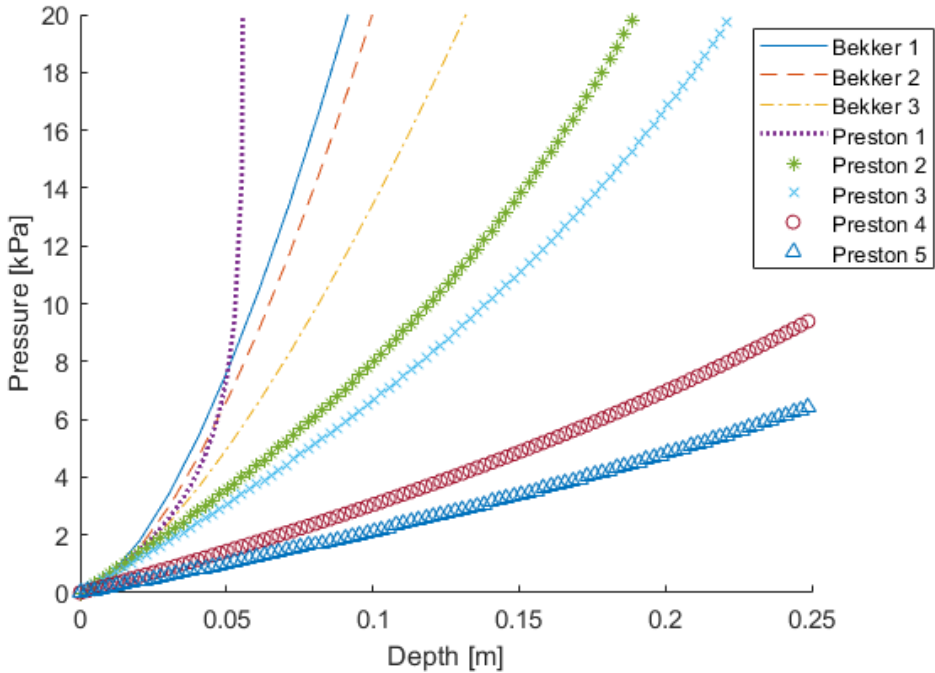


Figure 3.3: Range of pressure vs. sinkage profiles obtained in snow.

optimized wheel design, it does allow for the beginnings of defining and bounding the design challenge.

### 3.4 Traction

While the Bekker model describes how the terrain will deform under the weight of the robot, the shear failure of the terrain must be understood in order to calculate the robot's motive forces. The thrust produced by the robot wheel is limited by the properties of the terrain. At this interface, the loading conditions given by the weight and torque applied by the robot and the mechanical properties of the soil define a point at which the soil will fail. This failure is characterized by the transition from a state of plastic equilibrium to plastic flow. The Mohr-Coulomb failure criterion is simple and commonly used to define the shear stress,  $\tau$ , at which a soil will fail

$$\tau = c + \sigma \tan \phi \quad (3.7)$$

where  $c$  is the cohesion of the soil,  $\sigma$  is the normal stress (defined by the pressure-sinkage curves above), and  $\phi$  is the angle of internal friction. The values for cohesion and internal shearing angle of a given terrain are determined by using a shear plate or shear ring to find a relationship between shear stress and shear displacement (similar to the plate tests to determine pressure-sinkage relationships, described in the previous section) [2]. This relationship exhibits different characteristics depending on the terrain type. For example, sand, loam, and what's termed 'firm snow' [2] show a rapid increase in shear stress with shear displacement and after quickly reaching a maximum, the shear stress drops and reaches a steady-state value below its peak. This behavior can be characterized by

$$\tau = (c + \sigma \tan \phi) K_r \left\{ 1 + \left[ \frac{1}{K_r (1 - \frac{1}{e})} - 1 \right] e^{(1 - \frac{j}{K_w})} \right\} \left( 1 - e^{\frac{-j}{K_w}} \right) \quad (3.8)$$

where  $j$  is the shear displacement,  $K_r$  is the ratio of the residual shear stress to the maximum shear stress, and  $K_w$  is the amount of shear displacement that results in the maximum shear stress [2]. While the term 'firm snow' is used in the terramechanics literature, a better descriptor of this type of snow, to be compatible with definitions in glaciology and snow science, is *well bonded*. This means that the snow crystals have undergone some form of metamorphism that has resulted in the grains becoming connected at their boundaries, forming a three-dimensional network [42] and can be associated with high cohesion snow. This is contrasted with what is termed 'fresh snow' [2] in terramechanics literature, which describes newly deposited snow that is typically unmetamorphosed with no sintering between snow crystals. However, this property is not unique to new snow, as some forms of snow metamorphosis also result in loose, disconnected snow grains [42]. Therefore, the term *poorly bonded* will be used instead of 'fresh' to describe this type of low cohesion snow. For poorly bonded snow, the shear stress vs. shear displacement relationship has a different shape than that for well bonded snow. In this type of terrain, there is a similarly sharp increase in shear stress with displacement, with further shear displacement causing

the shear stress to rise and approach a steady-state, maximum value (also shown in Fig. 3.4, presented below). This behavior can be described by the following function

$$\tau = (c + \sigma \tan \phi) (1 - e^{-j/K_s}) \quad (3.9)$$

where  $j$  is the shear displacement, and  $K_s$  is the shear deformation modulus [2]. Shear displacement,  $j$ , along the contact patch of a rigid wheel can be calculated for both Eq. (3.8) and (3.9) for a given slip ratio,  $i$ , according to [2]

$$j(\theta) = r_w[\theta_1 - \theta - (1 - i)(\sin \theta_1 - \sin \theta)] \quad (3.10)$$

From these equations and the sinkage equations from section 3.3, the shear stress acting on the contact patch of the wheel can be calculated to give a tractive force. Therefore, the shear stress-shear displacement relationships are translated to tractive force vs. slip ratio plots for rigid wheels, as shown in Fig. 3.4. In this plot, the weight and wheel dimensions of *Cool Robot* are used in all calculations to allow for direct comparison of the two models. Both the well bonded and the poorly bonded shear stress-shear displacement relationships are used to evaluate wheel performance of the rover since it can be expected to encounter every type of snow possible. For the well bonded condition (3.8), the values of  $K_\omega$  and  $K_r$  have been found to be approximately 2.2 cm and 0.66 respectively [2]. For the poorly bonded condition (3.9), the value of the shear displacement modulus,  $K_s$ , has been found to be anywhere from 2.5 cm to 5 cm [2]. As for the values of  $c$  and  $\phi$  in the Mohr-Coulomb failure criterion (3.7), there is significant variation from experiment to experiment, most likely due to the variability of snow as a material. In addition, there is the issue of non-uniqueness, meaning that different combinations of values for the cohesion and angle of internal friction parameters can yield the same curves (discussed further in Ch. 4). From the three studies referenced by Wong, the range of cohesion,  $c$ , spans from approximately 0.6 kPa to 6 kPa [2]. Measurements for the angle of internal friction of snow also vary in

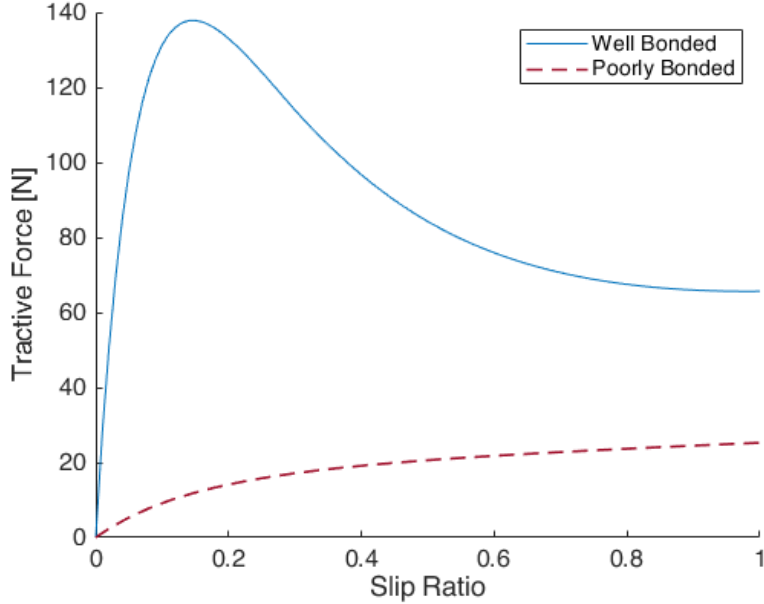


Figure 3.4: Comparison of *well bonded* (3.8) and *poorly bonded* (3.9) snow traction models for the two types of snow defined by the parameters in Table 3.3.

the literature, ranging from  $9^\circ$  [41] to  $23^\circ$  [2]. Since shear stress is a function of normal stress (3.7), the choice of pressure vs. sinkage parameters (discussed in section 3.3) also impacts the shear stress-shear displacement curve.

Ultimately, all the terrain parameters are linked, and independently forcing individual parameters to the extremes of their measured ranges yields incongruous results. For example, a well bonded snow would not likely have a shallow pressure-sinkage curve. Similarly, a poorly bonded snow would not, by definition, have high cohesion or a steep angle of internal friction. Therefore, the poorly bonded shear model will only be applied to low cohesion and low stiffness snowpacks, and the well bonded model will only be applied to high cohesion and high stiffness snowpacks. The wide range of tractive forces that can be achieved by a wheel operating on these two, very different types of snow is illustrated in Fig. 3.4, with Table 3.3 showing the relevant parameters for each curve presented. This plot further demonstrates the complexity of evaluating new wheel designs and the difficulty in optimizing them to handle all possible snow variants.

Terrain parameters for two different types of snow										
Parameter [Units]	$k$ [ $\frac{\text{kPa}}{\text{m}}$ ]	$z_m$ [cm]	$k_c$ [ $\frac{\text{kN}}{\text{m}^{n+1}}$ ]	$k_\phi$ [ $\frac{\text{kN}}{\text{m}^{n+2}}$ ]	$n$ -	$c$ [kPa]	$\phi$ [°]	$K_s$ [cm]	$K_\omega$ [cm]	$K_r$ -
Well Bonded, High Stiffness	-	-	2.49	246	1.6	6.0	23	-	2.2	0.66
Poorly Bonded, Low Stiffness	19.2	54	-	-	-	0.6	9	5.0	-	-

Table 3.3: Parameters used to compare a low stiffness, poorly bonded snow to a high stiffness, well bonded snow. The well bonded, high stiffness snow uses the well bonded shear stress-shear displacement model (3.8) and the Bekker pressure-sinkage model (3.2). The poorly bonded, low stiffness snow uses the poorly bonded shear stress-shear displacement model (3.9) and the Preston-Thomas pressure-sinkage model (3.6). Cells with no number mean that the parameter is not used in the models that describe this type of snow.

### 3.5 Balance of Forces

These simplified models of pressure vs. sinkage and shear stress vs. shear displacement allow us to calculate drawbar pull and trafficability of the vehicle with certain assumptions. The first assumption is that the two-dimensional normal and shear stress distributions along the rim of the wheel are uniform across the width of the wheel. The second is that the robot is traveling at a constant velocity and static equilibrium conditions hold. The balance of forces can then be described by the following equations:

$$W = r_w b \left[ \int_{\theta_2}^{\theta_1} \sigma(\theta) \cos \theta d\theta + \int_{\theta_2}^{\theta_1} \tau(\theta) \sin \theta d\theta \right] \quad (3.11)$$

$$F_x = r_w b \left[ \int_{\theta_2}^{\theta_1} \tau(\theta) \cos \theta d\theta - \int_{\theta_2}^{\theta_1} \sigma(\theta) \sin \theta d\theta \right] \quad (3.12)$$

$$T_r = r_w^2 b \int_{\theta_2}^{\theta_1} \tau(\theta) d\theta \quad (3.13)$$

$W$  is the weight of the robot,  $F_x$  is the drawbar pull, and  $T_r$  is the resistive torque. The first equation (3.11) defines the amount of sinkage the robot wheels will experience by

balancing the force exerted on the wheels by the terrain with the normal force of the robot. With this sinkage known, the shear force that can be applied by the wheel to the terrain before failure can be calculated (first term of Eq. (3.12)). This force must be greater than the compaction resistance force in opposition to the robot's motion (second term of Eq. (3.12)), in order for drawbar pull to be positive and for the robot to successfully traverse the terrain. The resistive torque (3.13) is the minimum torque that must be transmitted to the wheels in order to overcome the terrain forces.

## 3.6 Other Factors

While these are the basic equations for predicting vehicle mobility, other factors need to be considered. Another force acting against the motion of the robot is known as bulldozing resistance. The portion of a driven wheel in the forward flow regime of the soil discovered by Wong and Reece can be approximated by a blade pushing against the soil [2]. The soil experiences local shear failure and exhibits a resistive force equal to

$$R_b = b (0.667 z_t c K_c + 0.5 z_t^2 \gamma K_\gamma) \quad (3.14)$$

where  $b$  is the wheel width,  $z_t$  is the distance in the z-axis from the terrain surface to the transition point of the two flow regimes,  $c$  is cohesion,  $\gamma$  is the soil specific weight (set to 1.96 kN/m<sup>3</sup>), and  $K_c$  and  $K_\gamma$  are soil bearing capacity factors, calculated from Terzaghi's factors  $N_c$  and  $N_\gamma$  [43] [44]. This added term of bulldozing resistance is marginal with small sinkages but becomes important in calculating drawbar pull with the potential of encountering low stiffness, highly compressible snow.

The dynamic effect of sinkage induced from wheel slip is also not captured in the equilibrium equations above. This phenomenon can be seen when the wheels start to excavate the terrain with increased slip, sinking further and thus increasing the compaction resis-

tance. One formula developed to describe this effect has been validated in sands and clays

$$z_{actual} = z_0 + iS z_0 \quad (3.15)$$

where  $i$  is the slip and  $z_0$  is the sinkage that would occur were there no excavation (calculated using Bekker's pressure-sinkage relationship (3.2)), and  $S$  is the slip-sinkage coefficient calculated to be approximately 60%/30% [45]. Lyasko showed this relationship to be accurate for wheel slips up to 33%, increasing sinkage an additional 60%, with prediction errors using this model to be less than 5%. This theory was developed through single-wheel studies in soil, specifically Lunar soil simulant, but the same general principles can be expected to occur in poorly bonded snow as well.

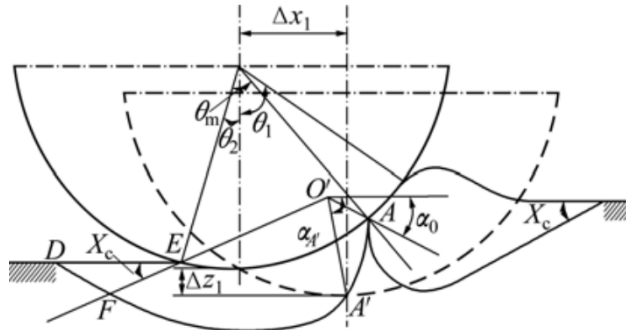


Figure 3.5: Logarithmic spiral curve that approximates additional sinkage due to slip [7].

Another theory of slip-sinkage is that presented by Ding, in which he calculates the envelope of soil that is flowing backwards relative to the longitudinal motion of the wheel in order to predict the resultant sinkage from this excavation. He describes the shear failure line beneath the wheel with a logarithmic spiral curve, shown in Fig. 3.5 as curve  $ADE$  [7]. As slip or as sinkage increases, the point of maximum normal stress,  $A$ , moves higher up the curve of the wheel and the shear flow failure envelope grows larger. As more soil is excavated from beneath the wheel, the added sinkage from slip,  $\Delta z_1$ , also increases. As with almost all these equations, this theory was developed through single-wheel studies in soil, specifically Lunar soil simulant, but the same general principles can be expected

to occur in dry snow as well. The larger issue with either Lyasko's or Ding's model for slip-sinkage is that they do not address how the added sinkage changes the pressure distribution below the wheel, meaning that the equilibrium equations above cannot be solved. Therefore, these equations will not be used directly in calculating improvements that can be made to the tractive elements of the snow rovers. However, limiting predicted sinkage should be a primary objective due to its direct impact on additional sinkage resulting from slip and the high potential for this slip-sinkage to immobilize the robot.

## 3.7 New Wheel Design

The main goal of modifying the wheel design of the robot is to increase drawbar pull to reduce the chances of immobilization when towing a load. Increasing drawbar pull is a combination of increasing the shear force applied to the terrain and decreasing the resistive forces of compaction resistance and bulldozing. To increase shear force, one can either increase the weight of the robot or increase the contact patch. Increasing the weight causes more sinkage and therefore higher compaction resistance, bulldozing, and slip-sinkage (3.15), so it should be minimized in whatever design changes are implemented. Increasing the contact patch by increasing the width or radius of the wheel is the clear choice, but understanding which parameter to vary and how it will affect compaction and bulldozing resistance is more complex.

To evaluate the effects of altering wheel dimensions on the rover's trafficability, the terramechanics equations outlined in the previous sections are used with the range of terrain parameters defined in section 3.3 and 3.4. Evaluating all combinations of the different models and parameter values found for snow with each combination of wheel width and radius would be an intractable problem and would only allow for optimization of the wheel dimensions for one type of snow. Therefore, only a worst and best case set of snow parameters, defined by their effect on the rover's mobility, will be used to understand the impact of

changing the wheel width and the wheel radius. The list of parameter definitions for these two types of snow was presented in Table 3.3, with the worst snow having low stiffness and therefore high sinkage for a given pressure, employing the poorly bonded model for shear stress-shear displacement, and using the lowest values in the measured range of cohesion and internal friction angle. In contrast, the best snow is that defined by high stiffness, low sinkage, the well bonded model, and the highest measured values for cohesion and internal friction angle. The values for  $c_1$ ,  $c_2$ ,  $\theta_2$ , slip ratio, and the inputs to the bulldozing equation (3.14) remain constant for both snow conditions.

The literature suggests that increasing the radius of the wheel reduces compaction resistance more effectively than increasing wheel width [2] [46]. Terrain resistance is calculated using Eq. (3.11), where the normal pressure distribution is defined by Eq. (3.4) and (3.5) and the shear stress is defined by Eq. (3.8), (3.9), and (3.10). These equations allow for sinkage to be determined for a four-wheeled, 60 kg robot in snow and for the resultant terrain resistance to forward motion for each wheel to be calculated. Starting from wheel dimensions that roughly correspond to those of the pneumatic tires on *Cool Robot* and *Yeti*, the terrain resistance is compared for an increase in width of 0.3 m to an increase in radius of 0.3 m, with the assumption of a constant mass. Figure 3.6 shows the relative decrease in the terrain resistance forces given these design changes for two cases, with Fig. 3.6a using the low stiffness, poorly bonded snow parameters and Fig. 3.6b using the high stiffness, well bonded snow parameters. Both graphs show the same trend predicted by Wong and Wallace, with an increase in a wheel's radius proving more effective in reducing terrain resistance than an increase in the wheel's width by the same dimension, given a constant load on the wheel.

This direct comparison of terrain resistance for one-to-one changes in radius and width is not particularly useful. These graphs capture no part of the predicted sinkage, which has been shown to have a large impact on slip-sinkage effects, no indicator of drawbar pull, which takes into account the increased shear force as well as both compaction resistance

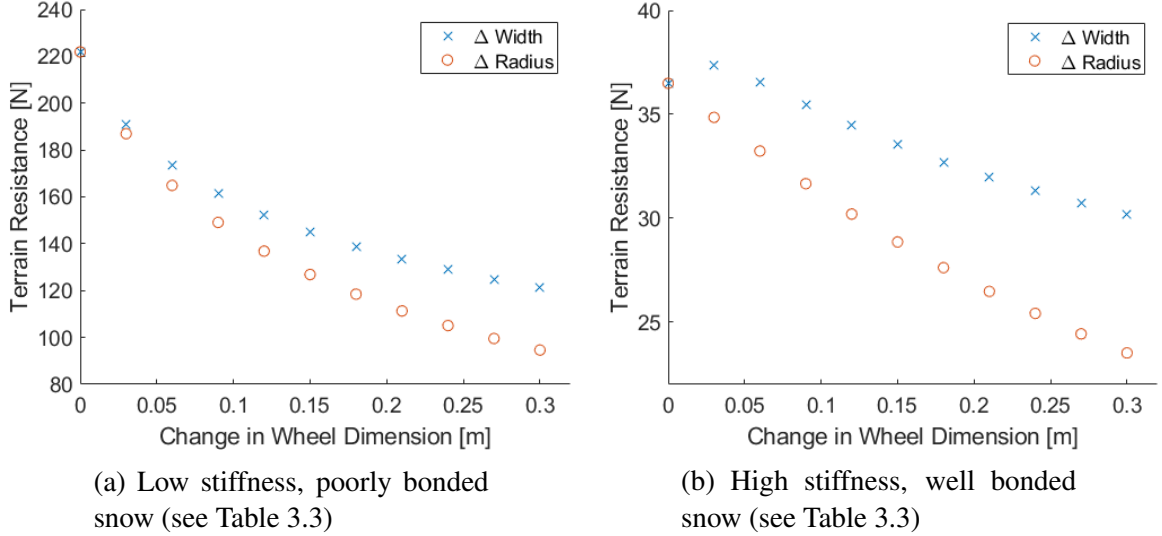
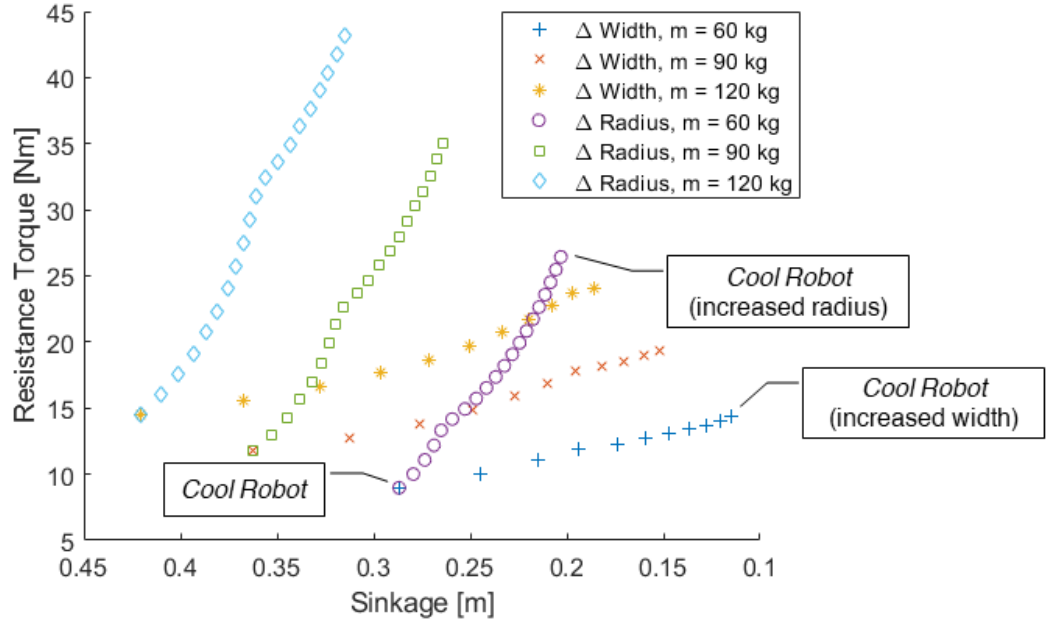
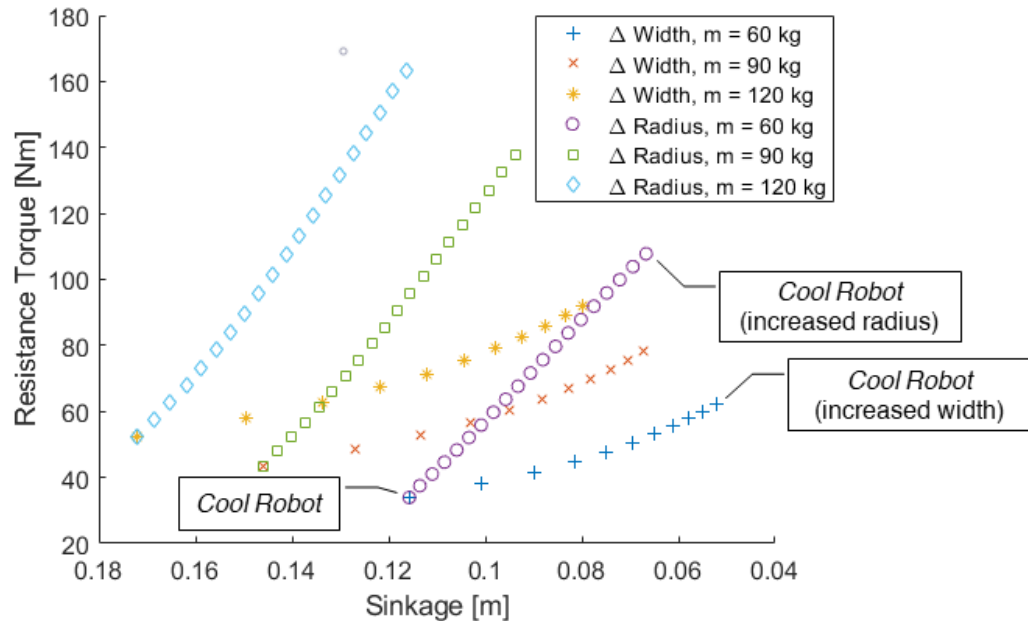


Figure 3.6: Modeled decrease in compaction resistance of a single wheel with changes in the wheel’s dimensions. Wheel width,  $b$ , increases from 0.1 m to 0.4 m. Radius,  $r_w$ , increases from 0.2 m to 0.5 m. All other variables, including the assumed 60 kg mass of the rover, are kept constant.

and bulldozing forces, and nothing of the torque required, which would define the motor sizing and energy usage. Therefore, more useful evaluations of changes to radius and width are presented in Fig. 3.8 for the two types of snow. Figures 3.7a and 3.7b show how changing the width of the wheel,  $b$ , decreases sinkage for a given increase in resistive torque far more effectively than increasing the radius of the wheel. This is important in sizing the motor and gearbox for the robot. Increasing the radius of the wheel would almost certainly require a larger motor to handle the higher torques and could potentially require a lengthening of the chassis, resulting in an increase in body weight as well as wheel weight, without a significant decrease in sinkage. On the other hand, increasing the width of the wheel (especially in low stiffness, poorly bonded snow), has a drastic impact on reducing sinkage and is less likely to necessitate up-sizing the motor. The only impact on weight would be the heavier wheels. The second set of graphs (Fig. 3.8a and 3.8b) shows how much the increase in torque, given a change in wheel dimensions, translates to a change in drawbar pull by introducing a new variable called the *mobility efficiency* factor. Instead of normalizing drawbar pull by vehicle weight, as is done with the traction

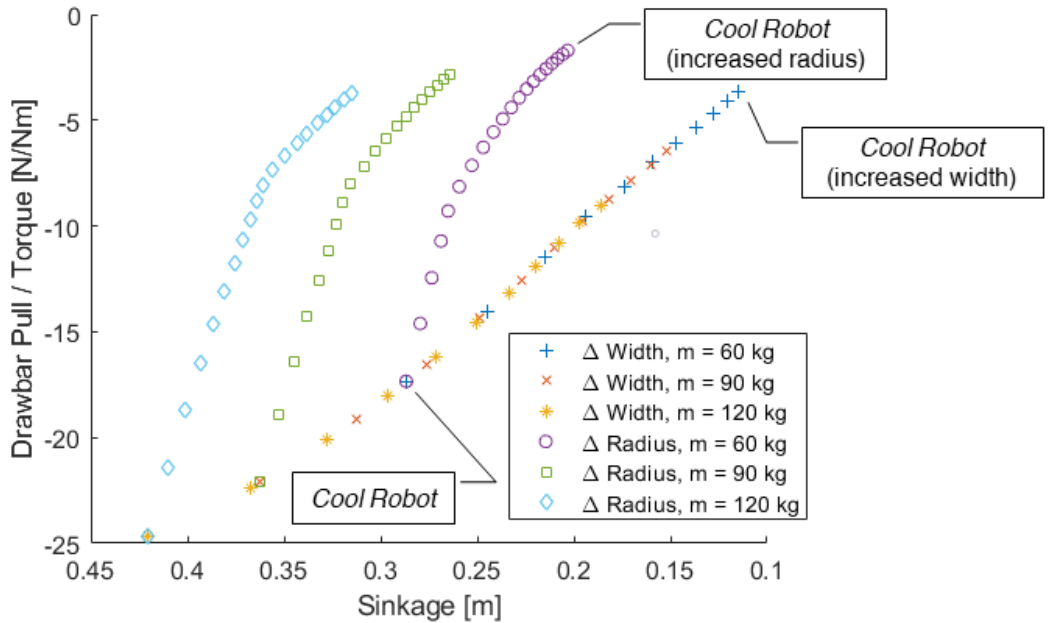


(a) Low stiffness, poorly bonded snow parameters

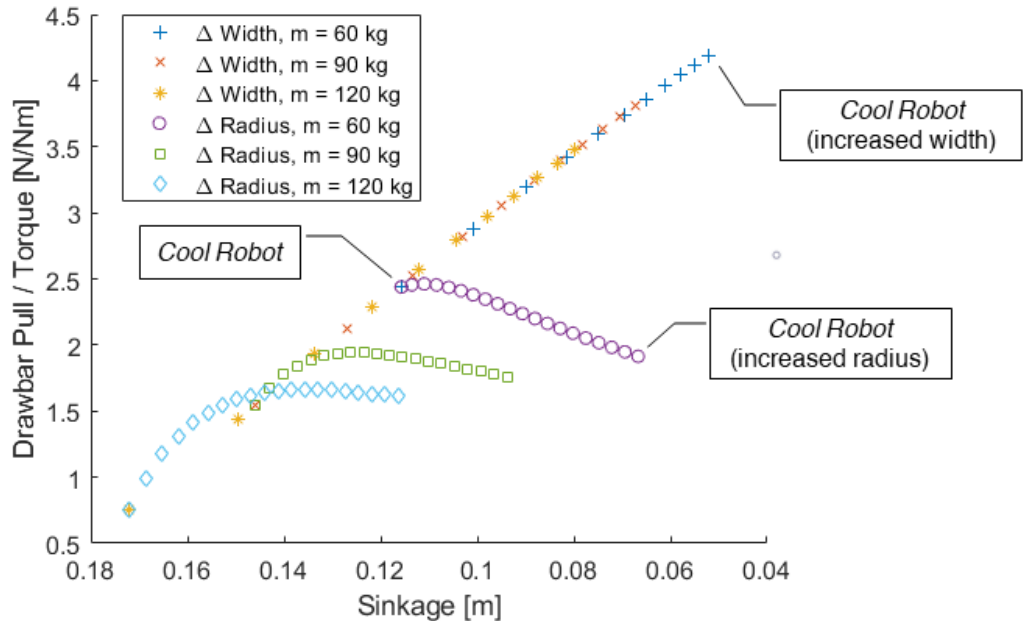


(b) High stiffness, well bonded snow parameters

Figure 3.7: Effect of changing wheel dimensions on resistance torque in two different snow types. In both figures, the wheel width,  $b$ , was increased from 0.1 m to 0.5 m and the wheel radius,  $r_w$ , was increased from 0.2 m to 0.5 m. Note that the x-axis scale is reversed, with left to right corresponding to a decrease in sinkage and an increase in wheel dimensions. Three different robot masses,  $m$ , were evaluated, seeing as changing wheel radius or wheel width would impact the rover's mass.



(a) Low stiffness, poorly bonded snow parameters



(b) High stiffness, well bonded snow parameters

Figure 3.8: Effect of changing wheel dimensions on the *mobility efficiency* factor (drawbar pull per torque required [N/Nm]) in two different snow types. In both figures, the wheel width,  $b$ , was increased from 0.1 m to 0.5 m and the wheel radius,  $r_w$ , was increased from 0.2 m to 0.5 m. Note that the x-axis scale is reversed, with left to right corresponding to a decrease in sinkage and an increase in wheel dimensions. Three different robot masses,  $m$ , were evaluated, seeing as changing wheel radius or wheel width would impact the rover's mass.

coefficient, the mobility efficiency factor normalizes the drawbar pull by the resistive torque to evaluate the usable torque given a design change in the wheel geometry. For the worst case terrain, increasing the radius of the wheels has a more pronounced impact on the mobility efficiency, but the wider wheels can achieve the same drawbar pull per torque specification as the large radius wheels, but with lower sinkage. Also, for the high stiffness, well bonded terrain, increasing the radius can actually decrease the mobility efficiency factor, whereas increasing the width increases this factor while also reducing the wheel's sinkage to a greater degree.

For all these reasons, it was decided that the redesigned wheels should have increased width rather than drastically increased diameter. The wheels of *Cool Robot* and *Yeti* only have a radius of 0.225 meters with an effective width of approximately 0.12 meters. Based on the results shown in Fig. 3.7 and 3.8, the new wheels were designed to have a slight increase in radius to 0.265 meters and almost a 4x increase in width, to be 0.45 meters wide. The same motor and gearbox that were used in *Yeti* could still be used with the new wheels due to the relatively small increase in predicted torque and the wheel weight staying approximately the same at 6 kg each. However, the shafts, bearings, and bearing blocks increased in mass to support the cantilevered load. All told, the robot, called *FrostyBoy*, increased in weight from *Cool Robot*'s  $\sim$ 60 kg to approximately 90 kg (a more detailed explanation of *FrostyBoy* is presented in section 5.2). Even with this increase in mass, the predictions shown in Fig. 3.8 still show an overall reduction in compaction resistance, an increase in drawbar pull, and a decrease in sinkage.

With such a wide wheel, bulldozing resistance becomes a larger factor in the overall resistance to motion. To counteract this force, grousers were added to the rim of the wheel to reduce the resistive forward flow of the snow. It has been shown that if the grousers interact with the soil before the wheel rim, marginal forward soil flow will occur [37]. While Inotsume's study [37] was performed in lunar regolith simulant, the grouser count

formula was still used to evaluate the design of the new wheel operating in snow

$$n_g > \frac{2\pi(1-i)}{\sqrt{(1-\hat{h})^2 - (1-\hat{z})^2} - \sqrt{1-(1-\hat{z})^2}} \quad (3.16)$$

with  $n_g$  being the minimum number of grousers to fully reduce the forward flow regime resistance,  $i$  being slip, and  $\hat{h}$  and  $\hat{z}$ , the height of the grouser and sinkage, respectively, normalized to the radius of the wheel. Off-the-shelf parts dictated the height of the grouser to be about 5% of the wheel radius and the overall geometry resulted in the wheel having 68 grousers. According to the equation above, this combination of  $\hat{h}$  and  $n_g$ , along with the approximate projected sinkage of 0.09 m for a 90 kg robot with a wheel width of 0.45 m (see Fig. 3.8) results in reduced bulldozing resistance for all values of wheel slip and resistance for slips greater than 30%.



Figure 3.9: Prototype of new wheel design with a 4x increase in wheel width compared to previous snow rovers.

These models were used to influence the final design and prototypes of the new wheels. The wheel is made up of two sidewalls that get rigidly mounted to a shaft, with the outer

diameter of the wheel being formed by aluminum U-channel grousers. The open sidewalls and gaps between grousers prevent snow from accumulating in the drum of the wheel, keeping it light and balanced. While these models serve well in predicting general trends in how modifying wheel dimensions will impact mobility and energy usage in low stiffness, low cohesion snow, their ability to predict performance improvements quantitatively is severely limited.



Figure 3.10: Sinkage comparison of snowmobile track (from top of photo to bottom left), *FrostyBoy* wheel track (from right to left side of photo - double wide), and a person's boot track (lower right). The boot sinkage is estimated to be about 3 to 4 cm, the snowmobile track  $\sim$ 1 cm, and the *FrostyBoy* wheels appear to sink less than the snowmobile. While this appears to be high stiffness snow, the relative sinkages serve as a sinkage test to understand *FrostyBoy*'s surface pressure.

The new rover, *FrostyBoy*, equipped with these prototype wheels was tested in the dry-snow zone of Greenland near Summit Station in 2018 and in over 80 km of towing an 80 kg sled of GPR equipment, the robot never became immobilized and was observed to have significantly less sinkage compared to *Cool Robot*. This serves as a qualitative analysis of the wheels, since snow conditions vary drastically from year-to-year and from month-

to-month in Greenland. Since no plate indentation or shear ring tests were performed, it is impossible to directly compare the number of immobilizations in 2017 with the lack thereof in 2018. However, the ability to tow a heavier sled for a significantly longer distance with zero immobilizations gives an idea of the improved performance. The sinkage of the wheels, relative to that observed for a snowmobile and a human on the same patch of snow, allows for direct comparison of surface pressure. As can be seen in Fig. 3.10, *FrostyBoy* sinks less than a snowmobile track ( $\sim 3.5$  kPa) in snow where normal boot pressure ( $\sim 60$  kPa) causes sinkage of about 3 to 4 cm. In addition, when *FrostyBoy* was driven up an incline of about  $20^\circ$  during the 2018 field season, the motors reached a current limit on the motor controllers that translates to approximately 40 Nm per wheel, meaning they were limited by the motor controllers and not by a limitation in their ability to gain traction, as no wheel slip was observed. Ultimately, modifying the tractive elements of the robot, using the existing terramechanics models to guide the new design, was shown to improve trafficability of the rover on snow and drastically reduce the chances of immobilization.

# **Chapter 4**

## **Mobility Prediction**

### **4.1 Introduction**

To replace manned traverses in the Arctic and Antarctica with autonomous rovers, incipient immobilization must be detectable. While modifying the tractive elements of the robot reduces the chances of immobilization, patches of low stiffness or low cohesion snow can still put an end to a traverse if the robot does not adjust to the changing conditions. If incipient immobilization can be detected, the control algorithm can then adapt to optimize traction in response to the terrain, choose an alternate route that potentially avoids the marginal terrain, or temporarily release a towed load until greater drawbar pull can be achieved [47]. It is critical that this detection is reliable over a range of terrain conditions since snow is highly variable in its material properties. This prediction must also be computationally simple enough to foresee alarming conditions in real time. Currently there is no existing vehicle-terrain model that adequately captures the pertinent dynamics of a rigid-wheeled vehicle traveling in snow that meets these reliability and speed requirements.

## 4.2 Existing Methods

A variety of approaches in predicting vehicle mobility have been utilized in autonomous, off-road applications. Oftentimes these methods are concerned with mapping the landscape and detecting obstacles for route planning and slope assessment. In these environments, LiDAR sensors can assess the topography and video images can be used in concert to judge whether the obstacles are compressible (such as a small bush or plant) and therefore passable, or should be avoided by charting a different route around them [48] [49] [50]. While this technology could be useful in avoiding large chunks of ice, mounds of snow, open crevasses, as well as in route planning up a slope, the primary concern when operating on a vast, flat, low contrast ice sheet is evaluating the properties of the terrain itself.

### 4.2.1 Terrain Models to Predict Mobility

Many methods exist for characterizing snowy terrain for trafficability, including a Rammsonde, a SnowMicroPenetrometer, and a drop cone [51], but one of the primary methods by which mobility is judged is through modeling of vehicle-terrain interaction and determining if the terrain conditions allow for enough tractive force. The development of these mobility models was largely supported by the United States military. Organizations such as the U.S. Army Engineer Research and Development Center (ERDC) and the U.S. Army Tank Automotive Research, Development, and Engineering Center (TARDEC) were interested in predicting the trafficability of tanks and armored vehicles [34]. Therefore, the models, such as the Nepean Wheeled Vehicle Performance Model (NWVPM) and the NATO Reference Mobility Model (NRMM) use classical Bekker-Wong theory, described in Ch. 3, for this class of vehicle [52] [53]. While the validity of these equations in predicting the mobility of lightweight vehicles with smaller wheels is touched on in the previous chapter and further explored in section 4.2.2, assuming these models were 100% accurate, there is still the issue of accurately determining the terrain properties needed as inputs to the Bekker-Wong

equations. These parameters typically require a plate-sinkage device to determine pressure vs. depth characteristics and a shear ring or shear plate test to find cohesion, angle of internal friction, and the shear displacement modulus. Yet, this still does not result in the full suite of parameters, seeing as without a full-blown single-wheel testbed and particle tracking video system,  $c_1$  and  $c_2$  in Eq. (3.3) must be estimated from the literature. Vehicle mounted bevameters and vehicle mounted single-wheel field testers have been developed to evaluate these properties semi-autonomously *in situ* [54] [55] [56]. A similar method that removed the need for additional, specialized equipment on-board the vehicle was developed by NASA in using one of the Mars rover Sojourner's wheels as a trenching device to determine a subset of the terrain parameters [57]. While these methods prove to be effective in characterizing terrain and comparing actual mobility with predicted mobility from the model, they cannot prevent immobilization. These measurements require the vehicle to stop, meaning the loss of all forward momentum, and they assume low spatial variability of the terrain, since these are only point measurements. Since snow has been found to have a high degree of spatial variability from bevameter tests performed manually [58], this method would not work in predicting mobility of the rover even one wheel rotation beyond the test location.

To evaluate trafficability of the terrain in real-time as the rover is in motion, researchers turned to extracting terrain parameters using proprioceptive sensor measurements. One method proposed by Iagnemma could approximate the cohesion and friction angle of a terrain by measuring each wheel's normal load, torque, sinkage, angular speed, and longitudinal speed [59]. These parameters could then be fed into simplified Bekker-Wong equilibrium equations to estimate a rover's mobility on the terrain being encountered. One problem with this method is that in order to calculate closed-form solutions to the equilibrium equations (3.11)-(3.13), simplifications need to be made to the normal and shear stress distributions at the wheel-terrain interface. Iagnemma assumes this stress distribution to be symmetric, sets  $\theta_2$  to zero degrees, and also presumes  $\theta_m$  to be exactly halfway between

$\theta_1$  and  $\theta_2$ . Wong and Reece proved experimentally that this symmetry only occurs at one value of slip, with parameters  $c_1$  and  $c_2$  defining how the maximum stress moves based on the wheel's slip ratio (3.3) [31]. Since all terrain-wheel interaction forces are based on these stress distributions, errors due to this simplification can have significant impacts on determining mobility. This method also suffers from the issue of non-uniqueness in determining terrain parameters using sensor measurements and from the need for a significant number of data points before the model converges. Assuming a perfectly accurate understanding of the normal pressure distribution below a wheel, as well as an exact calculation of drawbar pull for that wheel, the cohesion parameter,  $c$ , and the angle of internal friction,  $\phi$ , both contribute to the shear stress according to Eq. (3.7), with significantly different impacts on mobility with varying slip ratios (see section 6.3.3). Therefore, multiple data points need to be employed to extract each parameter's respective value. Another problem with this approach is that torque and normal load are typically not directly measured for wheeled mobile robots (WMRs), as this would require a multi-axis force sensor in each wheel adding significant complexity, cost, and mass to a rover. Since these inputs are estimated from a quasi-static analysis based on mass distribution and from current supplied to the motor, the approximations will be inherently noisy or inaccurate. In trying to account for sensor noise, Iagnemma corrupted the inputs with white noise and this, combined with the issue of non-uniqueness, necessitated at least thirty measurements before the model would converge [59]. Depending on the sampling rate and speed of the rover, the need for thirty samples before convergence could require a long stretch of homogeneous terrain to obtain an accurate estimate of mobility and provide an ample time window for the robot to lose all traction. For his application, where the robot was traveling at only 5-10 cm/s, the sensor sampling rate was 5 Hz, and the terrain can be assumed to be somewhat homogeneous, this method could provide adequate warning. However, for *FrostyBoy* traveling at 1-2 m/s, sampling at 10 Hz, and on highly variable terrain, all four wheels could be immobilized by the time the model converges.

Other online estimation methods have relied on specific maneuvers to be performed by the rover before parameters can be estimated. Specifically, Ojeda required a robot to perform turns at varying yaw rates while measuring motor currents in order to develop an analog to the shear-stress vs. shear-displacement curve [60]. Another study conducted by Liu extracted terrain parameters only when a WMR was skidding (negative slip) down a slope [61]. Both these methods prove limited in their application since requiring the rover to perform turns could actually incite an immobilization event, downhill slopes are not guaranteed nor likely on a flat ice sheet, and the parameters estimated during these maneuvers may not be applicable to upcoming terrain.

All of the methods mentioned up to this point suffer from the same four drawbacks in predicting mobility.

1. They require an assumption that the terrain is homogeneous to make accurate predictions about future mobility.
2. They only calculate a subset of the terrain parameters, with average values assumed for the remaining terrain parameters.
3. They require simplifications of the pressure and shear stress distributions at the wheel-terrain interface to solve the Bekker-Wong equilibrium equations in real-time.
4. The terrain parameters are inextricably linked in their contribution to mobility and cannot be uniquely identified from single force measurements or estimates.

To solve these issues and predict mobility in very inconsistent terrain, Ray [6] employed Bayesian multiple model estimation (MME) to evaluate the most likely set of terrain parameters that could describe the robot's sensor readings. In this method, Ray uses multiple hypotheses of almost a complete set of terrain parameters ( $\theta_2$  is assumed to be zero degrees) as inputs to the Bekker-Wong equilibrium equations to generate expected forces from the terrain on a rigid-wheeled, lightweight rover [6]. The forces estimated through an

Extended Kalman-Bucy Filter (EKBF) from the proprioceptive sensor measurements of the wheels can then be compared to those generated from the hypotheses, and the most likely set of terrain parameters can be determined based on their conditional probability given the measurements. Even though Ray tested this method on simulations of a constant terrain type, she found that this method converged very quickly to the closest terrain parameter hypothesis, within two iterations of the MME algorithm, even when no hypothesis was an exact match of the terrain parameters being simulated [6]. As Cook found, this rapid convergence meant Ray's method was effective in detecting terrain parameters quickly in non-homogeneous snow, allowing traction control methods to be developed to maintain mobility in changing conditions [47]. Cook also included the shear deformation modulus,  $K_s$ , in his terrain parameter hypotheses, meaning one fewer parameter that is fixed to the average value found in the literature [47]. The third drawback of previous methods is also solved, since the force-slip curves generated for each hypothesis can be calculated numerically ahead of deployment, meaning that no simplifications to the Bekker-Wong equations (3.11) - (3.13) are necessary for the algorithm to run in real time. However, the issue of non-uniqueness still plagues this method, as Ray found overlap in differentiating high-cohesion soils in her simulations and Cook's algorithm had difficulty differentiating between his 320 different hypotheses at low slip ratios in snow [47].

### 4.2.2 Drawbacks of Terrain Models

While the MME method is effective at rapidly converging on a set of terrain parameters, the forces these terrain parameters predict and the resulting mobility judgment are still rooted in the Bekker-Wong terramechanics model. As discussed in Ch. 3, this model was developed for heavier vehicles, with larger wheels, operating in sands and soils. Modifications to the model have been proposed to better fit the data from lightweight vehicle tests, but these often add parameters to the existing set, are not specific to snow, and none of these adaptations have been universally adopted. In addition, there are observable effects that

cause immobilization which are not considered in these models.

The primary effect that is not considered is the dynamic sinkage that occurs from excessive wheel slip and the resultant excavation of terrain. The model relies on an accurate definition of the pressure distribution below a rigid wheel to accurately predict a vehicle's mobility. This distribution defines the overall sinkage and therefore the compaction resistance and resistive torque applied to the wheel by the terrain. However, while Reece's equation (3.3) takes into account the radial movement of the angle of maximum stress,  $\theta_m$ , based on the wheel's slip, there is no equation that redefines the pressure distribution after slip-sinkage occurs. The boundaries of the contact patch are also poorly understood when slip-sinkage occurs. Even in Ray's study,  $\theta_2$  was assumed to be directly below the wheel axle, but it has been experimentally shown in single-wheel studies that at higher slip ratios, the backward flowing zone of soil under the wheel enlarges until at 100% slip, there is no forward flowing zone and  $\theta_2$  is much less than  $0^\circ$  (see Fig. 4.1) [2]. This slip-sinkage effect

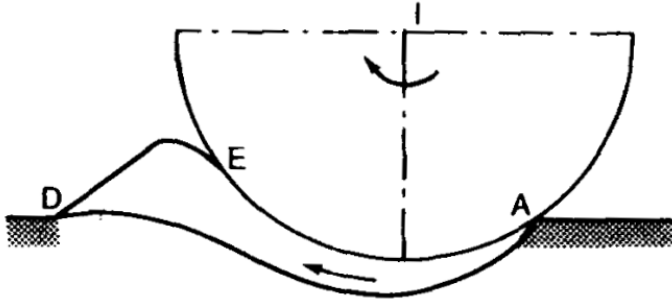


Figure 4.1: Flow pattern beneath driven wheel at 100% slip [2].

was the primary cause of *Cool Robot*'s immobilizations observed in the 2017 field season near Summit Station, Greenland. The robot would encounter a patch of low cohesion, low stiffness snow. While making very little forward progress, the robot wheels would slip and dig themselves deeper until the chassis was touching the snow surface (see Fig. 4.2). While Lyasko's simple prediction of additional sinkage due to slip (3.15), as proportional to initial sinkage, serves as a good approximation, it does not consider how slip-sinkage develops over time. The vehicle-terrain interaction has been observed to be more complicated when

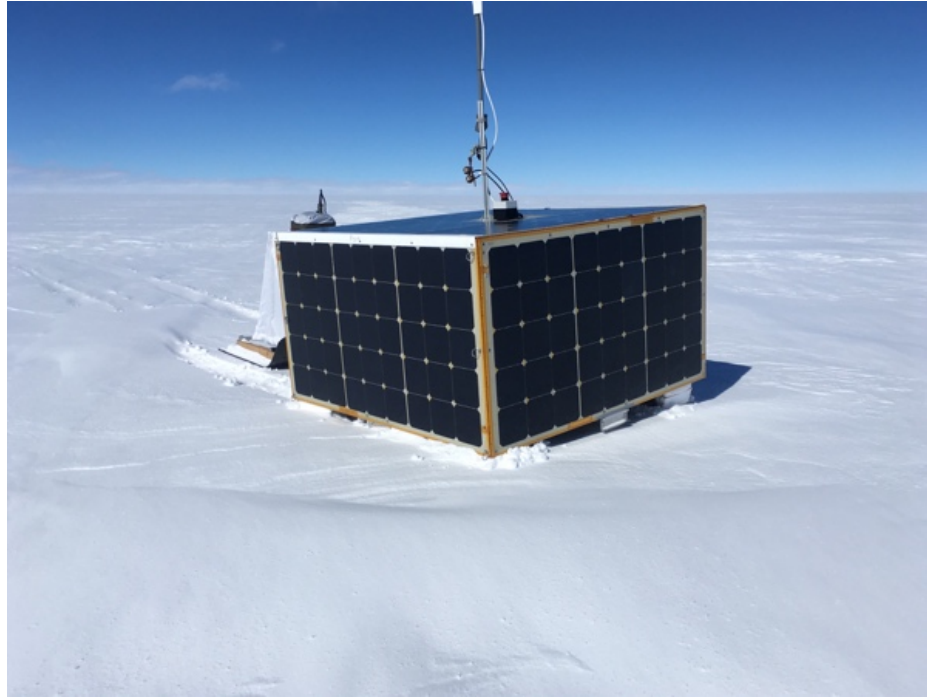


Figure 4.2: Immobilization of *Cool Robot* due to slip-sinkage effect.

this slip-sinkage effect occurs [62].

With so many caveats and deviations of the terrain models from the reality of how lightweight, wheeled vehicles operate in snow, a new immobilization detection method needs to be developed that will capture the dynamics of the system without relying on unknown and marginally applicable terrain parameters.

### 4.2.3 Other Methods

One such method of predicting mobility avoids the problems inherent in measuring or estimating terrain parameters by instead using a machine learning approach. Trautmann [63] used classified proprioceptive sensor data during normal operation and immobilization events of a rover on snow to train a machine learning algorithm. Instead of a terramechanics model, it relies on supervised learning of a support vector machine for deciding whether the terrain being traversed is a threat to mobility. This method was proven experimentally using *Yeti*, instrumented with encoders and current sensors on each motor, an

IMU, and an optical ground speed sensor. The machine learning approach proved to be very effective in predicting a loss of traction, however the large training data set required renders it impractical. This method is ‘expensive’ for the operator, as Trautmann hand labeled the robot sensor measurements to characterize them to be one of three conditions: fully mobile, almost immobilized, or immobilized. In addition, field seasons to collect this data are typically short and costly and many examples of the robot’s performance on both immobilizing and traversable terrains are required for a robust model.

### 4.3 New Mobility Prediction Method

The objective of the work presented in the following chapters is to develop a mobility prediction method that does not rely on estimating terrain parameters, can run in real time, and is not predicated on an enormous amount of training data. It also must be reliable enough to detect an immobilization in a wide variety of terrain conditions, as snow has been observed to be highly variable. There are two main components in developing the algorithms to detect an incipient immobilization. The first component is the real-world data collection, which involves instrumenting a four-wheeled rover with proprioceptive sensors and logging their measurements during forced immobilizations, similar to the *in situ* testing performed by Trautmann [63]. However, instead of being used to train a machine learning algorithm, these data are used to develop a truth model, the second component of this method. This truth model, although rooted in Bekker-Wong terramechanics, is enhanced by the real-world observations to mimic the robot’s dynamics. Both of these components, the collected data of the rover losing traction and the simulated data of the modeled rover becoming immobilized, are then used to develop the detection algorithm that can warn the rover of an impending mobility loss. This proposed method has many advantages when compared to the state-of-the-art immobilization prediction approaches. The models for nominal operation, and those characteristic of an immobilization, will be derived directly

from data measured with the pertinent robot operating in the range of terrain types for which it was designed. This eliminates all the problems, elucidated above, of determining just how well the most recent advances in terramechanics models apply to lightweight rovers in low cohesion terrain, particularly the widely neglected terrain of snow. There are no integrals that must be iteratively solved, no large set of terrain parameter combinations that must be evaluated, and no mathematical uniqueness issues. Translating empirical relationships formulated for heavy vehicles to lower surface pressures or slip-sinkage equations developed in sand to snow proves unnecessary. Most importantly, the effect of slip-induced sinkage on terrain resistance and drawbar pull, which has been identified as a primary cause for immobilization, is captured just by nature of analyzing real data collected when this phenomenon played a key role. The method will also go beyond single-wheel studies, by considering the role all four wheels play in a loss of traction. With an accurate truth model, these algorithms can also be tested on new scenarios and new terrains, not tested with the instrumented robot. This allows for a small data set, meaning a less costly, shorter field season for collecting these data, to provide a broadly applicable incipient immobilization detection method.

# **Chapter 5**

## **Methodology and Findings**

### **5.1 Introduction**

Collecting proprioceptive sensor measurements on an instrumented robot operating in snow is a critical step in developing a truth model of the rover’s interaction with the terrain and algorithms with which immobilization can be predicted. The goal is to collect information about the dynamics of the rover and its interaction with the terrain to be able to help formulate and validate the simulations. Since the truth model is primarily based on the wheel-terrain interaction defined by the Bekker-Wong model, terrain parameters need to be measured to serve as inputs to these equations. The overarching goal for this data collection phase is to find a signature of immobilization that is easily separable from the nominal operating conditions that can be used to warn of an upcoming loss of mobility even in highly variable terrain.

### **5.2 Instrumentation**

Measurements of robot ground speed, roll, pitch, and yaw rates, motor currents, motor speeds, sinkage at each wheel, longitudinal and lateral accelerations, as well as drawbar load were logged during outdoor tests on relevant terrains. The robot, *FrostyBoy*, men-

tioned in previous chapters and shown in Fig. 5.1, was used for this testing. It is similar to *Yeti* and *Cool Robot* in that it has four electric motors (identical motor and gearbox combination to *Yeti*) that are powered by lithium ion batteries, optionally charged by solar panels towed behind on a sled. *FrostyBoy* is heavier than the other two robots with a mass of about 90 kg. Its chassis is constructed of T-channel aluminum extrusion, with a pivot on the front axle to give the robot some compliance about the roll axis and  $\pm 9^\circ$  about the yaw axis to reduce lateral bulldozing resistance in a skid-steer turn. The heavier chassis is necessary to support the wider wheels (described in section 3.7). This robot has been operationally tested in Greenland during a 2018 and a 2019 field season [64]. After the 2019 field season, the robot was outfitted with sensors to measure the parameters listed above. The ground speed, as well as accelerations of the robot, are derived using the VectorNav VN-200 GPS-aided Inertial Navigation System (INS) mounted on the robot chassis with built-in Kalman filtering algorithms to improve accuracy. This device can measure accelerations with a resolution less than 0.5 mg and has velocity accuracy of less than 0.05 m/s. Roll and pitch accuracies have a standard deviation of  $0.03^\circ$  and heading accuracy, when moving, has a standard deviation of  $0.2^\circ$ . The motor currents and motor speeds were read using the RoboteQ FBL2360 brushless DC motor controller. Sinkage at each wheel was measured with OMEGA LVU-32, non-contact, ultrasonic level transmitter. This sensor detects distances from 0.1 to 2.4 meters with a resolution of 0.25 mm. With a relatively narrow, conical beam of only 8 degrees, these sensors are mounted next to every wheel axle on the body of the robot. Although tested in the lab, these ultrasonic sensors did not function properly during field tests and therefore no data from these sensors will be used or presented in this thesis. An INTERFACE STA-3 S-beam load cell with a rated load of 4900 N and an accuracy of  $\pm 1$  N was mounted on the tow point of *FrostyBoy* and measured the instantaneous force required to move a weighted sled. All sensor data was logged by a Campbell Scientific CR1000X configured with a CFM100 CompactFlash Memory Module.



Figure 5.1: *FrostyBoy* shown in Greenland during the 2018 field season in the dry snow zone towing a sled carrying solar panels and a GPR unit.

In addition to the on-board sensors that would supply data for immobilization detection, the terrain also needed to be characterized in terms of the Bekker-Wong model parameters to better understand where it fits in the range of snow types. A bevameter cannot be readily obtained off the shelf, as they are typically custom made and uniquely calibrated. They also require an expensive multiple-degree-of-freedom, force-torque sensor and a shear annulus with specific geometry in order to measure both pressure-sinkage as well as shear parameters. Since the purpose of the measurements was for broadly characterizing the snowpack and not to exhaustively match experimental data with Bekker-Wong parameters, a much less expensive, field deployable device that only measured the pressure-sinkage curve was designed. This device, known as the Ground Pounder (GP), had legs that could either sit on the surface of the snow with the optional feet added, or could be extended up to 1 meter to plunge through the soft layers of snow and rest on a hard layer beneath the surface. A battery-powered drill attaches to the drive shaft, which drives a lead screw (600 mm stroke, 5 mm lead), ultimately driving a plunger, with a 10.2 cm diameter round puck on one end, into the snow (see Fig. 5.2). The required force to drive the plunger into the snow was mea-

sured with an OMEGA LC703-50 miniature load cell (with linearity of  $\pm 0.15\%$  of its 23 kgf max capacity). Depth was calculated using a rotary encoder on the drive shaft (model 15T with 1800 CPR). The data were output from an Arduino Due's USB communication port at 11 Hz and recorded on a connected laptop. The battery-powered drill was run at maximum speed to limit the effect of acceleration on the force measurements.

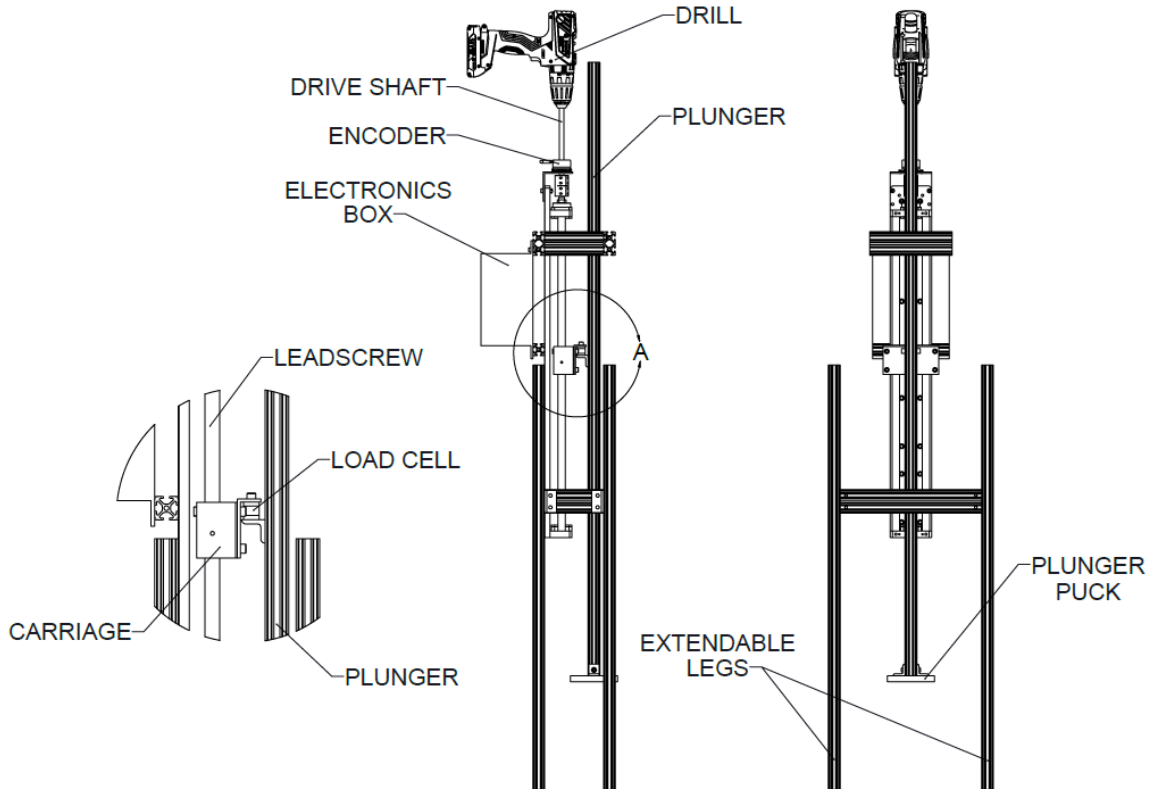


Figure 5.2: Labeled drawing of Ground Pounder device to measure pressure-sinkage profile.

### 5.3 Data Collection

In order for canonical models of the rover's dynamical behavior to be developed, proprioceptive sensor data needed to be collected during the transition from steady-state operation to its complete loss of forward velocity. For this transition to happen naturally requires a unique snowpack in which the robot is constantly on the verge of becoming immobi-

lized and small changes in the cohesion or sinkage can bring the robot to a halt. This low cohesion snow was observed in the 2017 field season at Summit Station, Greenland with *Cool Robot* losing traction approximately once every kilometer. Finding this type of snow was critical in capturing the slip-sinkage effects and unique dynamics that can result in immobilizations instead of forcing immobilization by driving up a slope, as was done by Trautmann in order to collect enough data for training an SVM [63]. The snow for testing also had to be deep enough that the pressure bulb radiating down through the snow from the wheel-terrain interface would not intersect a rigid interface below the snow. While this is largely dependent on the surface pressure applied to the terrain by the vehicle, and therefore the weight of the vehicle and size of its wheels, the rule of thumb for choosing a suitable test site was that the snow had to be deeper than two thirds of the wheel radius [29]. The final requirement for testing was that the air temperature had to remain well below 0° C during data collection so melting did not play a role in altering the terrain properties.

The search for these very specific conditions proved difficult in the immediate area around Dartmouth College and therefore required transport of the equipment to locations where the snow conditions were unknown, but weather data and snow depth measurements looked promising. The logistics involved in moving the equipment and issues with availability of spare parts at remote testing sites further reinforced the need for a method of detecting immobilization that doesn't require a large training data set. The data, used in the results and analysis that follows, were collected in two locations outside of Lebel-sur-Quévillon in Québec, Canada in March of 2020 that met the above requirements. The first test site was a small, flat, open area of deep snow (over 75 cm deep) that was sheltered from wind by surrounding trees (test site #1). This snow was not measured with the GP, but qualitatively found to have very low stiffness with normal boot pressure (approximated to be 60 kPa) resulting in sinkage of 75 cm or more. No measure of cohesion was performed, but the snow was qualitatively loose and unconsolidated. Another day of testing was done on the nearby lake (test site #2), which provided a very expansive and flat area for experi-

ments with the rover. This snowpack, characterized with the GP, was not as deep and not as compressible as the snow at the first site, but sufficiently met the requirement of ‘deep snow’. This snow was similarly unconsolidated in the morning, when all immobilization tests were performed, but as the ambient temperature rose above 0° C, the cohesion of the snow was able to be modified with compaction.

Three main tests were performed. The first and most important test was collecting sensor data during an immobilization event. At each test site, *FrostyBoy* was run in an open-loop speed control configuration in which all four motor controllers sent the same voltage to each of the four motors. This speed/voltage command was ramped up manually over the course of two to three seconds from a remote, control station until reaching a defined setpoint, usually around 40% of full speed. This setpoint percentage corresponds to the proportion of the motor’s rated voltage of 48V that is to be applied by the motor controllers and was recorded in a log file on the control station. The rover was left to operate at this voltage, tracking relatively straight, until it became naturally immobilized by what can only be deduced are natural variations in the snow properties, since the snow appeared highly uniform and completely undisturbed from the surface. In addition to the on-board sensor data, the speed commands sent to the rover were also logged, and pictures of the robot were taken after it became immobilized.

The second test involved characterizing the terrain with the GP. Overall, six pressure-sinkage curves were generated with the GP at the lake (test site #2). The first two were taken approximately 10 meters apart in the general area of testing before the robot was operated (GP Data 1 and GP Data 2). Two were taken near the front left and front right wheels of *FrostyBoy* (GP Data 3 and GP Data 4) immediately after one of the immobilization events, meaning that they were measuring pressure-sinkage properties of the snow that caused the immobilization and were separated by only ~2 meters. The last two were taken once the ambient temperature climbed above 0° C and, due to the drastic impact this had on the snowpack and the operation of the rover, these data will not be considered in the analysis.

The third test was performed to see how the rover could induce a change in the terrain parameters through repeated passes over the same path and the resultant increase in drawbar pull due to this modification. This final experiment was far less rigorous and merely meant to serve as a qualitative affirmation that a control sequence could be developed to improve traction once incipient immobilization is detected to lay the groundwork for further research in this area. In this test, the robot was pushed out of its rut after getting stuck and commanded to drive over its previous tracks to see if the sensor data showed a difference in trafficability.

## 5.4 Results

In order to properly understand the results from these tests, one must first understand the convention in which these data are presented. The sensor data are converted to a body-fixed reference frame with the longitudinal axis represented as the  $x$ -axis, with positive in the forward direction, the lateral  $y$ -axis being positive towards the left of the robot, and the  $z$ -axis being positive pointing away from the ground as shown in Fig. 5.3. The sensor data from the two days of testing were split into individual immobilization events and the raw sensor measurements were translated into plots of the relevant variables. Since the IMU outputs velocity in terms of North and East rather than  $x$  and  $y$  according to the convention presented above, these measurements were translated to longitudinal and lateral velocity using the IMU's heading measurement. Before the heading measurement could be used, yaw drift had to be accounted for by matching the yaw signature when the rover was in motion with the velocity vector direction to determine yaw offset. The absolute speed over ground of the left wheels and the right wheels were calculated according to the equations

$$v_L = v_x - \frac{t_w}{2} \dot{\psi} \quad (5.1)$$

$$v_R = v_x + \frac{t_w}{2} \dot{\psi} \quad (5.2)$$

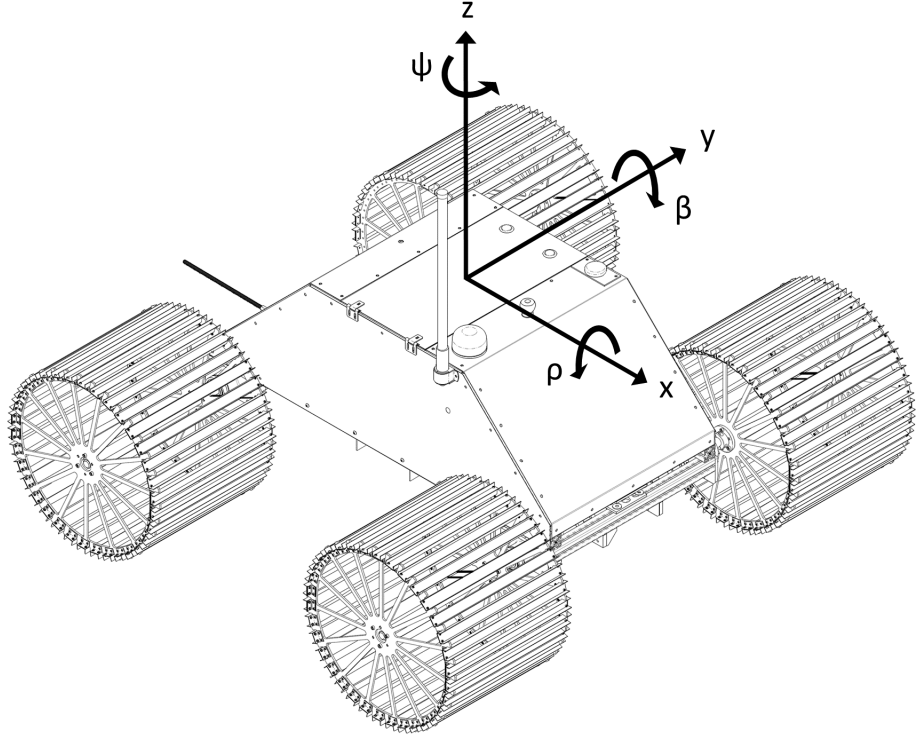


Figure 5.3: Body-fixed reference frame convention, with  $x$ ,  $y$ , and  $z$  defining the longitudinal, lateral, and vertical axes, respectively, and  $\psi$ ,  $\beta$ , and  $\rho$  defining the yaw, pitch, and roll angles.

where  $v_x$  is the longitudinal speed of the rover's center of mass,  $\dot{\psi}$  is yaw rate, and  $t_w$  is the lateral distance from the center line of the left wheel to the center line of the right wheel. The slip of each wheel could then be calculated from converting motor speeds to wheel speeds, using the 40:1 gearbox speed reduction factor, and then comparing the longitudinal wheel speeds over ground with the linear speed of the wheel's outer rim according to

$$i = \begin{cases} (r_w\omega - v)/r_w\omega & |r_w\omega| > |v| \\ (r_w\omega - v)/v & |r_w\omega| < |v| \end{cases} \quad (5.3)$$

with  $r_w$  being the wheel radius of 0.265 m and  $v$  being the longitudinal velocity of the left or the right side of the vehicle,  $v_L$  or  $v_R$  respectively. Wheel torques were also not measured directly, but instead, measurements of current supplied to the motors were translated to torque at the wheels by using the motor's torque constant, multiplying by the gearbox

ratio, and scaling down by an assumed 80%<sup>1</sup> efficiency for a two-stage planetary gearbox. Instantaneous longitudinal forces per wheel could only be derived by using the instantaneous acceleration measured by the IMU, the gravity resistance force calculated using the pitch angle, and averaging this evenly between the four wheels. The sinkage sensors failed to provide any usable measurements in the two days of testing. They will not be presented in this section and cannot be used in predicting immobilization. While this was an unintended result and these measurements would have been valuable in characterizing the snowpack and slip-sinkage effects, the ability to predict immobilization without relying on sinkage measurements will prevent the need for outfitting rovers with these expensive ultrasonic sensors at each wheel or outfitting each wheel with a camera, as proposed by Iagnemma [65]. Sinkage measurement for this data set can only be done using pictures taken after immobilization events at test site #2.

The most important findings from these data were the easily discernible patterns and signatures from slip, wheel speed, and torque measurements that have the potential to predict and prevent immobilization. The rover became immobilized frequently at both test sites, typically traveling less than 20 meters before becoming stuck, even without any towed load. The pattern observed in every one of these immobilization events was an increase in torque and decrease in wheel speed for two of the wheels and a decrease in torque and increase in wheel speed for the other two wheels. The wheels showing the same behavior were always at a diagonal to one another. An example is shown in Fig. 5.4 with the front right and rear left wheels exhibiting the same behavior while the front left and rear right wheels exhibit the opposite behavior. As shown in this example, two of the wheels' torques climb to the motor controllers' current limit restriction as their rotational speeds drop to zero (the oscillations observed in the torque record is an artefact of the motor con-

---

<sup>1</sup>Neugart gives a maximum efficiency rating of 94%, however this is at the optimal operating conditions: a gearbox temperature of 70° C, an output torque of 40 Nm, and an input speed of 1000 RPM. The drop off of efficiency at varying loads, input speeds, and lower temperatures (with a low-temperature grease) were not provided. Therefore, a conservative efficiency reduction of 10% per stage for the two-stage planetary gearbox was used in all calculations.

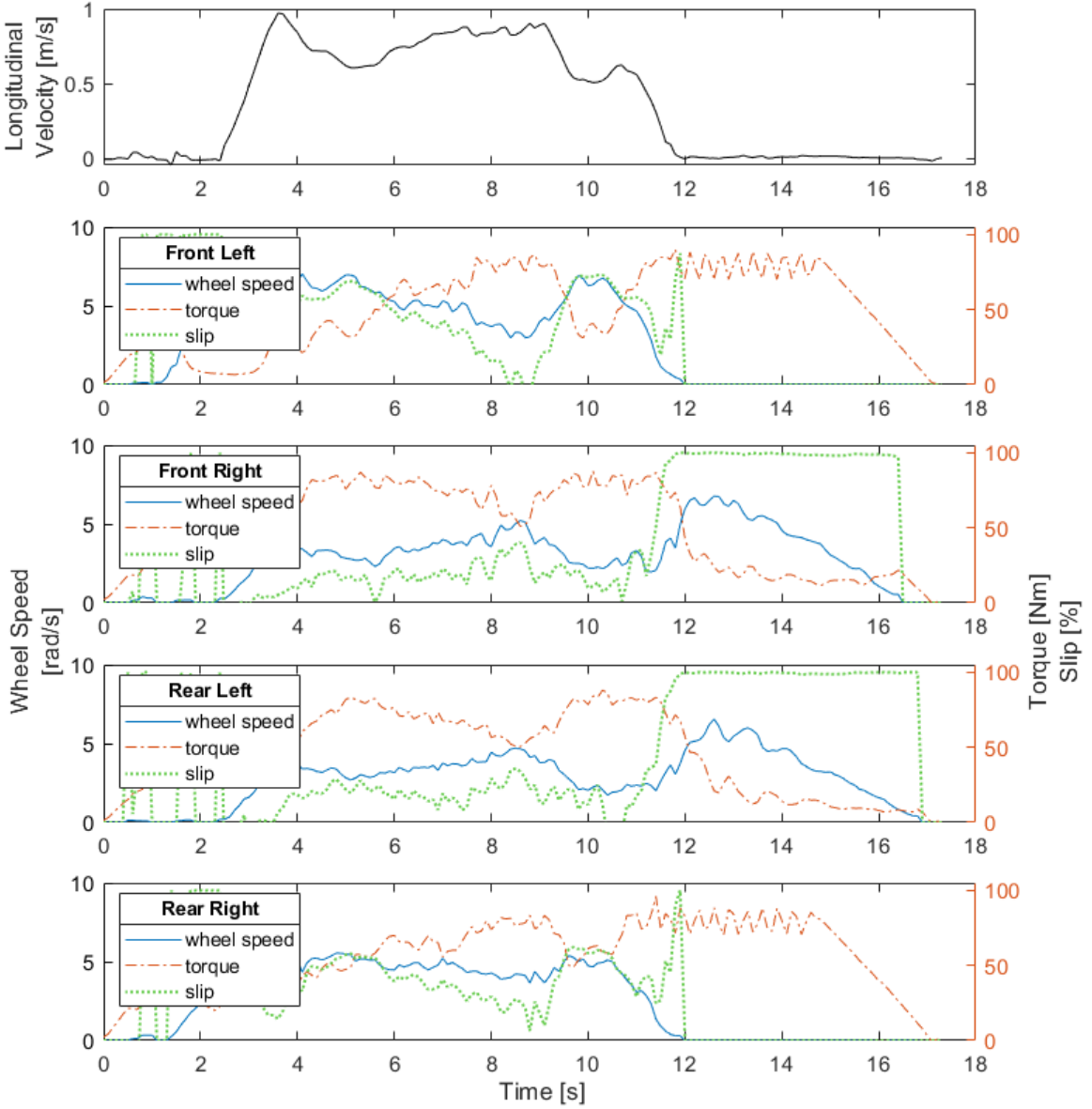


Figure 5.4: Data from a typical immobilization event, with the top graph showing longitudinal velocity of the rover,  $v_x$ , and the four subsequent graphs showing wheel speed,  $\omega$ , wheel torque,  $T$ , and wheel slip,  $i$ , for each of the four wheels. This example clearly shows that the front left and rear right wheels stalled and the front right and rear left wheels reached 100% slip.

trollers' programming to prevent the motor from overheating by dropping the current by a set amount each time the current limit of 40 amps is reached). The other two wheels' rotational speeds increase as their torques decrease, appearing to almost reach a no-load condition that also results in their slip ratios jumping up quickly to 100%. Figures 5.5

and 5.6 show other observed characteristics of these immobilization events. One is that the two wheels with high slip ratios are observed to excavate the terrain below the wheels, evidenced by the buildup of snow behind them. It is also evident from these photos that there is significant snow ‘trapped’ inside the frames of the two stalled wheels, which adds to the resistance torque. The robot pitching up is another signature of this event which can be seen in Fig. 5.6. While this added resistance, due to gravity, can be accounted for using the pitch angle measured by the IMU and knowledge of the robot’s center of mass, it serves as valuable insight into modeling the dynamics of these immobilizations. Specifically, this example shows that immobilization events are not only impacted by the vehicle-terrain interaction, but also depend on the vehicle’s rigid-body dynamics. The cause of immobilization can therefore not be completely understood by single-wheel studies, and full system testing must be performed to be able to detect incipient immobilization (discussed further in Ch. 6).

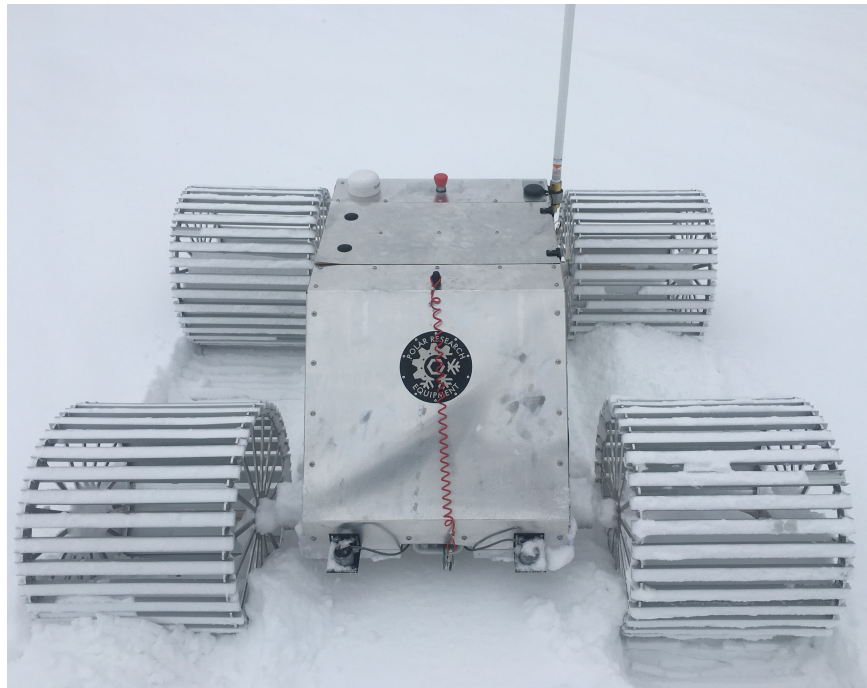


Figure 5.5: Top view of *FrostyBoy* after becoming immobilized at test site #2. Data for this immobilization are presented in Fig. 5.4. Note the build up of excavated snow behind the front right and rear left wheels.



Figure 5.6: Side view of *FrostyBoy* after becoming immobilized at test site #2. Data for this immobilization are presented in Fig. 5.4. Note the front of the robot (antenna side) is clearly pitched up relative to the horizon line.

To further understand the cause of this complete loss of mobility, we can look at the data collected from the GP to better grasp the pressure distributions below the wheels. The four sets of pressure vs. sinkage measurements are shown in Fig. 5.7 with the best-fit Preston-Thomas (3.6) pressure-sinkage curves plotted over them. The values for these best-

Terrain Parameters Fitted to GP Data						
Parameter [Units]	$k$ [ $\frac{\text{kPa}}{\text{m}}$ ]	$z_m$ [cm]	$k_c$ [ $\frac{\text{kN}}{\text{m}^{n+1}}$ ]	$k_\phi$ [ $\frac{\text{kN}}{\text{m}^{n+2}}$ ]	$n$	$R^2$
Data 1 - Preston	65.0	29.1	-	-	-	0.96
Data 1 - Bekker	-	-	165.3	130.8	2.88	0.99
Data 2 - Preston	56.4	34.6	-	-	-	0.98
Data 2 - Bekker	-	-	70.9	90.6	2.41	0.98
Data 3 - Preston	27.3	49.6	-	-	-	0.93
Data 3 - Bekker	-	-	26.9	12.7	2.15	0.81
Data 4 - Preston	19.2	54.0	-	-	-	0.92
Data 4 - Bekker	-	-	17.1	8.0	3.60	0.72

Table 5.1: Comparison of the best-fit Preston-Thomas (3.6) and Bekker (3.2) pressure-sinkage parameters and coefficients of determination collected with the GP at test site #2.

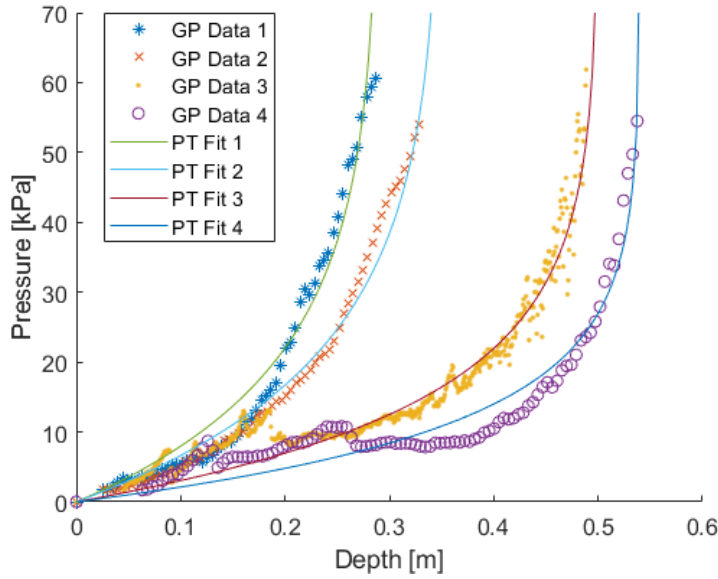


Figure 5.7: Pressure-sinkage data from the Ground Pounder collected at test site #2 in Lebel-sur-Quévillon, with the best-fit Preston-Thomas curve (3.6) shown for each data set. Data sets 1 and 2 are taken  $\sim 10$  meters apart before the immobilization trials started. Data sets 3 and 4 are taken immediately after an immobilization event, just to the left and right sides of the front rover wheels. The Preston-Thomas curve parameters and measures of fit are presented in Table 5.1.

fit curves,  $k$  and  $z_m$ , as well as their coefficients of determination, are shown in Table 5.1. For comparison, the coefficients of determination for the best-fit Bekker (3.2) pressure-sinkage curves are also presented in Table 5.1, showing that for some of the curves, the Bekker model provides a marginally better fit or matches the fit of the Preston-Thomas model. However, since the Bekker model relies on multiple tests with differently sized plates to bound its defining parameters yet only one plate size was used on the GP, and because the Bekker model only offers an incremental improvement in fitting the data for one of the four curves, the Preston-Thomas model will be used for the remainder of the analysis and the best-fit Bekker curves are not shown in Fig. 5.7. It is also evident from these data that this is the most compressible terrain evaluated in Ch. 3, having low values of  $k$ , meaning high sinkage for relatively low pressures, and having high values of  $z_m$ , meaning that compression against a harder layer of snow happens at a greater depth than that observed in Greenland by Lever in 2006 (shown in Fig. 3.3) [5]. Table 5.7 also shows

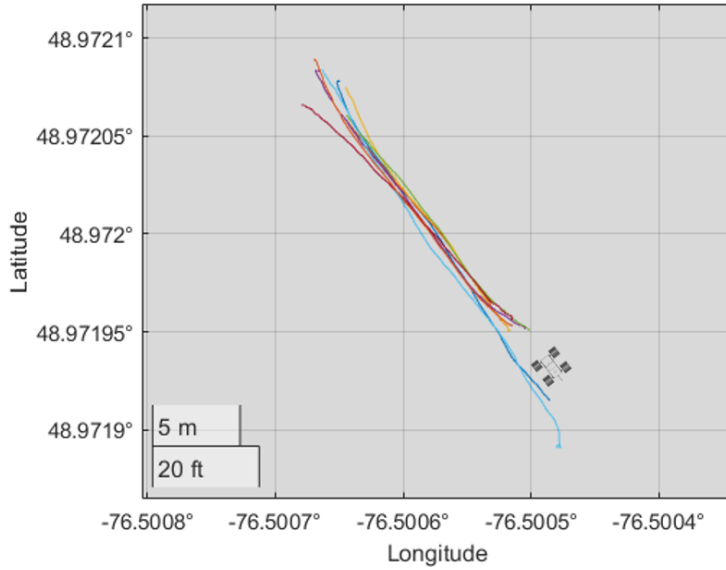


Figure 5.8: Recorded GPS track of the rover making nine passes over the same  $\sim 16$  m stretch of terrain at the wooded test site (#1) in Lebel-sur-Quévillon. An outline drawing of *FrostyBoy* is shown for reference.

the variability at test site #2, with values of  $k$  ranging from 19.2 to 65.0 kPa/m and values of  $z_m$  ranging from 0.29 to 0.54 meters, with a difference of  $\sim 10$  kPa/m just between the left and right sides of *FrostyBoy* after an immobilization event.

The final test suggests that terrain modification, through repeated passes over the same tracks to improve trafficability, is only possible given certain conditions. At test site #1, in the woods with the deep and low stiffness snow, *FrostyBoy* was sent on the same 15-20 meter path nine times. As can be seen from Fig. 5.8, the robot's total lateral variation for these nine passes was only  $\sim 1$  meter, meaning that the wheels were passing over the same terrain, yet the difference in torques and drawbar pull between the first pass and the last pass are statistically indistinguishable (shown in Fig. 5.9). The opposite effect was seen at test site #2, on the lake where the GP data was collected. At this site, the wheels visibly packed down the snow with each repeated pass, and there appeared to be no limit to the mobility of the rover on the modified terrain. In running the rover over its same tracks a second time, there is a clear drop in resistance torque (see Fig. 5.10). In fact, once the rover had compacted a stretch approximately 50 meters long with two to three passes, the

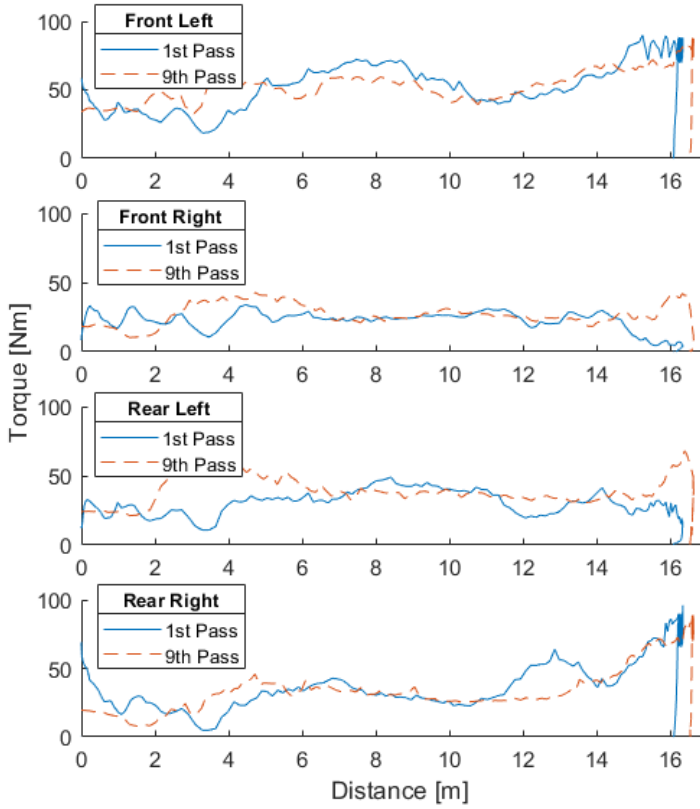


Figure 5.9: Comparison of torques for the first and ninth pass over the same terrain at test site #1. Multiple passes in the same tracks are shown not to significantly reduce the torque required in the loose, unconsolidated, and low stiffness snow with ambient temperatures remaining below 0° C.

sled was attached to the rover and loaded with weights. No effect on the rover's ability to traverse the compressed snow was observed, even when it was towing a payload of 120 kg in the sled.

While the sample size for this study is limited, this phenomenon can be, at least partially, attributed to the ambient temperatures when these measurements were taken. From temperature data collected at the nearest weather station during the time of these experiments, the air temperature at the wooded site (test site #1) reached a maximum of -5.5° C during testing, whereas the ambient air temperature on the lake (test site #2) reached a maximum of 1.2° C and was above 0° C by the time this terrain modification study was performed [66]. Models of wet snow clearly show that its compressibility increases with

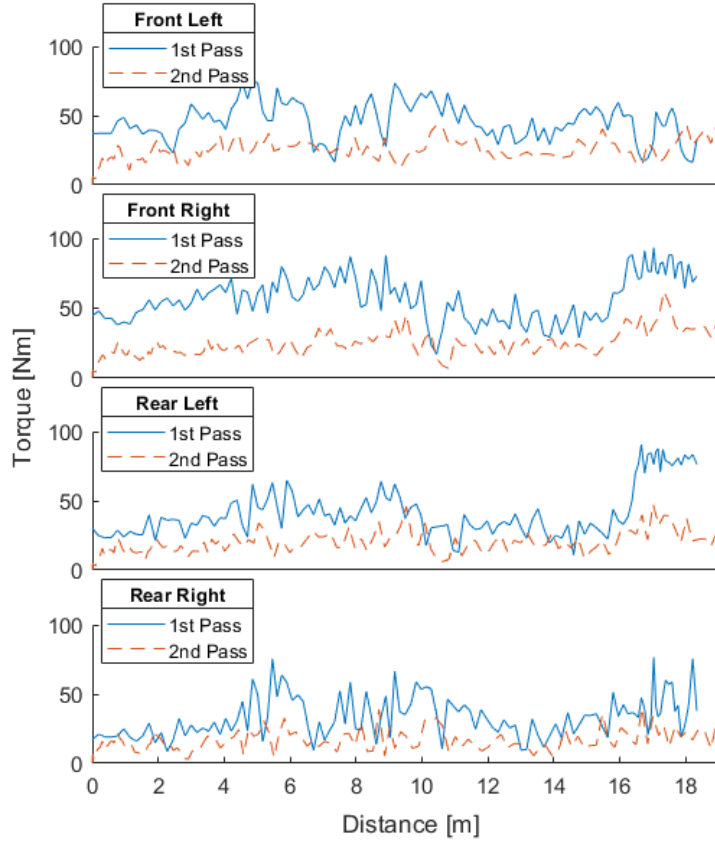


Figure 5.10: Comparison of torques for the first and second pass in the same tracks on the lake (test site #2) after ambient temperatures were approaching 0° C. This shows the clear reduction of resistance torque due to compaction of the terrain from one pass to the next. This trend can even be seen by comparing the front wheel torques to the rear wheel torques of the first pass.

increased water content [67], but since *FrostyBoy* is designed to primarily operate in ambient temperatures below freezing, the modification of terrain through repeated passes is not a viable option for improved trafficability. However, this type of study could be better performed in a controlled environment, like the single-wheel studies described in section 3.3, where low temperatures can be maintained, normal loads and slips can be tightly constrained, and material displacement can be monitored.

## 5.5 Summary

Ultimately the data collection proved successful even though test sites with the necessary conditions and the number of test days were both limited. These sensor data show that understanding the interactions and coupling of all four wheels is critical in identifying how a robot like *FrostyBoy* becomes immobilized in snow. This information is unique in that it could not be gleaned from even the most meticulous single-wheeled study, due to the dynamics and interactions of the four wheels playing a key role in the immobilization sequence. Also, the variation in snow conditions further reinforces how robust an incipient immobilization detection method must be if it is to ensure rover mobility across an ice sheet. One obvious shortcoming in the data set collected is the lack of sinkage measurements. While these data would have been invaluable in modeling the wheel-terrain interaction and the pressure distribution below the wheels, they will, in Ch. 7, be proven unnecessary in detecting incipient immobilization which removes the requirement for these additional sensors. In addition, since any method of measuring sinkage (ultrasonic sensors, laser range finders, video cameras) could be easily occluded with blowing or kicked up snow, these measurements would not be sufficiently reliable to predict mobility. The results also demonstrate that in temperatures below 0° C, there is little evidence to suggest repeated compaction as an effective means of traversing low stiffness, low cohesion snow. However, with climate change increasing global temperatures, wet snow could become common and terrain shaping could prove a useful control sequence in traversing otherwise immobilizing terrain.

The high rate of immobilization events during testing and the inability to modify terrain to obtain the necessary traction might appear discouraging for wheeled robots performing unmanned traverses, but the majority of snow in Greenland and Antarctica is not like that encountered in Lebel-sur-Quévillon. This is evidenced by looking at the years of *Cool Robot's* and *Yeti's* successful campaigns towing sensors in these locations, operating with much higher ground pressure and with less versatile wheels compared to *FrostyBoy*. In-

stead, these data serve as a high concentration of information about a small percentage of snow conditions on a traverse.

# Chapter 6

## Truth Model Development

### 6.1 Introduction

While the collected data, described in Ch. 5, is invaluable in developing an incipient immobilization detection algorithm, it is limited in its scope. Immobilization events were only recorded during two days of testing, with two types of snow, and two sets of environmental conditions. This lack of control over the independent variables influencing the rover's mobility is the nature of *in situ* testing. Also, a key goal of this work is to generate a mobility prediction method without requiring the exhaustive training data sets necessary for machine learning. Therefore, a truth model needed to be developed to complement the data collected from this relatively small sample size of conditions. Once this model, rooted in classical terramechanics models of Bekker, Wong, and Reece, has been adapted to incorporate the dynamics seen in the real-world data, the prediction method can then be tested against simulations of the rover. The truth model then allows for more extensive testing of the method's reliability and for conditions not encountered during testing to be simulated, leading to a more comprehensive incipient immobilization detector.

## 6.2 Modeling Approach

The truth model was developed as a custom MATLAB script to allow for easy customization and adaptability to the effects seen in the real-world data. There are a variety of vehicle dynamics simulation programs available that are useful in the rover hardware design as well as in development of the control algorithms for navigation and course planning. Products like Gazebo and MSC Adams would allow for importation of the rover's geometry from CAD and a digital elevation model (DEM) of rough terrain to better simulate dynamics and weight distribution as the rover drives [68] [69]. In addition, these packages have been formulated to model the multibody physics of wheel suspensions. However, these features are not well suited to the problem. The DEM's of ice sheets show only gradual changes in elevation compared to a more jagged and uneven landscape which would have a larger impact on a rover's mobility. In addition, since *FrostyBoy* was built with low-cost and reliability as primary constraints, there is no wheel suspension and its chassis can therefore be simulated as a single, rigid body. These products also have limited functionality in their terrain models, with Gazebo treating wheel-terrain interaction as a simplified spring-damper system with only point or line contact rather than a complex pressure distribution dependent on sinkage and slip [68]. MSC Adams' simple terrain model was also insufficient for developing the Mars Exploration Rovers (MERs), requiring separate FORTRAN terramechanics subroutines [69]. Since the primary purpose of the modeling effort is to observe how variability in the terrain properties, rather than how terrain topography, impacts mobility and adapt the existing terramechanics models to the data collected, a fully customizable MATLAB script seemed the best-suited approach that would provide the greatest flexibility. Also, while Finite Element Analysis (FEA) models would provide much better accuracy in simulating the wheel-terrain interaction, these are much more computationally and time intensive processes, whereas the MATLAB script rooted in semi-empirical models allows for faster simulations and rapid iteration.

## 6.3 Model Development

### 6.3.1 Dynamics

The truth model is based on rigid-body dynamics with body-fixed equations for a four-wheel drive robot with skid steering in longitudinal motion to mimic *FrostyBoy*. These body-fixed equations of motion are given by

$$\dot{v}_x = \frac{1}{m}(F_{xfl} + F_{xfr} + F_{xrl} + F_{xrr}) \quad (6.1)$$

$$\ddot{\psi} = \frac{1}{I_{zz}} \left\{ \frac{t_w}{2} [(F_{xfr} + F_{xrr}) - (F_{xfl} + F_{xrl})] - M_{res}\dot{\psi} \right\} \quad (6.2)$$

$$\dot{\omega}_{fl} = (T_{fl} - T_{rfl} - B_\omega \omega_{fl}) \frac{1}{I_\omega} \quad (6.3)$$

$$\dot{\omega}_{fr} = (T_{fr} - T_{rfr} - B_\omega \omega_{fr}) \frac{1}{I_\omega} \quad (6.4)$$

$$\dot{\omega}_{rl} = (T_{rl} - T_{rrl} - B_\omega \omega_{rl}) \frac{1}{I_\omega} \quad (6.5)$$

$$\dot{\omega}_{rr} = (T_{rr} - T_{rrr} - B_\omega \omega_{rr}) \frac{1}{I_\omega} \quad (6.6)$$

where the  $F_x$ 's are drawbar pull forces on the four wheels in the longitudinal,  $x$ , direction and the  $T_r$ 's are the resistive torques for all four wheels applied by the terrain. The geometry and properties of the robot are captured in the terms  $m$ , being the robot's mass of 90 kg,  $t_w$ , being the track width of the vehicle (see Fig. 6.1),  $I_{zz}$ , the yaw moment of inertia about its center of mass, and  $I_\omega$ , the wheel moment of inertia about its center of rotation. The lateral forces on the wheels are not captured explicitly, but a restoring moment,  $M_{res}$ , is applied to the robot based on its yaw rate,  $\dot{\psi}$ , to account for the lateral resistance from the terrain on the sidewalls of the wheels. Also, since the rover's yaw is controlled by skid steering rather than by changing the heading of the wheels or axles relative to the body of the robot, the lateral velocity,  $v_y$ , is not included in the model. The  $B_\omega$  term takes into account the mechanical damping in the drivetrain. The values for all these parameters measured from *FrostyBoy* and used in the truth model are outlined in Table 6.1.

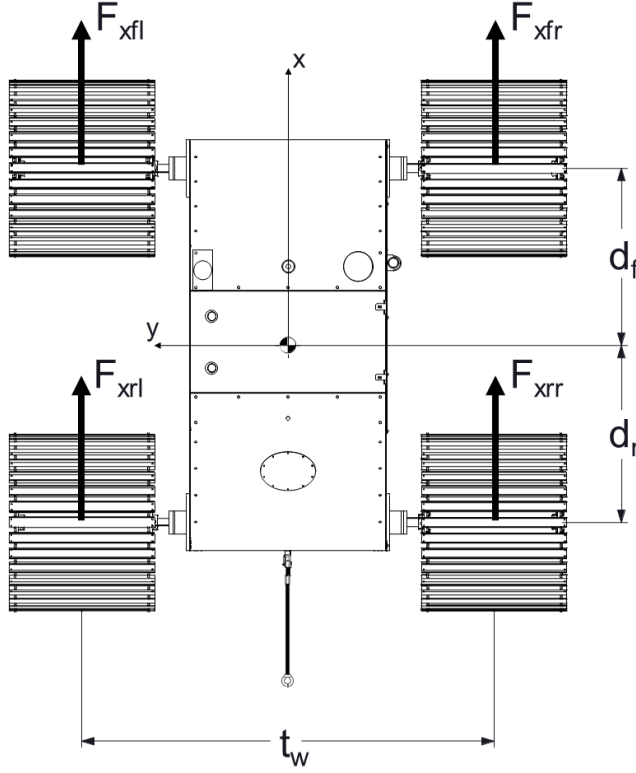


Figure 6.1: Robot body-fixed coordinate conventions and relevant dimensions.

FrostyBoy Parameter Values			
Description	Variable	Value	Units
Mass	$m$	90	kg
Wheel radius	$r_w$	0.265	m
Track width	$t_w$	1.142	m
Distance from COM to front axle	$d_f$	0.579	m
Distance from COM to rear axle	$d_r$	0.515	m
Height of COM above axles	$h$	0.140	m
Rover moment of inertia about z-axis at COM	$I_{zz}$	36.05	$\text{kg m}^2$
Wheel moment of inertia about axis of rotation	$I_\omega$	0.415	$\text{kg m}^2$
Restoring moment constant	$M_{res}$	0.3	$\text{Nm}/(\text{rad/s})$
Mechanical damping constant	$B_\omega$	0.327	$\text{Nm}/(\text{rad/s})$

Table 6.1: Values for parameters measured from *FrostyBoy* and used in the truth model to simulate its behavior.

It is also important to define how the normal load and sinkage are calculated at each time step. Typically, in these simulations, the sinkage for each wheel is iteratively solved, using Eq. (3.11), until the normal load from the terrain balances the robot weight. Even

assuming that the weight of the robot is evenly distributed between all four wheels, if the terrain below each wheel has different properties, the resultant sinkage will be different for each wheel. However, this is not realistic since the rover has a rigid chassis and all four wheels could never be at different relative heights. Instead, this simulation assumes a roll angle,  $\rho$ , to be zero since this observed variable in the test data had a mean of zero and an absolute maximum less than  $1.5^\circ$ . Also, this maximum roll angle would result in less than 1.5 N of weight shift between the left and right wheels on a given axle considering the geometry and weight of *FrostyBoy* at  $0^\circ$  pitch. Therefore, for a given axle, the minimum sinkage among the two wheels is applied to both wheels in the next time step. Pitch angle is calculated using these minimum sinkage values for each axle according to

$$z_f = \min(z_{fl}, z_{fr}) \quad (6.7)$$

$$z_r = \min(z_{rl}, z_{rr}) \quad (6.8)$$

$$\beta = \sin^{-1} \left( \frac{z_f - z_r}{d_f + d_r} \right) \quad (6.9)$$

where the  $z$  values are the calculated sinkages and  $d_f$  and  $d_r$  are the distances from the center of mass to the front and rear axles, respectively. The distribution of weight between the two axles is handled by the following equations, taking pitch and the effect of acceleration and deceleration into account:

$$F_{zf} = \frac{-h(mg \sin \beta + m\dot{v}_x) + d_r mg \cos \beta}{d_f + d_r} \quad (6.10)$$

$$F_{zr} = \frac{h(mg \sin \beta + m\dot{v}_x) + d_f mg \cos \beta}{d_f + d_r} \quad (6.11)$$

The variables and parameters in Eq. (6.10) and (6.11) are defined in Fig. 6.1 and 6.2. Then, for each axle, the weight supported by the wheel with the adjusted sinkage is calculated based on the minimum sinkage, with the opposite wheel on the same axle assumed to support the remaining weight of that axle. For example, assume that  $z_{fl} > z_{fr}$  in the previous

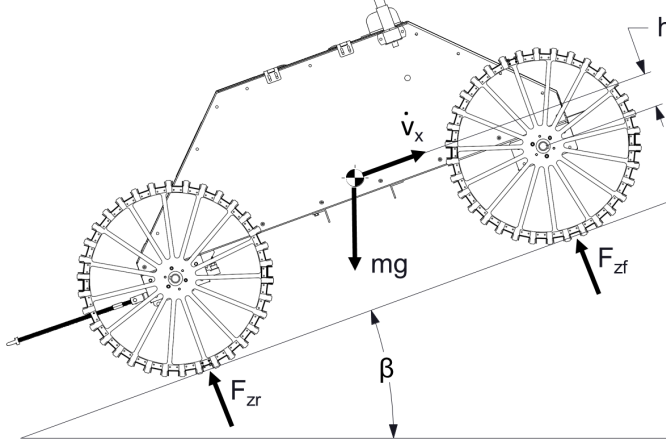


Figure 6.2: Diagram showing conventions and variables involved in calculating the normal force for front and rear axles.

time step. This means that the normal force from the terrain,  $F_{zfl}$ , for the current time step will be calculated using the given minimum sinkage,  $z_f$ , which is equal to  $z_{fr}$ . Then, the normal force supporting the right, front wheel,  $F_{zfr}$ , will be calculated from

$$F_{zfr} = F_{zf} - F_{zfl} \quad (6.12)$$

with the sinkage,  $z_{fr}$ , being iteratively calculated according to the balance of forces equation (3.11). These calculations are critical in defining the wheel-terrain interaction as they serve as the basis for the reaction forces from the terrain.

### 6.3.2 Motor Model

The RoboteQ motor controllers can operate in open-loop or closed-loop mode. In open-loop mode, a constant voltage is sent to the four motors corresponding to a desired wheel speed. In this mode, the wheel speed varies as the load on the wheel changes. The load on the wheel is determined by the resistance torque from the terrain. Therefore, as the terrain changes beneath each wheel, the wheel speed also changes.

The relationship between torque and wheel speed is characterized by the motor manufacturer in the torque-speed curve shown for the Electrocraft RP34 series motor in Fig. 6.3,

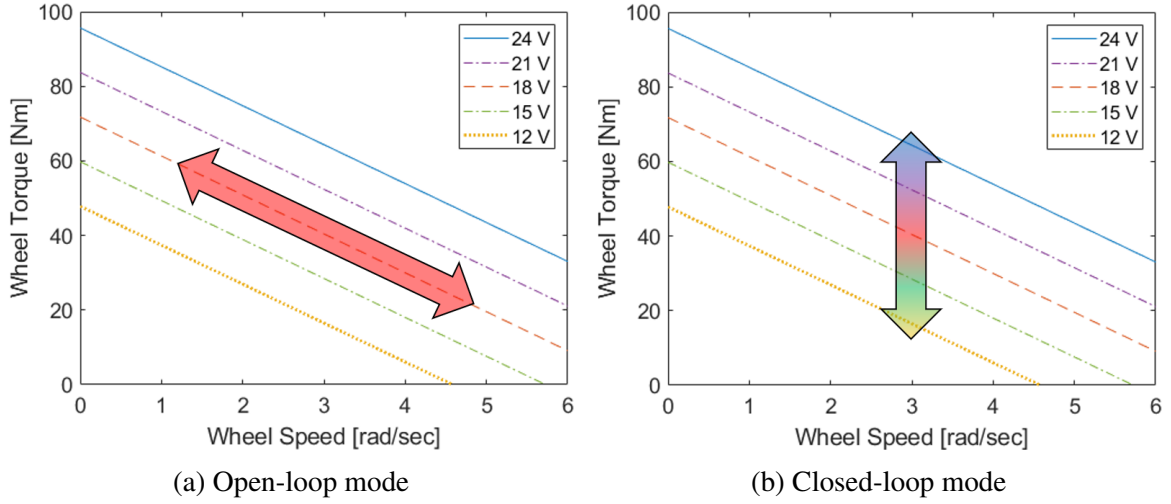
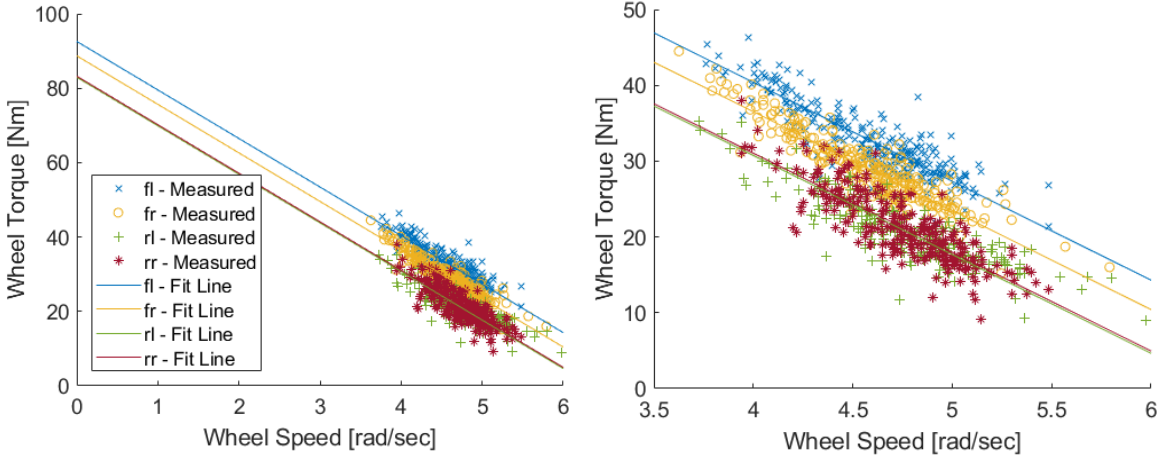


Figure 6.3: These plots show how the motor operating points move in open-loop and closed-loop modes. **(a)** In open-loop mode, the applied voltage is fixed and the motor operating point moves along the torque-speed curve defined by this voltage. This figure shows an example if the applied voltage is set to 18V (38% of the 48V design voltage) and the load on the wheel varies. The torque-speed curves at 12V, 15V, 21V, and 24V are shown for reference. **(b)** In closed-loop mode, the motor controller changes the applied voltage (represented by the color gradient in the arrow) to maintain a constant speed over a wide range of loads. In this figure, a speed setpoint of  $\sim 3$  rad/sec is being maintained.

where the motor speeds have been translated to wheel speeds given the 40:1 gearbox. Figure 6.3a shows that in open-loop mode, the operating point of the motor is constrained to vary only along the torque-speed line defined by the applied voltage. On the other hand, in closed-loop mode a speed setpoint, rather than an applied voltage, is defined. The measured rotational speed of the motor is fed back to the controller and compared to the setpoint, and then the voltage applied to the motor from the motor controller is altered to maintain a constant speed even with varying load. The torque-speed curves at various applied voltages are shown in Fig. 6.3b to demonstrate how changing the applied voltage frees the motor from just operating on a single torque-speed curve and instead allows for a constant speed to be maintained over a wide range of loads.

While *FrostyBoy* was intended to be operated under closed-loop speed control, a unique



(a) Data from steady-state operation of motors with best fit torque-speed curves.

(b) Zoomed in version of (a). The legend from (a) still applies.

Figure 6.4: Comparison of the calculated torque-speed slope with measured data points during steady-state operation of *FrostyBoy*. This data is pulled from a run where the rover was driving on the lake (test site #2), tracking relatively straight, with all four motors sent the same commanded voltage of 18V.

quirk of the RoboteQ motor controllers<sup>2</sup> and the limited time for testing required that the motors be operated in open-loop mode. This simplified the model of the motors, as there was no need to replicate the motor controller's unknown closed-loop feedback parameters. Instead, the torques applied to the terrain by the wheels ( $T_{fl}$ ,  $T_{fr}$ ,  $T_{rl}$ , and  $T_{rr}$ ) could be modeled based on the torque-speed curve at the commanded voltage. This slope was compared to the measured torques and speeds of *FrostyBoy*'s wheels on the lake (test site #2), during the longest sustained steady-state operation of the rover in snow at either test site. As shown in Fig. 6.4, the measured data match well with the precalculated slope from the motor manufacturer's datasheet, with the residuals following a normal distribution with an average standard deviation of 2.26 Nm. As described in section 5.3, the speed setpoint corresponds to an applied open-loop voltage commanded as a percentage of the motor's 48V rating and is the same for all four motors. For the data presented in Fig. 6.4, all four

<sup>2</sup>The Arduino microcontroller on *FrostyBoy* sent speed commands in the form of pulse width modulated (PWM) digital output signals. However, in order for the RoboteQ motor controller to operate in closed-loop mode, the speed commands must be communicated via serial commands. By the time this fact was discovered, the rewiring and reprogramming necessary could not be accomplished before testing.

motors were commanded to 37.5% of full voltage (corresponding to a no-load wheel speed of 11.5 rad/sec), but the best fit lines show setpoints ranging from 34.7% to 38.7%. This error will not be reproduced in the model, but is presented here to show one source of the model's inaccuracy in replicating real data. These data were pulled from a segment where the robot was tracking straight, with an average yaw rate of 0.2 deg/s. Therefore, the slight offset in torques between the front wheels and the resultant turning moment on the robot body is not enough to overcome the lateral resistance force on the wheel sidewalls. This figure also shows that the rear wheel torques are lower than those of the front wheels. Because the rover is weight balanced front to back, this difference in torques is assumed to be due to the front wheels compacting the terrain, resulting in less resistance torque applied to the rear wheels by the terrain. This trend was not observed in data collected during the colder day at test site #1 and will therefore not be included in the model, as the simulations assume low temperatures and no significant modification of the terrain due to multiple passes. Ultimately, the torque-speed operating points, measured during steady state, match the expected behavior of motors operating in open-loop mode. Outside of steady state, when the terrain becomes more variable, the measured torque-speed relationship still holds, but the four wheels' operating points become separated. Some wheels experience increased terrain resistance, forcing the wheel speed to decrease with an increase in torque on the wheel, while other wheels slip in unconsolidated snow, increasing in wheel speed as they experience less resistance torque. This separation of operating points is further investigated in section 6.4, but it does not change the validity of the motor model.

### 6.3.3 Terrain Model

The terrain resistance torques and forces used in the model are calculated from the Bekker-Wong terramechanics model described in Ch. 3. While the drawbacks and limitations of these empirical equations in simulating a lightweight vehicle in snow are discussed in previous chapters, it serves as a widely accepted, standard foundation for an investigation of

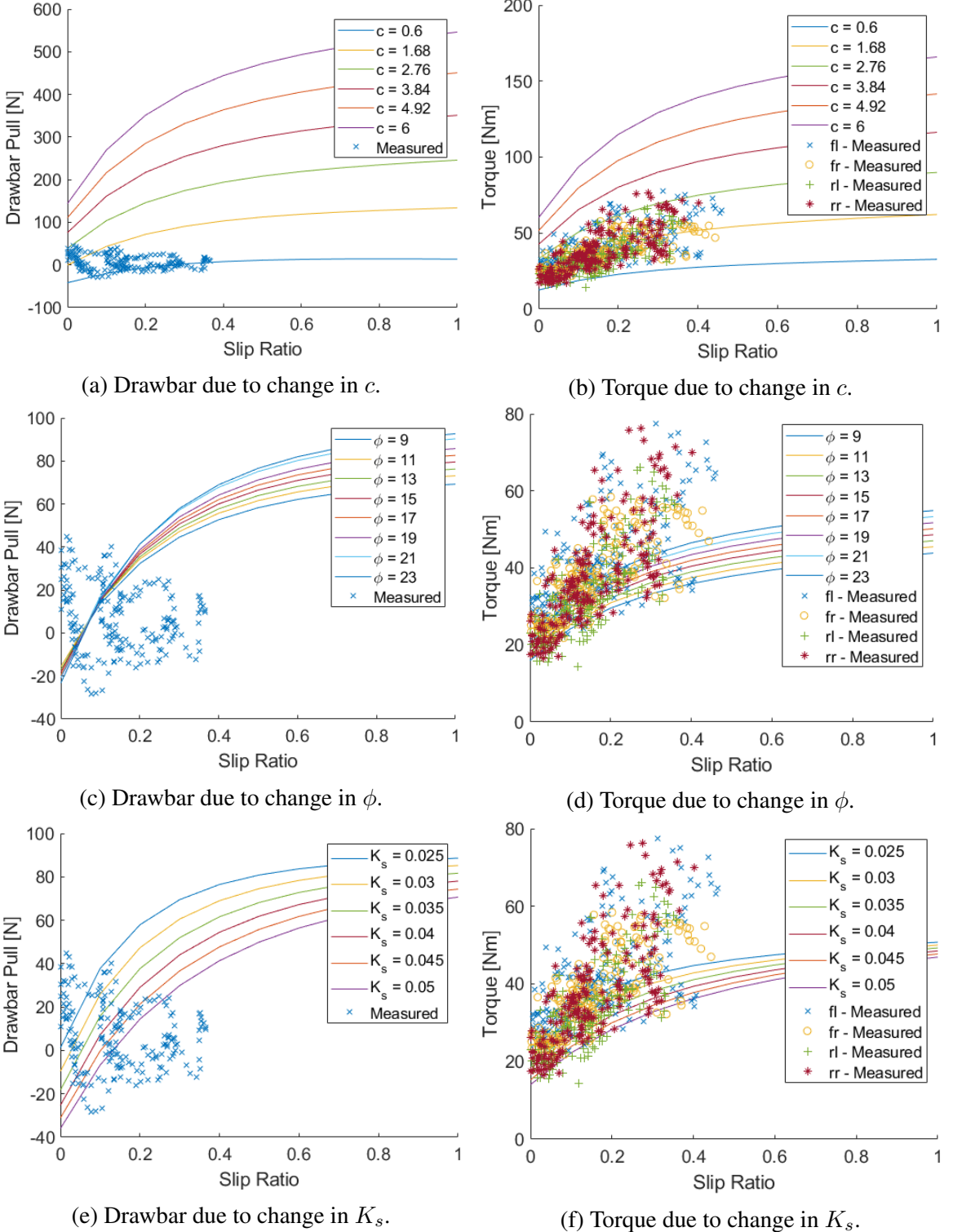


Figure 6.5: Sensitivity study to understand the effects of cohesion,  $c$ , angle of internal friction,  $\phi$ , and shear deformation modulus,  $K_s$ , on drawbar pull and torque for a single wheel. The data points, repeated on each plot, are from measurements taken during steady-state operation of *FrostyBoy* on the lake (test site #2). Note that plots (a) and (b) have differently scaled y-axes than the other plots due to the significant impact of the cohesion parameter on drawbar pull and torque.

mobility. However, a few modifications are incorporated from the start. First of all, the pressure-sinkage distributions at the wheel-terrain interface are defined by the Preston-Thomas equation (3.6), rather than the Bekker equation (3.2). This model matches well with plate indentation test data that Lever collected in Greenland as well as that measured with the GP in Lebel-sur-Quévillon (see section 5.4). Since only two parameters define the curve, it also reduces the number of variables that define the terrain, and it is easier to understand the physical effect each of these parameters has on the compressibility of the snowpack. In terms of traction, the poorly bonded model (3.9) will be used since this is the most accurate descriptor of what was encountered during testing in Lebel-sur-Quévillon, as it was dry, low cohesion snow with no sintering observed when grains in the top 10 cm of the snowpack were inspected. In addition, it allows for the tuning of the single shear deformation modulus,  $K_s$ , rather than the two parameters involved with the well bonded traction model (3.8). Unlike the majority of terramechanics models [70], this simulation will also include the bulldozing effect described by Eq. (3.14) since this effect makes up a significant portion of the terrain resistance for such a wide wheel [43]. While this adds three more parameters to the already extensive terrain parameter set ( $\gamma$ ,  $K_c$ , and  $K_\gamma$ ), these will remain constant for all simulations. Similar to the analysis performed in section 3.7, the parameters defining the angle of maximum stress,  $c_1$  and  $c_2$ , as well as the definition of the exit angle,  $\theta_2$ , will be held constant.

The data collected from Lebel-sur-Quévillon were used to approximate the remaining terrain parameters. The method by which this was accomplished was in no way exhaustive, nor meant to produce the exact values of the terrain. This step is to merely ensure that the model matches the scale and overall trends of the data. As presented in Ch. 5, the parameters defining the pressure-sinkage curve were directly measured using the GP, with  $k$  ranging from  $\sim 20$  to 65 kPa/m and  $z_m$  ranging from 0.3 to 0.54 meters. Given this measured variability in the terrain, the parameters of cohesion, angle of internal friction,

and shear deformation modulus were tuned to match the average drawbar pull<sup>3</sup> per wheel vs. slip and the resistance torque<sup>4</sup> per wheel vs. slip. Lines of drawbar pull vs. slip and torque vs. slip were generated using the terrain model equations for a single wheel while varying these parameters over the expected range (discussed in section 3.4). Figure 6.5 shows these simulated drawbar pulls and torques compared to measurements taken during steady-state operation of the rover in Lebel-sur-Quévillon. All six figures present the same set of measured data. Figures 6.5a and 6.5b show that minor changes in the cohesion parameter have a significant impact on both drawbar pull and resistance torque, requiring a different y-axis scale than the rest of the figures. From this sensitivity study it was determined that the cohesion parameter in the simulation was to be limited to the lower end of the range defined in the literature in order to simulate immobilizations and match the measured torque. Figures 6.5c through 6.5f show the relatively limited effect both the angle of internal friction and shear deformation modulus have on drawbar pull and torque. Therefore, these can be treated as static parameters, with the full range of observed mobility conditions being captured by the measured variability in the pressure-sinkage stiffness parameter,  $k$ , and with slight changes in cohesion,  $c$ . The most notable result from this sensitivity study is that the shape of the simulated curves still do not match the general trend of the measurements, even after attempting to fit the data by modifying the terrain parameter values. The simulated curves of drawbar pull continue to increase with increased levels of slip, whereas the drawbar pull data show that the maximum measured values drop off with increased slip ratios. The opposite is shown in the torque plots, with simulated torque increasing slowly as slip increases, whereas the measured torque shows a steep rise in torque with higher slip ratios, up to 50%. To increase the slope of resistance torque vs. slip, while also reducing drawbar pull at higher slips, the effect of slip-sinkage was added to the model

---

<sup>3</sup>Drawbar pull was calculated by using the moving average of the robot's acceleration in the x-direction as reported by the IMU. The force needed to accelerate the rover at this rate was then divided equally between the four wheels to give an average drawbar pull per wheel.

<sup>4</sup>Resistance torque was assumed to match torque applied by the wheel to the terrain. Each wheel's torque was calculated from the measured current being supplied to the wheel's motor multiplied by the motor manufacturer's torque constant and the assumed 80% efficiency of the gearbox, described in section 5.4.

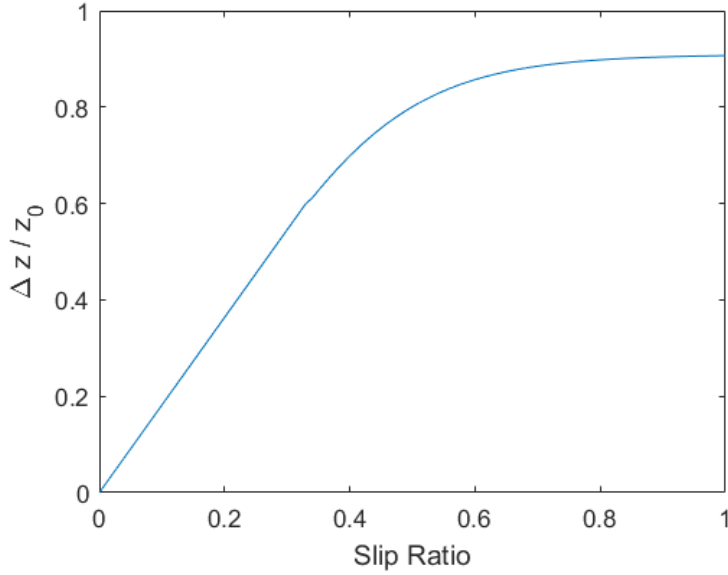


Figure 6.6: Modified slip-sinkage factor.

using a modified version of Eq. (3.15). Since this equation was only verified for slips up to 33% [45], it was modified when incorporated into the truth model to limit the additional sinkage at elevated slip ratios, where the added sinkage from slipping,  $\Delta z$ , can be defined by

$$\Delta z = \begin{cases} iSz_0, & i \leq 0.33 \\ \frac{1}{2} \left[ \frac{S}{1+exp[-8(i-0.25)]} \right] z_0, & i > 0.33 \end{cases} \quad (6.13)$$

This limits the additional slip-sinkage to be only  $\sim 90\%$  of  $z_0$  at 100% slip, rather than  $\sim 180\%$ , as described by Eq. (3.15).

This modified slip-sinkage model, shown graphically in Fig. 6.6, resulted in a much improved approximation of the real data. Figures 6.7a and 6.7b show that with an average cohesion value of 1.2 kPa, the drawbar pull only becomes positive at higher values of  $k$  for a narrow band of slip ratios below 50%. At the lower values of  $k$ , the sinkage becomes so great that the tractive force the wheel can apply to the terrain before it fails is not enough to overcome the terrain resistance force. At high values of slip, the slip-sinkage becomes so much that even with a relatively high stiffness,  $k$ , the drawbar pull still drops below

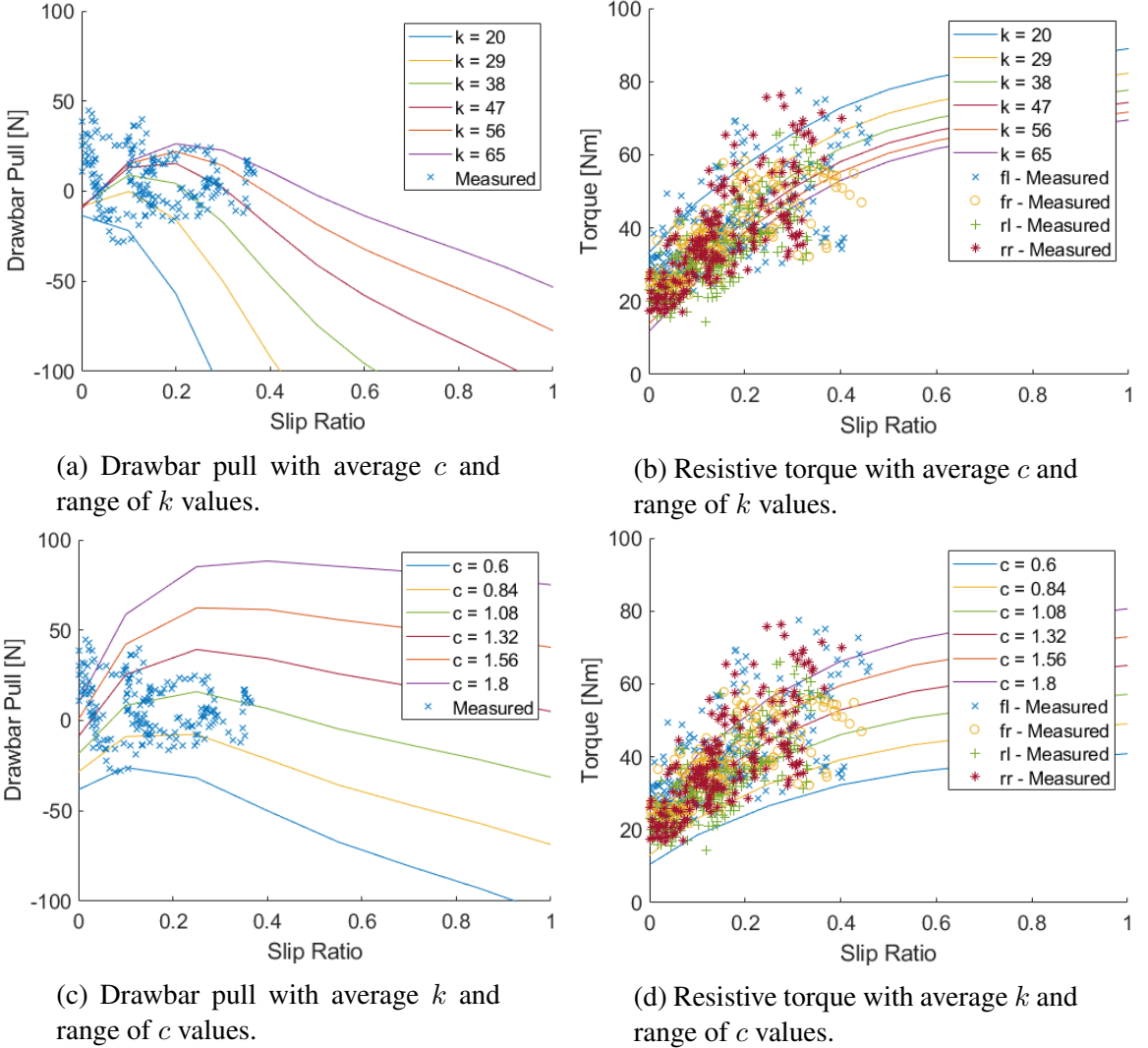


Figure 6.7: Curves generated using final set of terrain parameters that roughly approximate measured data.

Terrain parameters for simulation									
Parameter [Units]	$k$ [ $\frac{\text{kPa}}{\text{m}}$ ]	$z_m$ [cm]	$c$ [kPa]	$\phi$ [°]	$K_s$ [cm]	$c_1$ -	$c_2$ -	$\theta_2$ [°]	$S$ -
Simulation	20 - 65	54	0.6 - 1.8	9	.03	0.18	0.32	-12	1.82

Table 6.2: Final terrain parameters used to simulate low stiffness, poorly bonded, low cohesion snow.

zero. Figures 6.7c and 6.7d show that stepping up the cohesion parameter steps up both the drawbar pull and torque, with its effects more significant at higher slip ratios. Ultimately, Fig. 6.7 shows that the variability of the snow observed in Lebel-sur-Quévillon and the

resultant behavior of *FrostyBoy* can be adequately estimated by varying  $k$  and  $c$ . Therefore, the parameters, outlined in Table 6.2, will be used in simulating *FrostyBoy* operating on low stiffness, poorly bonded, low cohesion snow.

### 6.3.4 Simulation Process

With the dynamics, motor model, and terramechanics model equations all defined, the steps involved in the simulation process are:

1. The normal force for each wheel is calculated based on the rover's pitch and instantaneous longitudinal acceleration (6.10) (6.11).
2. The sinkage of each wheel is iterated until the pressure distribution below the wheel balances the normal load calculated in step 1. The additional sinkage due to slip (6.13) is then added to this nominal sinkage value to determine the ultimate sinkage each wheel would reach if these conditions were to be maintained at steady state. However, the actual change in sinkage for each time step is limited to that permitted by acceleration due to gravity. The minimum of the front wheel sinkages and the minimum of the rear wheel sinkages determine the pitch angle of the robot for the next time step.
3. The pressure distribution based on the sinkage determined in step 2 and the slip determined from the previous time step, give the shear stress distribution, terrain resistance, resistance torque, and therefore the overall drawbar pull for each wheel.
4. The torques applied to the terrain by the wheels are calculated by using the motor model discussed in section 6.3.2, where the wheel speeds, the known open-loop voltage setpoint, and the torque-speed curve of the motors define the operating point of the motor. Zero-mean Gaussian noise with a standard deviation of 2.26 Nm is added to this calculated torque to account for the variation around the torque-speed curve seen in Fig. 6.4.

- These applied torques and resistance forces serve as inputs to the dynamics equations (6.1) - (6.6), which define the robot velocity, yaw rate, wheel speeds, and therefore slip (5.3), for the next time step.

## 6.4 Simulating Immobilizations

The work in tuning the motor model and determining the most likely range of terrain parameters by looking at torque and drawbar pull data serve as validation for the performance of each wheel. This could be more rigorously studied using a single-wheel testbed filled with a homogeneous snow with tightly controlled terrain parameters. However, the value of the data obtained during testing is that they were collected *in situ*, with a four-wheeled robot becoming immobilized on a natural snowpack. This means that validation of the model dynamics of the robot as a whole must be performed by trying to replicate the four-wheeled immobilization signature, rather than just the individual wheels operating at steady state. As discussed in Ch. 5, the immobilizations were characterized by two of the wheels, at a diagonal to one another, experiencing a rapid increase in resistance torque until they reach the motor controller current limit, and the other two wheels increasing in rotational speed with a rapid decline of resistance torque until they are almost at a no-load condition. Comparing the torque-slip data points during an immobilization with those of steady-state conditions, Fig. 6.8 shows the separation in operating points that occurs and the divergence from the defined torque-slip curves given the range of terrain parameters determined. Various methods to tune the model to match these data were attempted.

The first method to account for the drastic change in torques was to look at each wheel individually and assess if there is a set of terrain parameters that could result in this movement of operating points while keeping all other variables constant. For the wheels that reach their torque limit, a patch of higher cohesion snow could result in this rapid increase in torque (as shown in Fig. 6.5b), however it would also result in higher drawbar pull rather

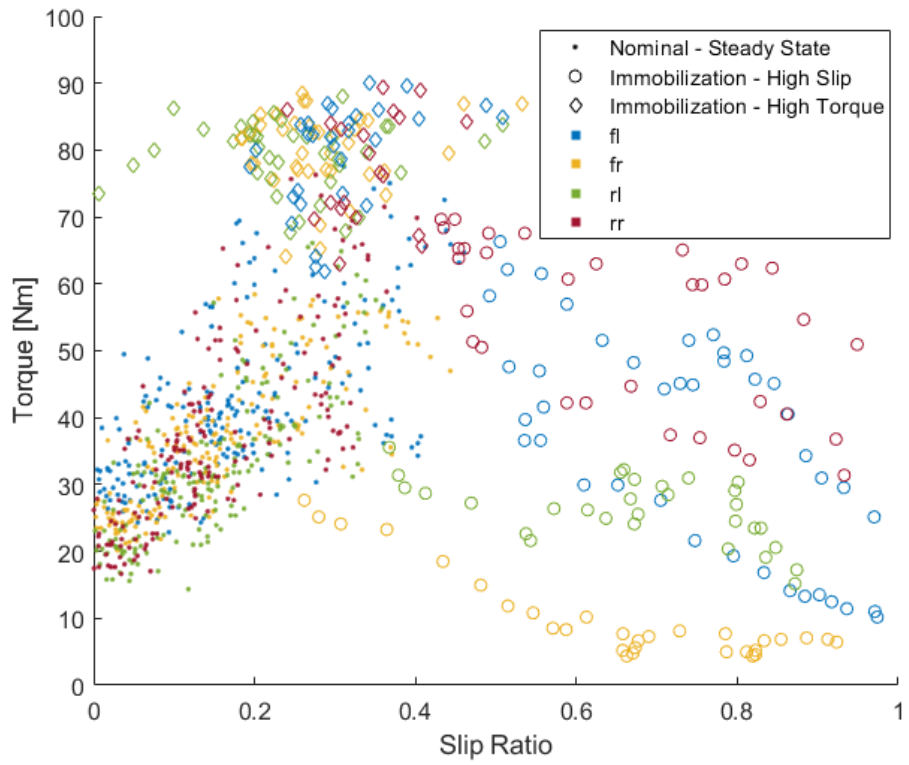


Figure 6.8: Separation of high torque and high slip operating points during immobilizations from those during nominal steady-state mobility. The dots represent nominal mobility, the circles show divergence from nominal mobility in the direction of high slip and lower torque, and the diamonds demonstrate divergence from nominal mobility in the direction of low slip and higher torque. The colors are used to denote from which of the four wheels the data point was measured.

than a strong terrain resistance force that slows the robot velocity to zero. Another option is that the pressure-sinkage slope,  $k$ , could drop to a point where the increased sinkage of the wheel could cause the increase in resistance torque and the corresponding increase in terrain resistance. The first problem with this theory is that the  $k$  value would need to be significantly lower than any value measured using the GP on the lake. The second problem is that the sinkage necessary for the modeled resistance torque and terrain resistance force to be as high as observed was never seen. While continual sinkage measurements were not recorded by the ultrasonic sensors, sinkage after an immobilization event can be determined from comparing photos of wheels in the snow with the known wheel geometry.

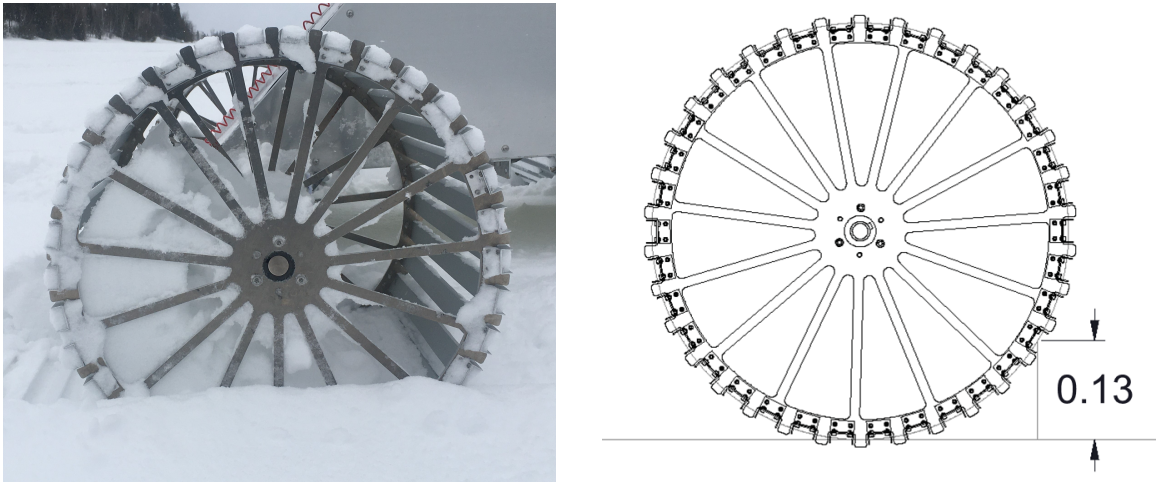


Figure 6.9: A typical example of a wheel's sinkage after an immobilization event.

Figure 6.9 shows a typical wheel sinkage of approximately 13 cm, which is well below the modeled sinkage that would result from stiffness values below 20 kPa. For the wheels that approach a no-load condition of higher speeds and decreased resistance torque, a decrease in cohesion would have the observed effect of simultaneously reducing torque and drawbar pull. However, at such sustained high slip, the wheel would succumb to dynamic slip-sinkage and result in much higher sinkage than observed. And finally, no value of  $k$  could reproduce this reduction of torque and increase in terrain resistance.

This analysis clearly shows that the wheels cannot be examined individually, and there is an interaction between the four wheels that is causing these changes to occur. Of the variables measured, there were no anomalies that could explain the immobilization phenomenon. While the front axle of the robot did consistently pitch up relative to the back axle of the robot preceding an immobilization (decrease in  $\beta$ ), this weight transfer from the front to the back and the added gravitational resistance force do not explain why wheels at a diagonal to one another and on opposite axles would exhibit the same behavior. However, in experimenting with weight transfer, it was found that transferring the weight of the robot from four wheels to two wheels resulted in the observed effect of high torque and low slip for the weighted wheels and low torque and high slip for the unweighted wheels, with a

universal decrease in drawbar pull. This match in wheel behavior resulted in the hypothesis that natural variation in the terrain parameters was inciting a transfer of weight from all four wheels, almost entirely to only two-wheels, ultimately resulting in an immobilization. These two wheels, supporting the majority of the weight, must be at a diagonal to one another, as observed in the data, since this is the only stable configuration in which this can happen. The truth model was then used to investigate how irregularity in the terrain properties could incite this behavior.

The first study performed was to force an immediate change in the  $k$  value of the terrain below the front left and rear right wheels, forcing these wheels to sink less than the other two wheels, and thus transferring the weight due to the minimum sinkage calculations described in section 6.3.1. As can be seen in Fig. 6.10, while this incited a transfer of weight, this did not increase torque for the front left and rear right wheels, nor did it drastically increase slip for the front right and rear left wheels. In fact, with the lower sinkage, the resistive torque actually decreased, the rover velocity increased, and there was only a  $\sim 75$  N difference in normal force between the wheels on each axle.

The next study performed was to force an immediate decrease in cohesion for the front right and rear left wheels. These results can be seen in Fig. 6.11. The transfer of weight is less substantial with this drop in cohesion, but there is a more substantial increase in torque on the front left and rear right wheels, as well as a desired increase in slip for the front right and rear left wheels. However, neither of these expected variations in terrain parameters forced an immobilization. Instead, the robot in the model merely reached a new steady-state operating point, with the torques and slips never reaching the magnitude observed in the collected data, and thus failed to capture relevant positive-feedback dynamics or phenomena.

One effect that was not captured in these tests, but was observed during the experiments in Lebel-sur-Quévillon, is the excavation of the snow that occurs at high slips. While slip-sinkage was taken into account in these simulations, it was only considered for the case of

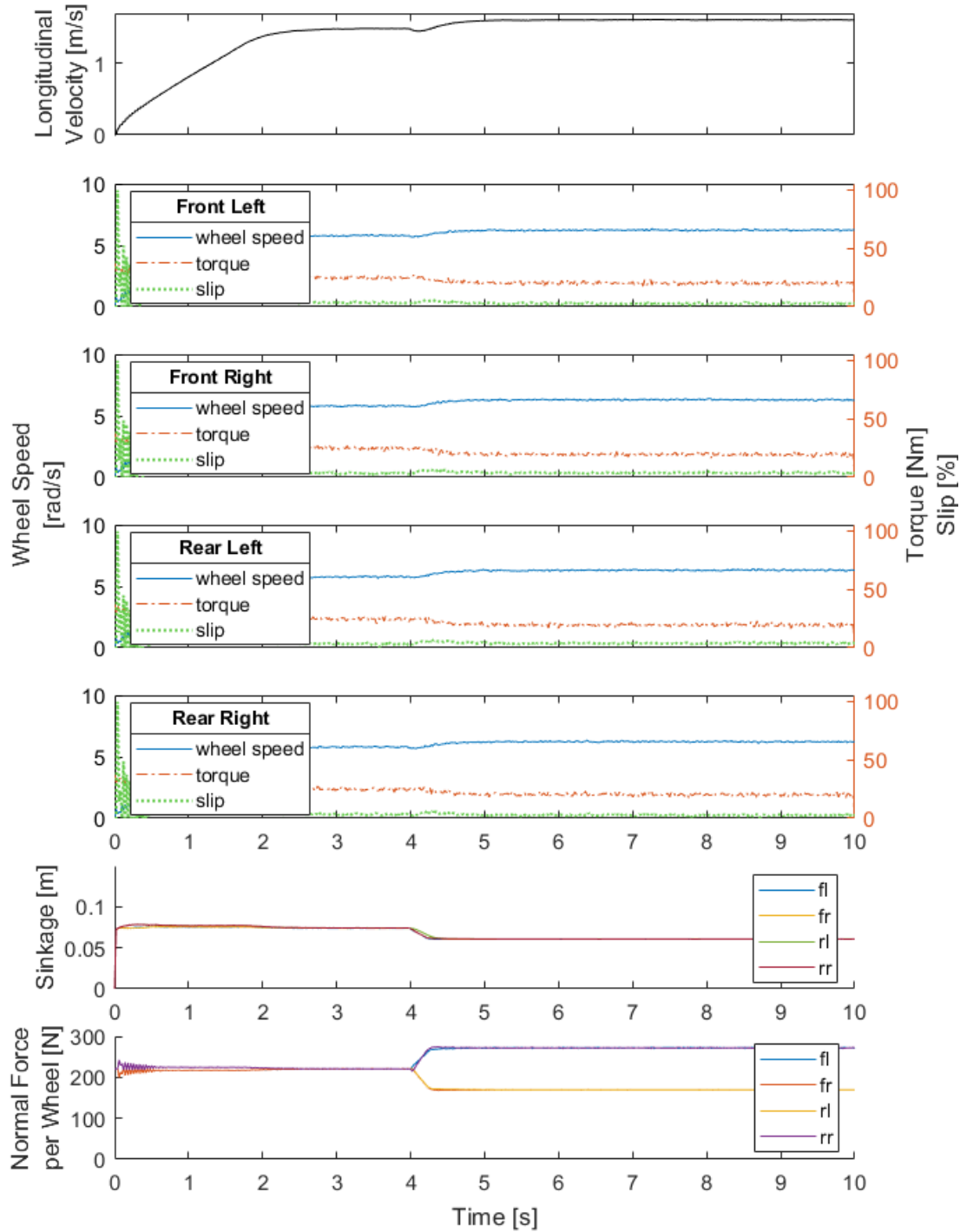


Figure 6.10: Simulation of abrupt increase in  $k$  at  $t = 4$  seconds for the front left and rear right wheels.

increased sinkage due to slip. However, with a rigid chassis robot, the high slip wheels are restricted to the sinkage reached by the opposite wheel on the same axle. Therefore, this in-

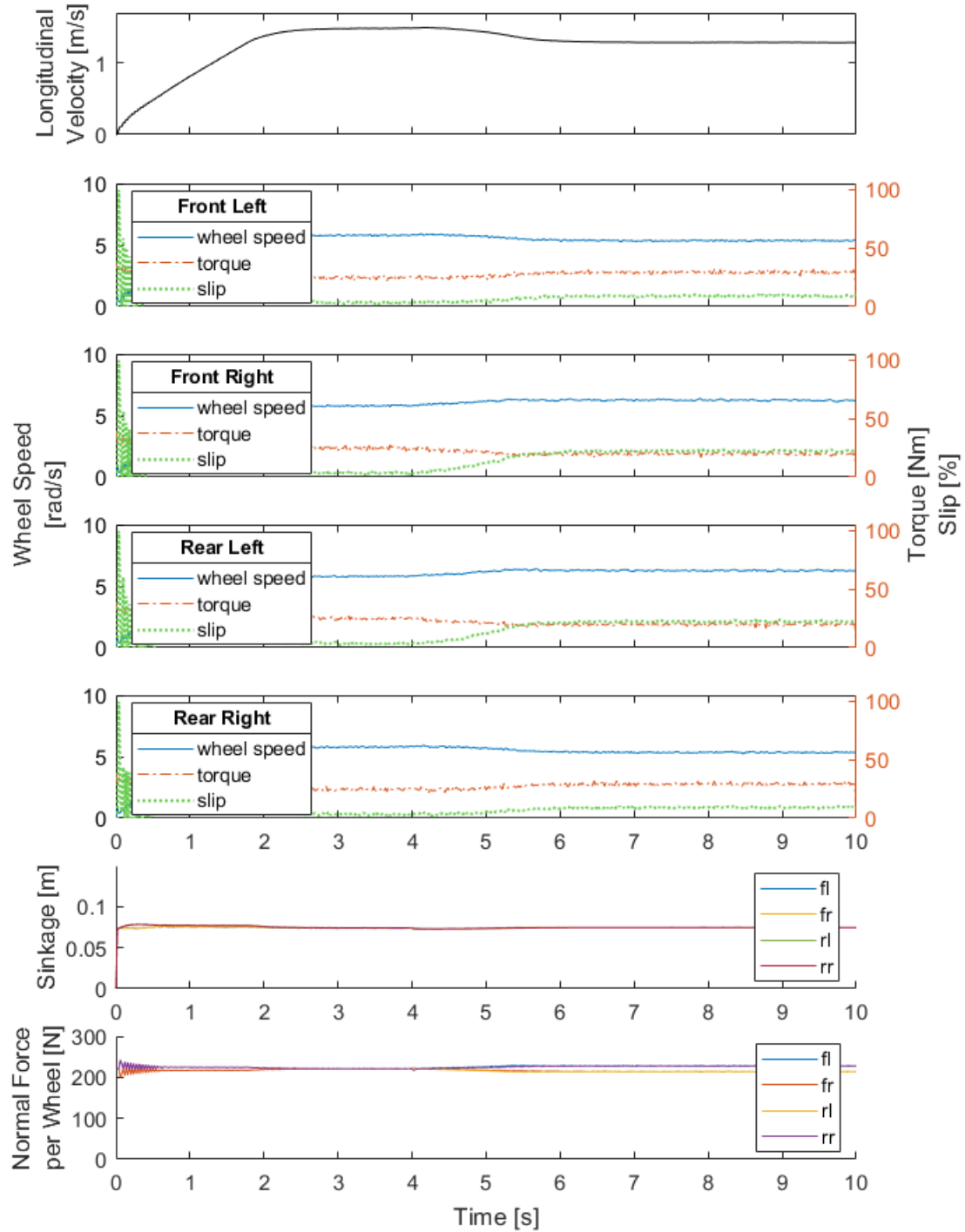


Figure 6.11: Simulation of abrupt decrease in  $c$  at  $t = 4$  seconds for the front right and rear left wheels.

crease in slip and resultant excavation, which would normally cause additional sinkage, had no effect on the wheel in the model. To remedy this, the model was changed to incorporate

what was termed an *excavation sinkage* for the wheels that cannot reach their calculated depth due to the rigid chassis. The excavation sinkage is a pseudo-sinkage calculated by subtracting the  $\Delta z$  term from  $z_0$  rather than adding it, and it is then used to calculate the resistance forces applied to the wheel by the terrain. This has the observed effect of a positive feedback loop between increased slip and weight transfer, as the slipping wheel excavates the terrain that would have supported it. The second parameter added to the model, was a wheel sinkage ratio,  $\lambda$ , that is used to calculate the exit angle at the rear of the wheel based on the sinkage at the front of the wheel, instead of keeping this angle constant [40].

$$\theta_2 = \cos^{-1} \left( 1 - \lambda \frac{z}{r_w} \right) \quad (6.14)$$

When used with the excavation sinkage as the  $z$  in the above equation,  $\theta_2$  goes to zero as  $z$  goes to zero. The wheel sinkage ratio,  $\lambda$ , was then tuned to ensure that the steady-state torques still matched those shown in Fig. 6.7, given the previously defined range of terrain parameters. The exact value of this wheel sinkage ratio in various types of snow needs further study, but for these simulations, a  $\lambda$  value of 0.07 was chosen to give the previously estimated  $\theta_2$  value of  $-15^\circ$  at a sinkage of approximately 13 cm (from Fig. 6.9).

With these phenomenological effects in place, the rover behavior in the model began agreeing with the unique immobilization mode seen in the test data. In addition, the model did not require that the natural, random terrain variation be such that the terrain below two wheels at a diagonal have higher  $k$  values and the other two wheels simultaneously encounter low cohesion terrain in order to incite a loss of traction. Instead, in the updated model, relatively small variations in the stiffness of the terrain alone can instigate the immobilization behavior. This is shown in Fig. 6.12, in which the only parameter modified is the  $k$  value, increased from 40 kPa/m to 65 kPa/m for the front left wheel and the rear right wheel, after the simulated rover has reached steady state at  $t = 4$  seconds. This causes the weight to quickly start shifting to the front left and rear right wheels, as the other two

wheels are lifted above their natural sinkage, causing an increase in slip and a start to the erosion of the supportive terrain below. As the weight is transferred, the resistance torque on the front left and rear right wheels increase quickly, slowing their wheel speeds, resulting in a significant reduction in their drawbar pull. This combination of effects eventually results in the complete loss of forward velocity of the rover, with the front left and rear right wheels stalled and the front right and rear left wheels spinning freely.

Without normal force sensors on all four wheels, this provides evidence that a weight shift, due to a rigid chassis, is a large factor in *FrostyBoy* becoming immobilized. To assess the impact of adding compliance about the roll axis for each axle, the simulation was run with all four wheels sinking to the depth where the normal force balances the weight on that wheel, plus the extra depth from dynamic slip-sinkage. These simulations do not consider the variation in pressure across the width of each wheel that would result from the roll angle of each axle. This is assumed to be negligible and therefore, the camber angle is set to 0° for all wheels. To incite immobilization, the variability of snowy terrain is modeled by generating random walk models of the stiffness parameter,  $k$ , and the cohesion parameter,  $c$ , varying along the x-axis in discrete steps according to:

$$k_q = k_{q-1} + n_k \Delta x \quad (6.15)$$

$$c_q = c_{q-1} + n_c \Delta x \quad (6.16)$$

where the noise parameters,  $n_k$  and  $n_c$ , follow a zero-mean Gaussian distribution with standard deviations of 50 kPa/m<sup>2</sup> and 1 kPa/m, respectively. The random walks of  $k_q$  and  $c_q$  are generated before the simulations are run, with each increment of  $q$  corresponding to a  $\Delta x$  of 0.01 m. The parameters remain constant at nominal values for the first 4 seconds of the simulation time, so the rover can reach a steady-state velocity. Then, the terrain parameters beneath the wheels are set to those precalculated based on the longitudinal distance traveled since t = 4 seconds. Therefore, both wheels on the same axle experience

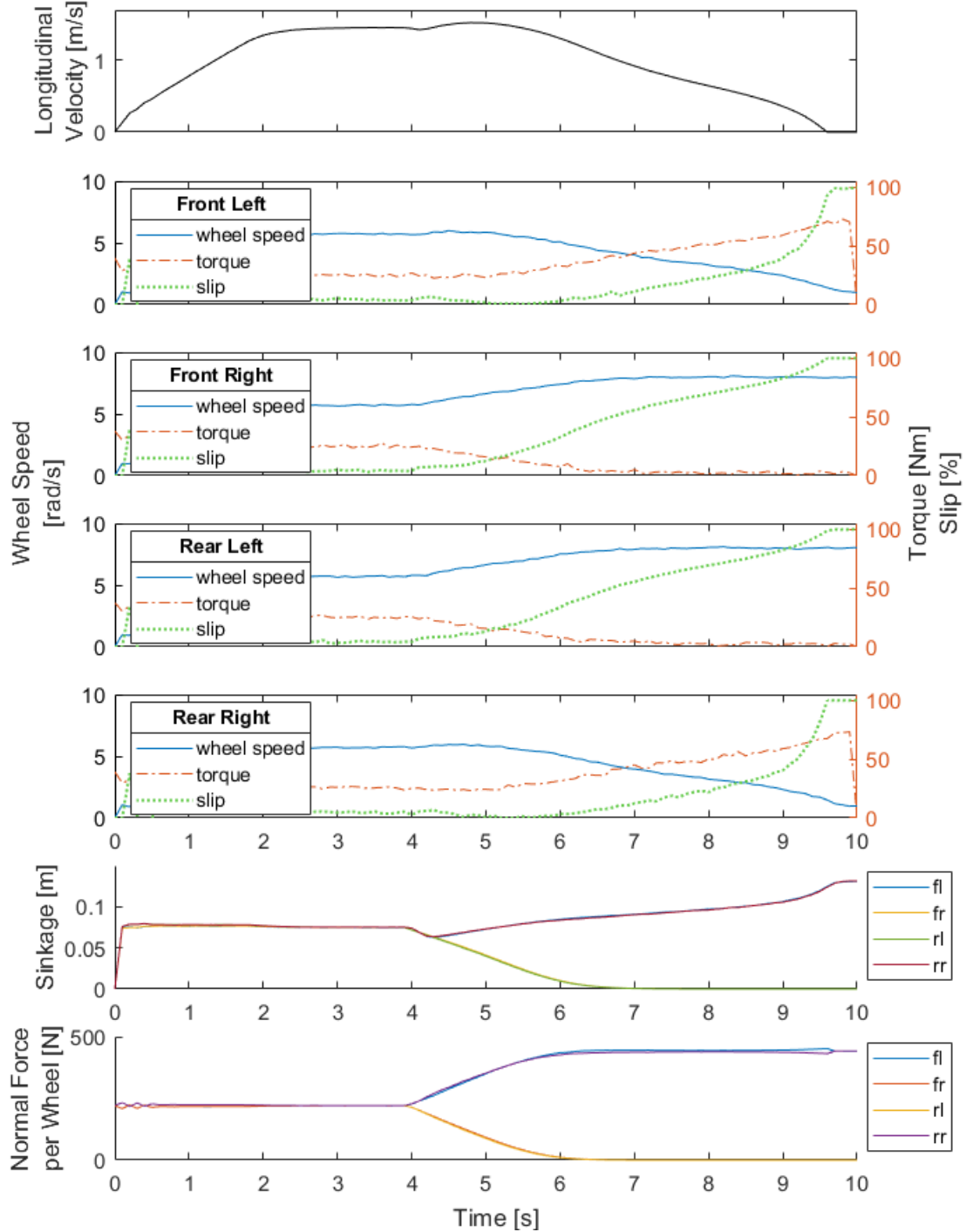


Figure 6.12: Simulation of abrupt increase in  $k$  at  $t = 4$  seconds for the front left and rear right wheels, with excavation considered for the front right and rear left wheels.

the same  $k$  and  $c$  values at each time step and the rear wheels encounter the same parameters as the front wheels, but delayed based on the distance traveled and the  $\sim 1$  meter wheelbase

of *FrostyBoy*.

Multiple simulations were run with different changes made to the two parameters to determine what variation in the terrain would result in a roll compliant rover to become immobilized. There were three interesting trends in the results from this series of simulations. The first was uncovered by varying only the pressure-sinkage stiffness parameter,  $k$ , and keeping cohesion,  $c$ , constant. In the immobilization of the rigid chassis rover, a change in  $k$  from 40 kPa/m to 65 kPa/m under wheels at a diagonal to one another instigated the positive feedback loop that caused the robot to lose all mobility. However, if the same sudden and coordinated increase on two wheels at a diagonal occurs with a roll-compliant rover, the mobility actually increases, similar to what can be seen in Fig. 6.10. These two wheels sink less, experience less terrain resistance, and therefore have higher drawbar pull to accelerate the robot. The roll angle of each axle, due to the different sinkage of each wheel, is only  $\sim 1^\circ$  on average, which results in a difference in normal load between two wheels on the same axle of less than 2 N. Most importantly, no wheel experiences dramatically increased levels of slip, meaning that the feedback loops of slip-sinkage and excavation are kept to a minimum.

To further investigate this improved resilience to changes in the terrain's pressure-sinkage parameters, the random walk model of only the stiffness parameter,  $k$ , was applied. In these runs, the only time an immobilization occurred was when  $k$  dropped below the lowest  $k$  value of 19.2 kPa/m observed with the GP (see Fig. 6.13 and note that the bottom plot is now showing the  $k$  value of the terrain the front wheels encounter vs. time). Therefore, the simulations show that roll compliance in this hypothetical rover would allow for far less susceptibility to variation in the stiffness parameter of the snowpack. The second finding came when adding the random walk of cohesion to the simulation. As was shown in the parameter sensitivity study for single wheels (see Fig. 6.5), slight changes in cohesion have a dramatic impact on a wheel's ability to gain traction. This can be attributed to the lower cohesion snow causing an increase in slip, which results in dynamic

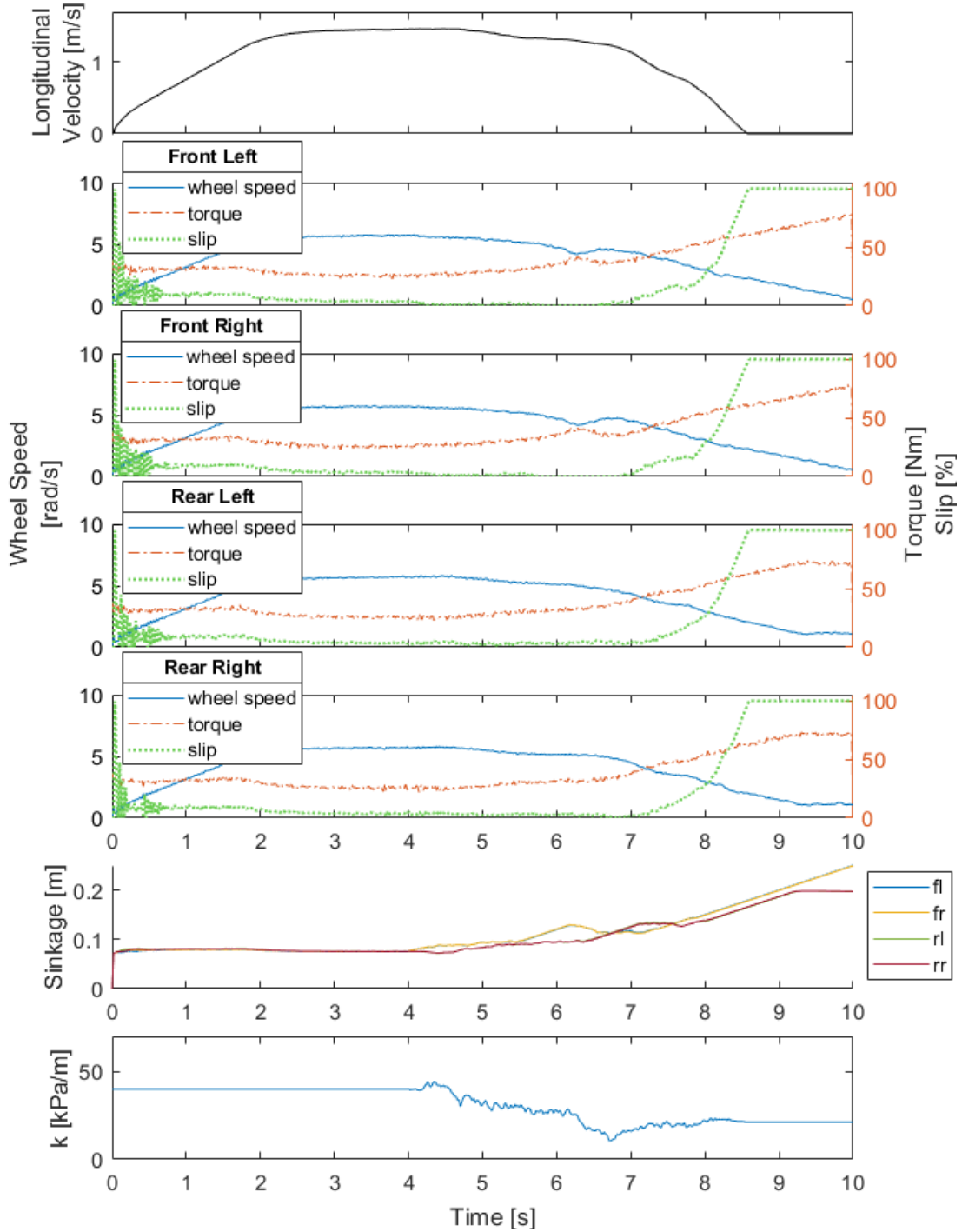


Figure 6.13: Simulation of varying terrain causing immobilization, with  $k$  taking on values based on a random walk model, shown in the bottom plot.

slip-sinkage and therefore increased terrain resistance. The third finding is that in every simulated case of the compliant rover becoming immobilized, the resistance torque never

became so high that the motors stalled. Instead, in every case, the rover became stuck due to high slip. It did not matter if only the stiffness parameter dropped to an untenable level, or only the cohesion parameter, or if it was a combination of the two. Every time, the wheels kept spinning and slipping, as sinkage increased for all four wheels and the forward velocity of the robot dropped to zero. This further validates the model as this is the only immobilization mode that has been observed with the rovers, *Yeti* and *Cool Robot*, in prior field seasons. *Yeti* actually has a central joint, which allows the axles to roll relative to one another, making it the closest analog to the simulated rover but not nearly as resilient as the simulated roll-compliant FrostyBoy due to Yeti's significantly narrower wheels. This rover primarily became immobilized when executing turns, with the added resistance to yaw causing the robot to slow down, slip, and start sinking. This can be seen in Fig. 6.14. While *Cool Robot* had a rigid chassis similar to *FrostyBoy*, it also had much narrower and more rounded wheels. Therefore, it is theorized that *Cool Robot* could not be completely supported and stable with only two of its wheels bearing all the weight. Instead, it needs three points of contact, making it behave similarly to the simulations, becoming immobilized only through excessive slip (discussed in section 4.2.2 and shown in Fig. 4.2).

While the true accuracy of these simulations cannot be assessed without an instrumented rover undergoing rigorous testing, this qualitative match between observations and simulations helps to reinforce the validity of the truth model and promotes its use in immobilization detection tests.

## 6.5 Summary

The ability to reproduce the immobilization seen in the test data suggests that the transfer of weight due to the rigid chassis of the robot is one of the principal factors in causing an immobilization with a rover traveling on snow. This finding, which could not have been uncovered in single-wheel studies, is important in informing the design of future rovers on



Figure 6.14: Example of a roll-compliant rover becoming immobilized during a turn due to excessive slip, evidenced by the snow buildup behind the right side wheels and the deep ruts created by the left side wheels.

snow. The truth model suggests that, even in keeping with requirements of being simple and low cost, future snow rovers could implement a passive compliance about the roll axis to maximize all four wheels' tractive force.

The second outcome of matching the simulation with the real data is that it serves as a form of validation for the truth model. Being able to tune the model with the steady-state operation of *FrostyBoy* and force immobilizations, just through the variation in the pressure-sinkage profiles of the terrain observed with the GP, gives confidence that the results and trends from the simulations can be used in investigations outside the testing done in Lebel-sur-Quévillon. It warrants the model's use in evaluating the effectiveness of the detection algorithm, developed in the next chapter, on simulated immobilizations for cases where the modeled rover does have compliance about the roll axis, or has motors operating under closed-loop speed control, or is performing a maneuver beyond just driving

straight. If shown to be effective and applicable, this would then allow for very few real-world tests to be required to establish baseline parameters of steady-state operation, as the truth model could then be used to generate a comprehensive suite of immobilization detection algorithms.

# Chapter 7

## Incipient Immobilization Detection

### 7.1 Introduction

The difficulty in developing a truth model using existing Bekker-Wong terramechanics theory and tuning a variety of terrain parameters to match collected data for a wheeled vehicle further reinforces the need for an online mobility assessment algorithm that is independent of these models and parameters. This is proven especially important for operating in a terrain, like snow, with such a wide range of terrain parameters. In snow, a lightweight, wheeled rover must strike a delicate balance between slipping enough to produce the requisite shear displacement to gain traction and slipping so much that slip-sinkage results in high terrain resistance, overwhelming the robot's tractive effort. However, instead of the circuitous method of using estimates of the wheel forces to determine terrain parameters to then calculate a change in operating point, the objective is to look for signatures in the data that can more directly be used to evaluate mobility. The collected data is used to generate a bank of behaviors that are indicative of steady-state operation and another set that serve as evidence of incipient immobilization. The multiple model estimation method (MME) is used in real time to decide which hypothesis is the most likely and whether it signifies nominal mobility or immobilizing terrain. In order for this to be valuable for a robot

traversing an ice sheet, it must be able to operate in real-time. The detection must occur early enough that the rover has time to adapt and maneuver out of the hazardous terrain. Yet, the detection method must be robust enough that it is not triggered by a temporary loss of traction from which the robot can recover. Finally, the bank of models indicative of the two states must be sufficiently universal to predict incipient immobilization even when terrain conditions or robot configurations are different than those directly tested.

## 7.2 Hypothesis Generation

The first step in developing a multiple model estimation algorithm is to generate the models which will serve as the hypotheses for how the robot is operating. To ensure the algorithm is robust, these models need to clearly and unambiguously fall into one of two groups: those that signify mobility and those that signify immobility. Unfortunately, the data set with which to generate these models is somewhat limited in scope. *FrostyBoy* was only operated in two types of snow (at the two different test sites), it functioned in an open-loop mode, and it was commanded to drive straight in an attempt to limit effects from lateral bulldozing resistance. Also, sinkage data cannot be used in the models since the ultrasonic sinkage sensors failed to produce usable data. In addition, the mode of immobilization seemed to be unique to the design of *FrostyBoy*, with the lack of suspension believed to cause a weight transfer to wheels at a diagonal that exacerbated the variability in the terrain parameters (analyzed in Ch. 6). However, the purpose of the truth model is to experiment with different scenarios, not measured directly, to see if incipient immobilization can still be detected. Also, models that do not depend on sinkage sensor data are more valuable, as the fewer variables involved, the lower the computational cost. Therefore, this approach still seemed valid and its effectiveness worth evaluating.

To generate hypotheses, various combinations of measured variables were analyzed as

inputs and outputs to a simple discrete-time state-space model.

$$\mathbf{x}_{s+1} = \Phi \mathbf{x}_s + \Gamma \mathbf{u}_s \quad (7.1)$$

$$\mathbf{y}_{s+1} = \mathbf{H} \mathbf{x}_s \quad (7.2)$$

For each combination, the system parameters were generated using the canonical variate analysis (CVA) approach for system identification [71], forcing the output matrix,  $\mathbf{H}$ , to the identity matrix, with the system and input matrices,  $\Phi$  and  $\Gamma$ , obtained using a prediction error minimization algorithm [72].

This process is easily performed using a command, *ssest*, in the System Identification Toolbox in MATLAB, allowing for rapid testing of several input/output combinations with different model orders specified to fit various sections of the time domain data. Each identified system was evaluated based on its goodness of fit with the data from which it was generated using the normalized root-mean-square error cost function. The system parameter values identified from characteristic immobilization segments of data were also compared with those from segments of normal mobility, to assess their uniqueness.

Many combinations of input and state variables were evaluated as potential system models, with the majority based on the clear divergence of each wheel's nominal operation seen in Fig. 6.8. Therefore, significant effort was focused on using slip and torque in the system model. However, the calculated slip from measurements of wheel speed and longitudinal velocity was too noisy for it to be a reliable predictor. The other most promising system model set torque as the input and wheel speed as the state. While very effective at predicting an upcoming immobilization in the real data, from which the hypotheses were generated, it failed in any simulation of conditions outside of those measured. After significant effort through trial and error, it was determined that the system model with the best fit, uniqueness, and potential for incipient immobilization detection was a first order model with wheel torque and wheel speed as the inputs,  $\mathbf{u}$ , and robot velocity as the state,  $\mathbf{x}$ .

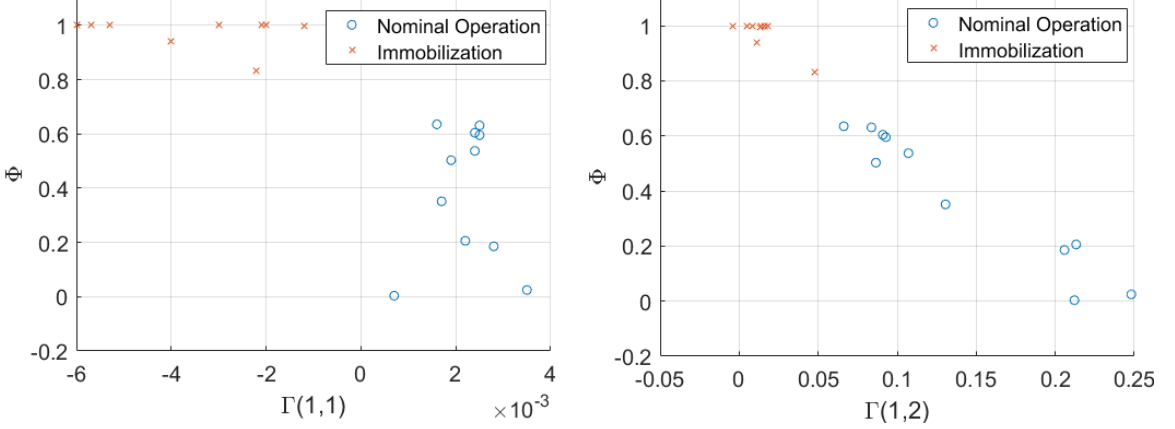


Figure 7.1: Plots of the hypothesis values to show separability of model values during nominal, steady-state operation and during an immobilization.

$$\mathbf{u} = \begin{bmatrix} T \\ \omega \end{bmatrix} \quad (7.3)$$

$$\mathbf{x} = [v_x] \quad (7.4)$$

This means that each hypothesis,  $\mu$ , is made up of a  $1 \times 1$  matrix,  $\Phi$ , and a  $1 \times 2$  matrix,  $\Gamma$ , that modify the state and input respectively. Hypotheses of nominal mobility were generated from the time series data in which the rover accelerates and reaches steady state. The immobilization hypotheses were generated from the data leading up to the complete loss of forward velocity. Of the seventeen immobilization events from the two different test sites, only those six with the most distinct ramp ups to steady-state operation and subsequent immobilizations were used to generate the hypotheses, with one nominal and one immobilization hypothesis generated for each wheel. Then, the values were plotted for  $\Phi$  vs.  $\Gamma(1,1)$  and  $\Gamma(1,2)$  and the duplicate hypotheses within the same set were removed to limit the number of parallel filters required, leaving eleven nominal hypotheses ( $A_{nom} = 11$ ) and nine immobilization hypotheses ( $A_{imm} = 9$ ) for a total of twenty ( $A_{total} = 20$ ), as can be seen in Fig. 7.1. Since the torque-speed curve for a BLDC motor is well un-

derstood and characterized, the idea of monitoring the operating torque and wheel speed of the motor and evaluating how this translates to overall rover velocity is a simple idea. However, it is this simplicity that allows hypothesis selection to run much faster than the 10 Hz rate of data collection without requiring any assumptions about, or solutions to, the equations describing the pressure distribution below the wheels. This method is also similar to other condition monitoring techniques, such as the motor current signature analysis (MCSA) used in sensing faults with induction motors [73]. While MCSA uses current spectral analysis to detect anomalies instead of a Bayesian inference algorithm, the basic principle of identifying the operating characteristics of a motor to sense any changes before a rapid decline in performance or a catastrophic failure occurs is embodied by this MME immobilization detection method [74]. It also allows for a robust set of hypotheses to be identified from a small set of immobilization data, meaning that the extensive training data required to train a machine learning algorithm is unnecessary. To prove this, the following sections will show how selecting between these twenty hypotheses can be used to reliably detect immobilization not only in the collected data but also in artificial immobilizations generated using the truth model.

### 7.3 Bayesian Multiple Model Estimation Method

The algorithm that forms the basis of choosing between these hypotheses uses recursive Bayesian inference to find which hypothesis best accounts for the wheel's operation at each point in time [75]. In this multiple model estimation (MME) approach, each hypothesis is assigned a Kalman filter that determines the likelihood of a measurement given the system parameters within each hypothesis. A posterior probability for each hypothesis is then calculated using Bayes' rule to combine the likelihood probability of the current time step with the *a priori* probability for that hypothesis from the previous time steps. Typically, each hypothesis is defined by the values of the system matrices ( $\Phi$ ,  $\Gamma$ , and  $\mathbf{H}$ ) as well as a

disturbance input matrix,  $\mathbf{Q}$ , and a measurement noise matrix,  $\mathbf{R}$  [75]. For this application, the hypotheses are only defined by matrices  $\Phi$  and  $\Gamma$ , with  $\mathbf{H}$ ,  $\mathbf{Q}$ , and  $\mathbf{R}$  being the same for all possible hypotheses. Therefore, at each time step,  $s$ , the Discrete Time Kalman Filter (DTKF) for a given hypothesis,  $\mu_a$ , to calculate an estimate of the state,  $\hat{\mathbf{x}}_s$ , is given by the sequence

$$\hat{\mathbf{x}}_s^- = \Phi \hat{\mathbf{x}}_{s-1}^+ + \Gamma \mathbf{u}_{s-1} \quad (7.5)$$

$$\mathbf{P}_s^- = \Phi \mathbf{P}_{s-1}^- \Phi^\top + \Lambda \mathbf{Q}'_{s-1} \Lambda^\top \quad (7.6)$$

$$\mathbf{K}_s = \mathbf{P}_s^- \mathbf{H}^\top [\mathbf{H} \mathbf{P}_s^- \mathbf{H}^\top + \mathbf{R}_s]^{-1} \quad (7.7)$$

$$\hat{\mathbf{x}}_s^+ = \hat{\mathbf{x}}_s^- + \mathbf{K}_s [\mathbf{z}_s - \mathbf{H} \hat{\mathbf{x}}_s^-] \quad (7.8)$$

$$\mathbf{P}_s^+ = [(\mathbf{P}_s^-)^{-1} + \mathbf{H}^\top \mathbf{R}_s^{-1} \mathbf{H}]^{-1} \quad (7.9)$$

where the state estimate is the expected rover velocity. This allows for the measurement residual,  $\mathbf{r}_s$ , and the residual covariance matrix,  $\mathbf{S}_s$  to be calculated with respect to the measured ground speed,  $\mathbf{z}_s$ , according to

$$\mathbf{r}_s = \mathbf{z}_s - \mathbf{H} \hat{\mathbf{x}}_s^- \quad (7.10)$$

$$\mathbf{S}_s = \mathbf{H} \mathbf{P}_s^- \mathbf{H}^\top + \mathbf{R}_s \quad (7.11)$$

which then can be used to estimate the probability distribution of the measurement,  $\mathbf{z}_s$ , given the estimated state predicted by the hypothesis parameters,  $\hat{\mathbf{x}}_s(\boldsymbol{\mu})$ . This distribution is defined by

$$\text{pr}[\mathbf{z}_s | \hat{\mathbf{x}}_s(\boldsymbol{\mu})] = \frac{1}{(2\pi)^{1/2} |\mathbf{S}_s|^{1/2}} e^{-(1/2)\mathbf{r}_s^\top \mathbf{S}_s^{-1} \mathbf{R}_s} \quad (7.12)$$

Since each hypothesis has its own Kalman filter, this process is repeated for all  $A$  hypotheses, with the probability of each hypothesis given the measurement defined by

$$\Pr(\boldsymbol{\mu}_a | \mathbf{z}_s) = \frac{\text{pr}[\mathbf{z}_s | \hat{\mathbf{x}}_s(\boldsymbol{\mu}_a)] \Pr(\boldsymbol{\mu}_a | \mathbf{z}_{s-1})}{\sum_{i=1}^A \left\{ \text{pr}[\mathbf{z}_s | \hat{\mathbf{x}}_s(\boldsymbol{\mu}_i)] \Pr(\boldsymbol{\mu}_i | \mathbf{z}_{s-1}) \right\}} \quad (7.13)$$

The most likely hypothesis for the wheel can then be determined from the highest conditional probability. The wheel can then be classified as almost immobilized or running nominally based on the group to which the most likely hypothesis belongs.

Testing this algorithm on the data collected in Lebel-sur-Quévillon allowed for certain parameters of the Kalman filter to be tuned and for new criteria for the triggering of an immobilization response to be developed. The state estimate depends on the relative weights of the disturbance matrix,  $\mathbf{Q}$ , and the measurement noise matrix,  $\mathbf{R}$ . In general, increasing  $\mathbf{Q}$  relative to  $\mathbf{R}$  places more confidence in the measurements, and the opposite change places more confidence in the model predictions. Since the model is what we are trying to determine in the MME method,  $\mathbf{Q}$  will be high relative to  $\mathbf{R}$ . Through testing, the best results came when  $\mathbf{Q}$  was set to  $20 \text{ (m/s)}^2$  and  $\mathbf{R}$  was set to  $1 \text{ (m/s)}^2$ . However, since both values can vary by  $\pm 20\%$  without any significant impact on detection, the algorithm is not overly sensitive to these parameters. The other tuning mechanism is the adjustment of how *a priori* probabilities are reset after each time step. The recursive Bayesian inference process is designed for convergence, with each new measurement either reinforcing the ‘belief’ that the wheel system is behaving according to the model of a given hypothesis or undermining this ‘belief’. This is not well suited for the use case for which this incipient immobilization detection method is being designed. Unlike the test sites from which the data was collected, the patches of immobilizing terrain are sporadic on the ice sheets of Greenland and Antarctica, yet the loss of mobility could happen just as quickly. Therefore, if the *a priori* probabilities have been converging on the hypotheses indicating good mobility for even a few seconds, the sensitivity of the system is critically compro-

mised. To improve the response time of the system, various methods of flattening the prior distributions at each time step were tested. Resetting the prior distributions to be uniform naturally resulted in the highest sensitivity, but also caused an unacceptable rate of false alarms. Even when requiring that immobilizing hypotheses are chosen for multiple time steps before a wheel is flagged to be ‘at risk’, the false alarm rate was still too high. From a final implementation standpoint, this would be untenable since the robot would be unnecessarily maneuvering and using excess energy to avoid perfectly trafficable snow. Therefore, the idea of convergence was applied to the rover system as a whole, using information from all four wheels to evaluate mobility rather than relying on any single wheel.

In the final configuration of the detection method, each wheel has  $A_{total}$  Kalman filters running in parallel, estimating the likelihood of the measured rover velocity given the torque and wheel speed for each hypothesis. These likelihoods are combined with a uniform prior to obtain the respective probability of each hypothesis given the measurement. The average of the probabilities for immobilization hypotheses are subtracted from the average of the probabilities for nominal hypotheses to get a value,  $\xi$ , for each wheel, with more negative values signifying higher risk of that wheel becoming immobilized.

$$\xi = \sum_{a=1}^{A_{nom}} \frac{\Pr(\boldsymbol{\mu}_a | \mathbf{z}_s)}{A_{nom}} - \sum_{a=A_{nom}+1}^{A_{total}} \frac{\Pr(\boldsymbol{\mu}_a | \mathbf{z}_s)}{A_{imm}} \quad (7.14)$$

Finally, to reduce the rate of false alarms, the  $\xi$  values from pairs of wheels were summed, requiring two wheels to be ‘at risk’, before a full immobilization is flagged. The pairs of wheels that were shown to most accurately predict an immobilization were those at a diagonal and those on the same axle. Pairing the left-side wheels or the right-side wheels of the robot resulted in false alarms during turning maneuvers. While the robot is highly susceptible to becoming immobilized during a turn, as it needs to overcome the added lateral terrain resistance, a simulated immobilization event during a turn would still be detected with the existing pairings. Therefore, the final detection algorithm calculates  $\Xi$

values for each pairing

$$\Xi_1 = \xi_{fl} + \xi_{fr} \quad (7.15)$$

$$\Xi_2 = \xi_{rl} + \xi_{rr} \quad (7.16)$$

$$\Xi_3 = \xi_{fl} + \xi_{rr} \quad (7.17)$$

$$\Xi_4 = \xi_{fr} + \xi_{rl} \quad (7.18)$$

and if any of the four  $\Xi$  values drop below a threshold, an immobilization is considered imminent, and the robot needs to take immediate action to maintain mobility.

## 7.4 Detection Results

### 7.4.1 Collected Data

The method described above was developed and refined using the immobilization event data collected in Lebel-sur-Quévillon. From these data, a threshold value of zero was established for all  $\Xi$  values. If any of these four values drop below zero, it indicates the likelihoods of the immobilization hypotheses outweigh the likelihoods of the nominal operating hypotheses for that pair of wheels, and the algorithm will flag an immobilization. In addition, to prevent false alarms, an immobilization flag is not triggered unless the robot velocity dips below 1 m/s, as the rover's momentum at higher speeds occasionally allows it to push past immobilizing terrain even if multiple wheels show the signature of an unsustainable motor operating point.

The performance of this type of classification algorithm is typically evaluated by comparing how the algorithm categorized an event vs. the actual category of the event. For example, a true positive would be an event in which the rover is about to lose mobility and the algorithm successfully warns of incipient immobilization before the robot's velocity drops to zero. An immobilization that the algorithm fails to detect, would be a false nega-

Summary of MME Results - Lebel-sur-Quévillon Data					
Event Number	Stop Distance [m]	Stop Time [s]	Velocity at Detect [m/s]	Distance to $v_x = 0$ [m]	Time to $v_x = 0$ [s]
<b>1-1</b>	0.54	1.2	0.97	0.45	1.1
<b>1-2</b>	0.88	1.5	0.86	0.38	1.0
<b>1-3</b>	1.34	1.8	0.45	early	early
<b>1-4</b>	1.58	2.6	0.91	early	early
<b>1-5</b>	0.46	1.0	0.82	0.15	0.7
<b>1-6</b>	2.66	4.7	0.58	0.67	2.1
<b>1-7</b>	2.31	3.7	0.95	1.26	2.8
<b>1-8</b>	6.07	8.0	0.98	4.42	6.6
<b>1-9</b>	4.69	5.2	0.99	early	early
<b>2-1</b>	2.64	4.0	0.88	1.51	3.0
<b>2-2</b>	0.38	1.3	0.84	early	early
<b>2-3</b>	1.95	2.4	0.65	early	early
<b>2-4</b>	0.78	2.4	0.56	0.61	2.1
<b>2-5</b>	0.67	1.7	0.70	early	early
<b>2-6</b>	0.45	1.1	0.70	0.21	0.8
<b>2-7</b>	1.00	3.4	0.29	0.28	1.8
<b>2-8</b>	2.29	3.6	0.82	0.99	2.2
<b>AVG</b>	1.81	2.92	0.76	0.99	2.20
<b>MAX</b>	0.38	1.00	0.29	0.15	0.70
<b>MIN</b>	6.07	8.00	0.99	4.42	6.60

Table 7.1: Results from applying the MME algorithm on data collected from immobilization events in Lebel-sur-Quévillon. The first number of the event number corresponds to the test site. The "early" entries mean that an immobilization was flagged by the algorithm before the start of the immobilization event that actually resulted in the rover's complete loss of mobility and are not included in the results' statistics.

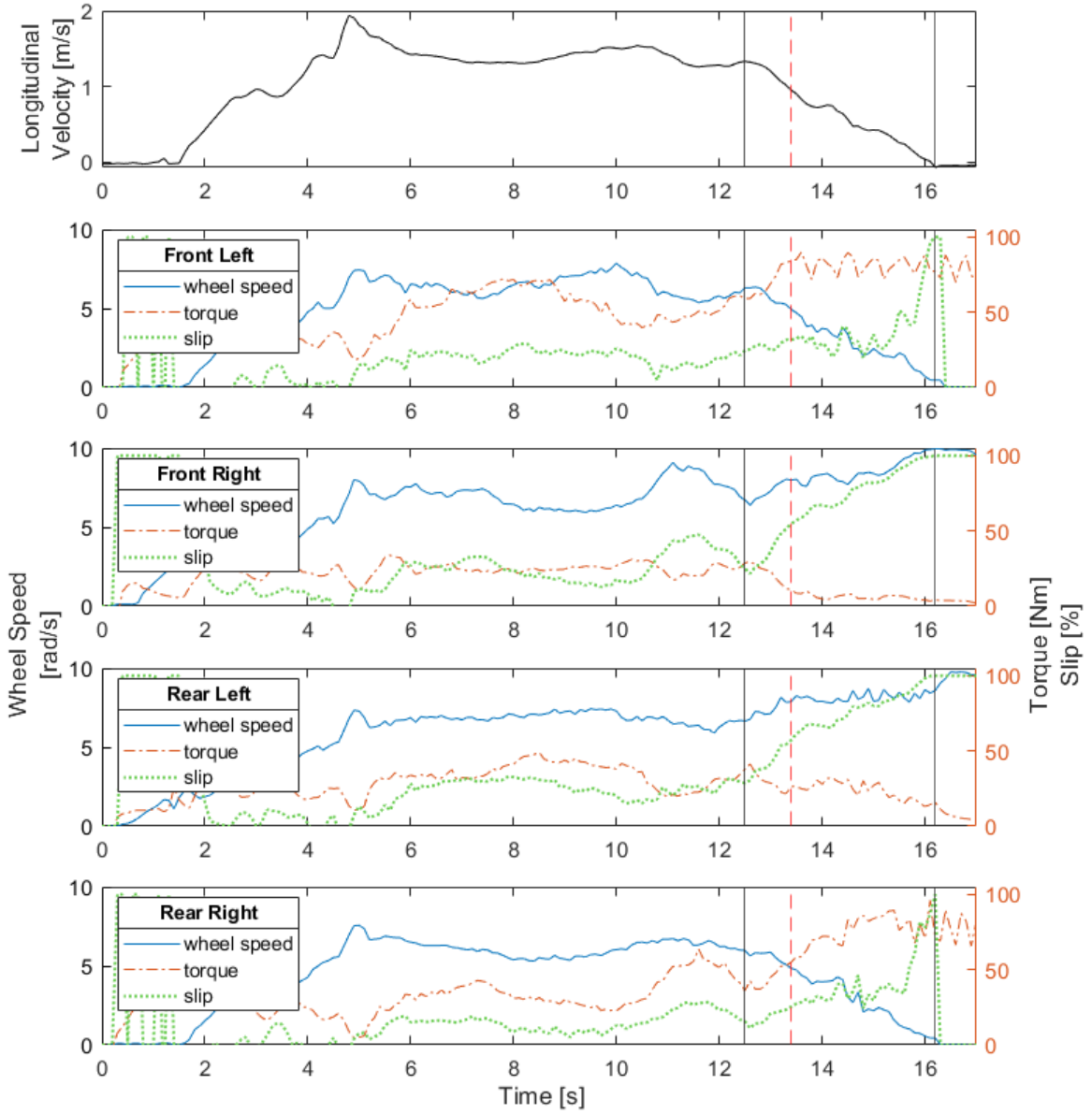


Figure 7.2: Longitudinal velocity and each wheel's speed, applied torque, and slip shown for Event 1-7. The first black vertical band marks the start of the immobilization, the second black vertical band indicates when the vehicle has become fully immobilized, with the dashed red line showing the time of detection. All immobilization events from Lebel-sur-Quévillon can be found in Appendix A.

tive. A false positive would be when the rover is operating normally, with good mobility, yet the algorithm flags an impending immobilization. Finally, a true negative would be when the rover has nominal mobility and the algorithm does not detect an immobilization. However, a few issues arise when trying to define what should be classified as an immobi-

lization in the real data. An obvious immobilization is when the longitudinal velocity of the rover reaches a steady state of zero when the rover has not been commanded to stop and the expected velocity is therefore nonzero. However, this definition means that any situation in which the rover’s mobility is significantly compromised and the algorithm detects a loss of mobility, yet the rover never reaches a full standstill, would be erroneously classified as a false positive. In addition, bounds would need to be defined for an immobilization event in the real data since a flag raised when the rover has good traction, meters before it is actually stuck, could be misconstrued as a true positive. In this example, technically the algorithm did warn of the immobilization before the rover’s velocity dropped to zero. However, the MME model was not behaving as intended since the rover’s mobility was nominal at the time of the alert, meaning the alert was premature. It is for these reasons that the standard classification terms, and the associated metrics of precision and recall, are not used to assess the detection performance.

Instead, the results of applying the MME method to the data from Lebel-sur-Quévillon were analyzed by looking at two tests. The first test was performed to ensure that the algorithm does not trigger in cases where a user initiates a stop and the rover comes to rest due to the motors’ programmed deceleration profiles. For the eight events tested in which *FrostyBoy* was commanded to stop rather than becoming immobilized due to the terrain, the algorithm never detected an incipient immobilization. With this simple check accomplished, the algorithm’s performance was then assessed on cases where the rover’s velocity did reach a steady state zero value due to immobilizing terrain. The results of these tests are shown in Table 7.1, with Fig. 7.2 showing an example of when detection occurs (red-dotted line) in relation to the rover’s velocity and to each wheel’s rotational speed, torque, and slip. Plots of all the events can be found in Appendix A. For each of these immobilization events, bounds are established for when the rover begins to lose mobility and when the rover has become stuck. While the exact point in time when the robot starts to lose traction is difficult to determine, this is estimated by when the IMU velocity begins

to steadily decline to zero and is marked by the first vertical black line in Fig. 7.2. The second vertical black line marks the time at which the robot's velocity reaches zero. This allows for algorithm detections that occur outside of these bounds to be excluded from the results' statistics. Instead, these "early" detections, that did not result in a complete loss of mobility, were analyzed qualitatively, and it was found that the velocity, torque, and wheel speed signatures, with which these "early" flags are associated, are identical to ones that did result in the robot becoming stuck. In addition, the terrain on which the rover was being tested was already at the edge of trafficability, meaning that if the rover was to encounter this patch of snow on a traverse, it is better to limit how far the rover travels on questionable terrain before raising an alert. So for all of these cases of "early" detections, it appears that the algorithm was functioning correctly and was not falsely identifying nominal mobility as potentially immobilizing. Also in these cases, the MME method's final warning was within the established bounds, meaning that the immobilizing terrain that ultimately brought the robot to a halt was still able to be identified.

For all of the events observed in Lebel-sur-Quévillon, the table shows the wide range of results in how quickly and over what distance the rover can become immobilized. The table also shows that the velocity at the time of detection is generally quite high, with an average value of 0.76 m/s, meaning that a simple threshold on rover velocity would perform significantly worse than the MME algorithm presented. However, the best way to judge the performance of this algorithm is by looking at the distance and time between the immobilization flag and the complete loss of forward velocity for the events without early detection. In these cases, the MME could notify the robot of an impending loss of mobility, on average,  $\sim$ 1 meter, or about 60% of a wheel revolution, before zero velocity. However, this ranged from a mere 0.15 meters to a full 4.42 meters of warning. While 15 cm is not enough distance to avoid driving into an area of either low cohesion or low stiffness snow, the 0.7 seconds of response time could drastically reduce the excavation and slip-sinkage that occurs at high slips. Also, if the rover has specific control modes to

improve its mobility over questionable terrain, or if it's towing a load on a winch, this gives plenty of warning to either alter its operation or pay out cable on the winch. The first step is warning the rover of its decreased mobility, and since the MME method triggered an alert for all immobilizations observed with *FrostyBoy* in Lebel-sur-Quévillon, with at least 0.7 seconds before a complete loss of forward momentum, this method has proven to be a valuable tool in incipient immobilization detection.

#### 7.4.2 Simulated Data

Due to the unique characteristics of *FrostyBoy*'s immobilizations, from which the system hypotheses were generated, the Immobilization Detection Algorithm (IDeA) was also tested on a number of simulations to assess its effectiveness when the scenario changed. *FrostyBoy*'s unique immobilizations were theorized to be attributable to its rigid chassis and the transfer of weight from four wheels to two wheels, as discussed in Ch. 6. To prove the algorithm's viability for potential future designs of a snow rover, all simulations are run with the assumption that each axle has compliance about the roll axis, but otherwise has identical parameters to the *FrostyBoy* rover. The same random walk of terrain variability (described in section 6.4) is introduced into the simulations to incite immobilizations. There were three distinct tests on which the IDeA was tested. The first test simply assessed if and when the algorithm would pick up on an immobilization for a rover driving straight with all four motors receiving the same open-loop voltage. The second experiment tested the IDeA when all four motors instead operated under closed-loop speed control. And the final test investigated the operation of the rover under closed-loop speed control, but with different speed setpoints for the left and right sides, simulating the rover performing a turn.

In all three tests, the IDeA had no issues not only detecting the immobilization but doing so with enough warning that the rover could enter control modes to prevent getting stuck. An example simulation of the first test is shown in Fig. 7.3. This is identical to the tests described in section 6.4, but with different random walks of  $k$  and  $c$  used to incite

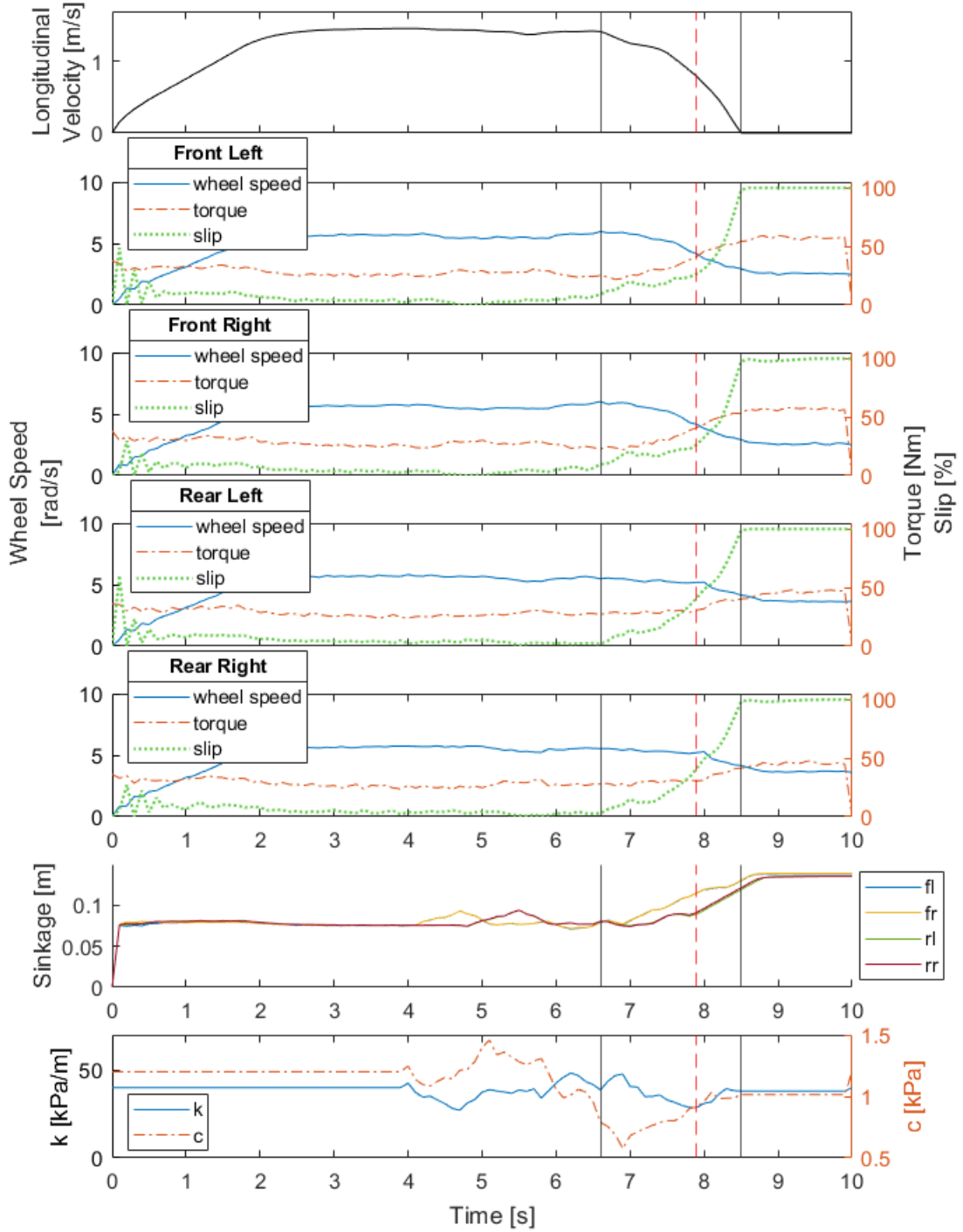


Figure 7.3: Simulation and detection of an immobilization caused by varying terrain parameters  $k$  and  $c$ , with motors in open-loop speed control.

the immobilization. In this particular example, the rover was traveling at 0.8 m/s when the immobilization was detected, with 0.25 meters and 0.6 seconds until its longitudinal

velocity dropped to zero. While this is just one example with one random walk model for  $k$  and  $c$ , the trend with this test showed that the IDeA detected all simulated immobilizations, but the time and distance between detection and zero velocity decreased compared to the real data. This is primarily a result of the rover decelerating much faster in the simulation once entering a high slip condition than that observed in Lebel-sur-Quévillon. This could be an artefact of the simulation, or it could be that in the very different immobilization scenario of all four wheels slipping, the dynamic slip-sinkage does cause this rapid rise in terrain resistance as modeled. This requires further investigation in future studies with a newly designed rover.

The encouraging results of this investigation are that in running each motor in the simulation at a constant speed with a closed-loop PI controller and feeding in the same random walk models for  $k$  and  $c$  as the open-loop cases above, the IDeA is actually more effective at detecting immobilizations earlier, and at a longer stopping distance, compared to running in open-loop mode. For example, a simulation with closed-loop speed control<sup>5</sup> was run with identical terrain parameter variation as that shown in Fig. 7.3, but the IDeA is able to flag a potential immobilization 0.2 seconds earlier, meaning that the rover speed at detection is 0.92 m/s and has 0.32 meters before its velocity drops to zero (see Fig. 7.4). A comparison of the open-loop vs. closed-loop speed control showed this trend across the board, no matter the random walk model that resulted in an immobilization. This is very important since closed-loop speed control would always be used in the future.

The final test was to add a turning maneuver to the simulation. During testing in Lebel-sur-Quévillon, the robot was commanded to go straight by giving all four motors the same voltage setpoint in an effort to reduce the variables contributing to its immobilization. In a turn, lateral bulldozing resistance reduces the rover's ability to gain forward traction and therefore makes it more susceptible to immobilization. This means that it is most important

---

<sup>5</sup>Closed-loop speed control in the simulation was accomplished by adding a PI controller to the applied voltage for each wheel. This feedback loop used the difference between the wheel speed setpoint and simulated wheel speed (no noise added), as the error, with the coefficients set to,  $K_p = 1$  and  $K_i = 0.01$ .

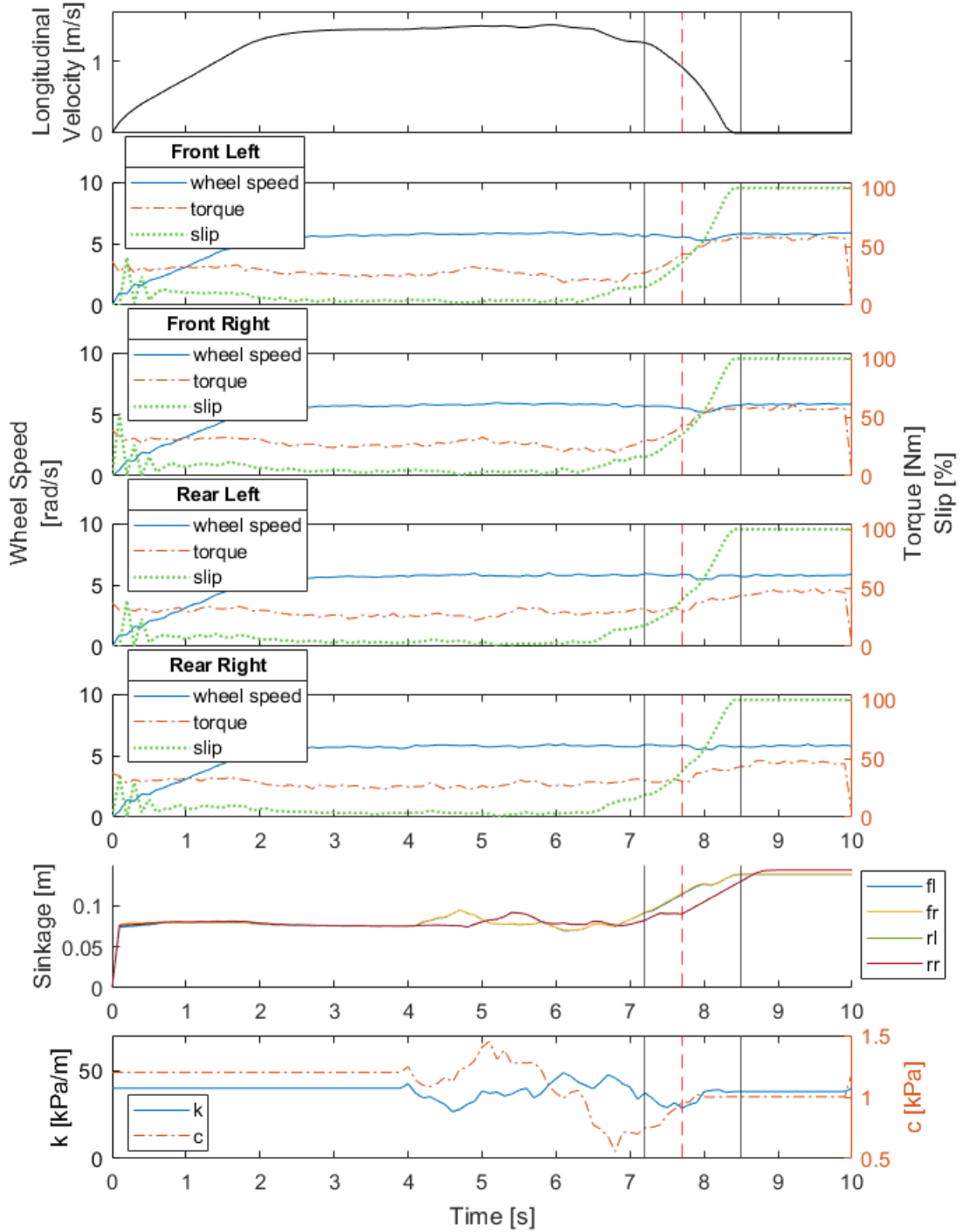


Figure 7.4: Simulation and detection of an immobilization with motors in closed-loop speed control. The variation of terrain parameters  $k$  and  $c$  are identical to those presented in Fig. 7.3.

for the IDeA to warn of a potential loss of mobility during a turn. These simulations were set to run longer, with a different set of  $k$  and  $c$  variables than the test above, to ensure

that the robot reached a steady-state yaw rate before an immobilization was initiated. After four seconds of driving straight, the left-side wheels were set to a closed-loop speed set-point of 3.5 rad/sec, while the right-side wheels maintained 5.8 rad/sec to turn the rover towards the positive y-direction. Of all the simulations run, this study was the furthest from the experiments actually performed in the field with *FrostyBoy*. There is no data from Lebel-sur-Quévillon collected during a commanded turn, making it difficult to accurately determine the restoring moment that resists yaw,  $M_{res}$  from (6.2). Also, the truth model was designed for simple longitudinal motion, so there is no explicit  $v_y$  term, and the lateral bulldozing resistance forces are not calculated. Without these factors, the turning maneuver's negative impacts on mobility will be less pronounced in the simulation. However, the model does replicate the negative drawbar pull for the wheels with lower relative speeds (left side wheels in this case) and the potential for high slips for the wheels with higher relative speeds (right side wheels). An example of a simulated immobilization that results from this difference between left and right side wheel speed commands can be found in Fig. 7.5.

The IDeA is able to predict this loss of mobility in a turn when the rover still has a longitudinal velocity of 0.75 m/s, with 0.8 seconds and 0.62 meters before it comes to a halt. Once again, this proved to be the norm as various random walks of the terrain variables were simulated, as well as different speed setpoints for the right-side and left-side wheels, with the IDeA detecting all immobilizations before the rover lost momentum. However, the most promising results were obtained when a simple traction control sequence was initiated upon the warning of incipient immobilization during these maneuvers. In these simulations, once the flag of a potential loss of traction was raised, the setpoint for all four wheels were set to the same, low speed value, in an attempt to gain full longitudinal traction by commanding the rover to go straight and eliminating the negative effects on mobility resulting from turning. An example of the effect this had on the rover's mobility is shown in Fig. 7.6, which uses the same terrain model as Fig. 7.5, but with both the right and left

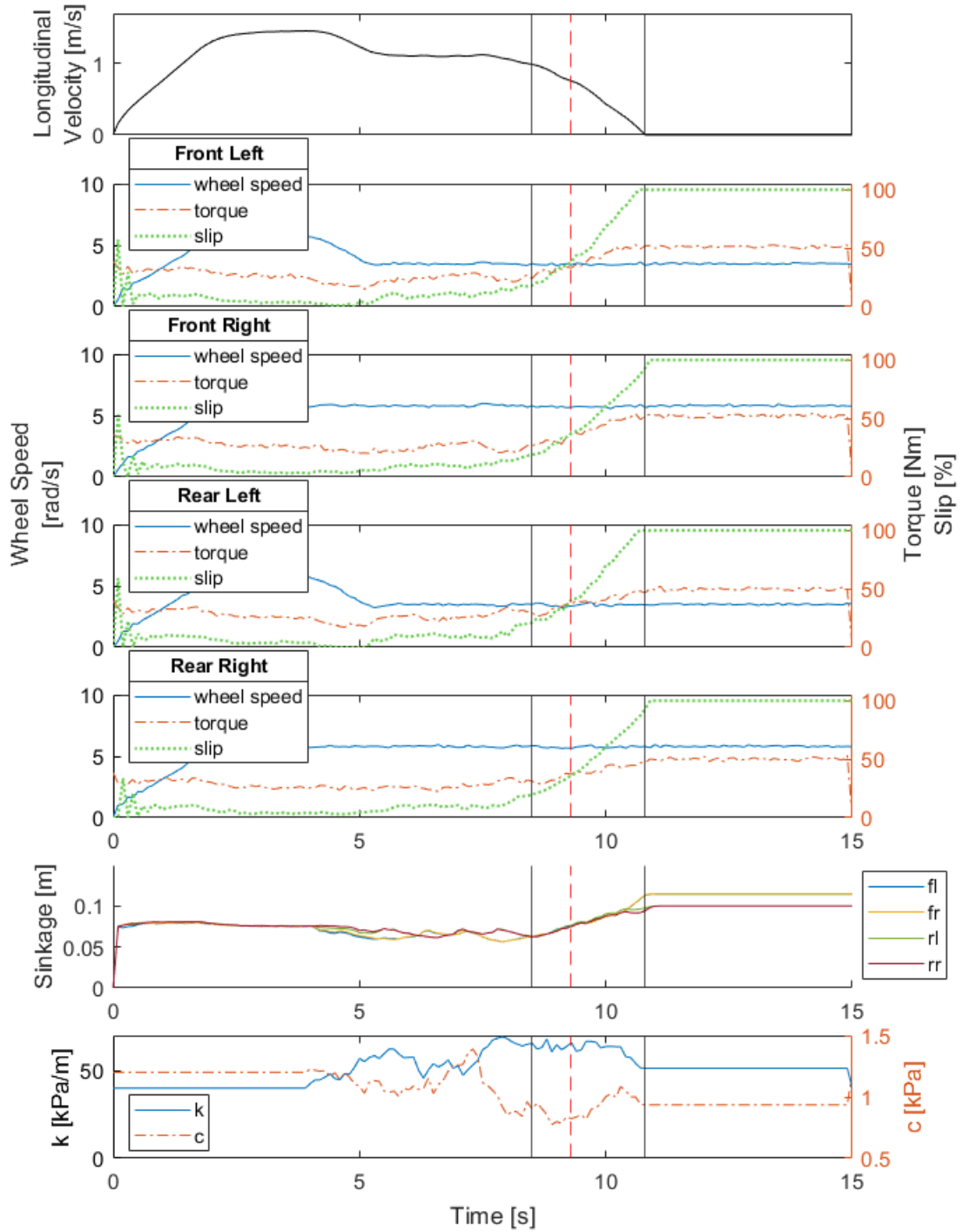


Figure 7.5: Simulation of a turning robot that becomes immobilized during the turn.

side wheels set to run at 3.5 rad/s once the IDeA warns of an immobilization at 9.3 seconds. In this simulation, the simple reduction of speed and the command to go straight actually resulted in the rover continuing in the longitudinal direction for another 2.7 meters beyond

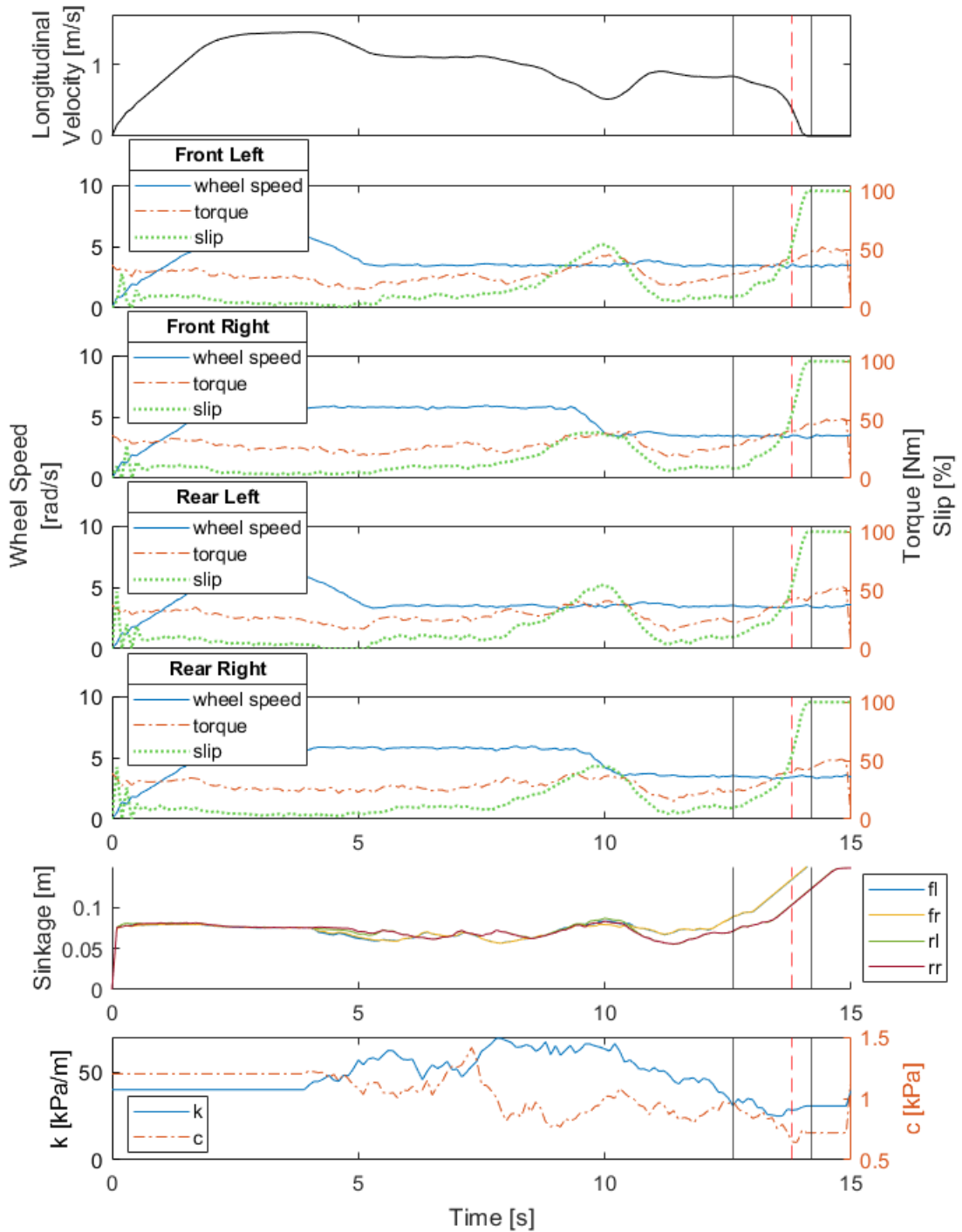


Figure 7.6: Simulation of a turning robot, commanded straight once incipient immobilization is detected. The same terrain variability was introduced into the simulation as was for Fig. 7.5.

where it became immobilized in the previous simulation, where no corrective action was taken (see Fig. 7.7). The IDeA was also still able to warn of the rover's final immobilization

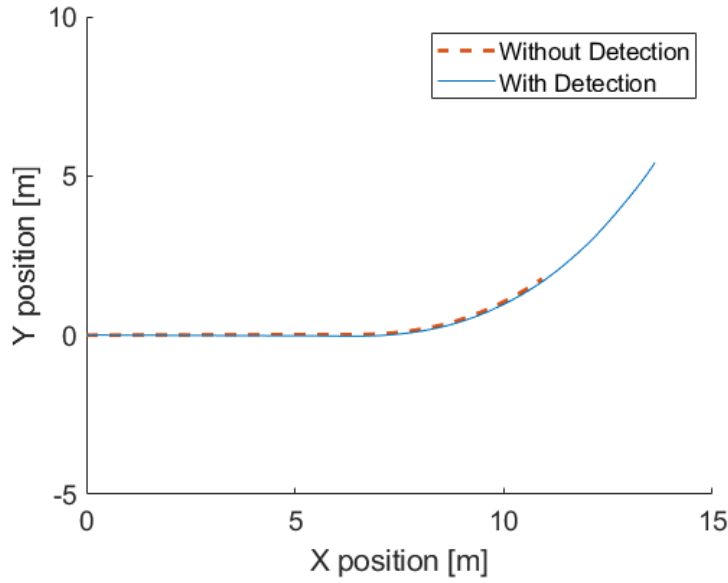


Figure 7.7: X and Y position of the rover tracked for turning simulations with and without immobilization detection.

after recovering from the first. Due to the potential faults and unvalidated aspects of this simulation, the goal of detailing this example is not to prove out the control sequence necessary to navigate low stiffness or poorly bonded terrain when executing a turn. Instead, this example is meant to showcase the Immobilization Detection Algorithm's reliability and its potential in preventing immobilizations.

## 7.5 Summary

The results from applying the IDeA to both real and simulated immobilization data shows its effectiveness and reliability in quickly identifying an incipient loss of mobility. The MME only requires torque, wheel speed, and speed over ground measurements as inputs to the model, making it feasible and inexpensive to implement on any rover. The lack of sinkage data, due to these sensors' failure, simplifies the detection method and reduces the cost and complexity of the sensor suite necessary on the rover. Also, by producing useful results with only twenty hypotheses per wheel and small input matrices, this implementa-

tion of the MME algorithm has a very low computational cost. It is able to run much faster than solving the terramechanics equilibrium equations and faster than similar algorithms involving hundreds of hypothetical parameter sets that each require a separate Kalman filter. Testing this algorithm on the collected data proved that this method cannot be applied for just one wheel and therefore, could not have been developed from single-wheel testbed studies. Instead, it requires analyzing the response of pairs of wheels and their combined impact on the velocity of the rover. This is the only way to reduce false alarms and reliably detect incipient immobilization. Finally, testing this algorithm on simulations showed that this method is not only applicable to the data set from which it was generated. Instead, the promising results from flagging immobilizations generated by the truth model in scenarios outside the scope of the experiments with *FrostyBoy* in Lebel-sur-Quévillon indicate that this method could be applied to rovers that are of a different design, that encounter more variation in the terrain, and that operate under a different control scheme. Further studies need to be performed to test this detection method with the configurations that have only been simulated. In addition, for a wider set of nominal and immobilization hypotheses to be generated from a small data set in the future, the truth model should be further refined and validated from both single-wheel testbed studies in snow and from *in situ* testing. Ultimately, the results from this study show that the IDeA is a simple, robust, and reliable method for detecting incipient immobilization of a rover operating in snow.

# Chapter 8

## Conclusion

This thesis describes three key advancements in enabling autonomous ground traverses of the Earth’s polar regions. The improvements developed are not just theoretical in nature but have real-world applications in expanding data collection and data processing capabilities in the Arctic and in Antarctica.

The first technology is a faster, more accurate, and higher resolution isochrone tracing algorithm for use with ground penetrating radar (GPR) data. The method outlined in Ch. 2 utilizes an average square difference function to track the signature of an internal reflection horizon in one sample to an adjacent sample. With such a low computational cost, this process can then be repeated for thousands of samples and multiple layers resulting in much faster and more detailed layer following than the typical method of manual tracing. This algorithm was not only proven on the large GPR data set collected from the Green-TrACS campaign but has also been packaged into a user-friendly application that can be immediately employed by other researchers on their own data. Automating layer picking over large distances will help save time and improve accuracy and is a necessary tool to efficiently process the vast amount of data that can be collected by autonomous rovers.

The second contribution is a new methodology for designing or modifying tractive elements to increase mobility in snow. Existing terramechanics theory provides a useful

framework in guiding the design of wheels for improved traction on deformable terrain. However, it is shown that limiting the scope to single-wheel studies neglects the impact of wheel changes on other key factors of a mobile robot system. Instead, this work demonstrates the importance of analyzing how altering a wheel’s dimensions affects the needed output torque and resultant sinkage and how this translates to drawbar pull and mobility efficiency. This design approach was put to the test in the exact scenario for which it was intended, as a prototype snow rover with the new wheels collected GPR data on the Greenland ice sheet, driving tens of kilometers with no immobilizations.

The final development is in utilizing studies of vehicle dynamics due to variation in terrain properties to assess real-time mobility. While optimization of wheel geometry allows for the rover to traverse a much wider range of snow types, terrains outside that range, which are known to cause immobilizations, are still likely to be encountered when traversing an ice sheet. There is also a gap in the literature on understanding and modeling the dynamics of a vehicle preceding a loss of mobility that result from its interaction with variable terrain. For a four-wheeled robot, this behavior cannot be assessed through single-wheel studies, seeing as the geometry, degrees of freedom, and control scheme of the rover all play a role in its performance. Therefore, *in situ* immobilization tests with an instrumented prototype operating on low stiffness, poorly bonded snow were performed to gather data on these effects and to expand on existing terramechanics models by including rover dynamics.

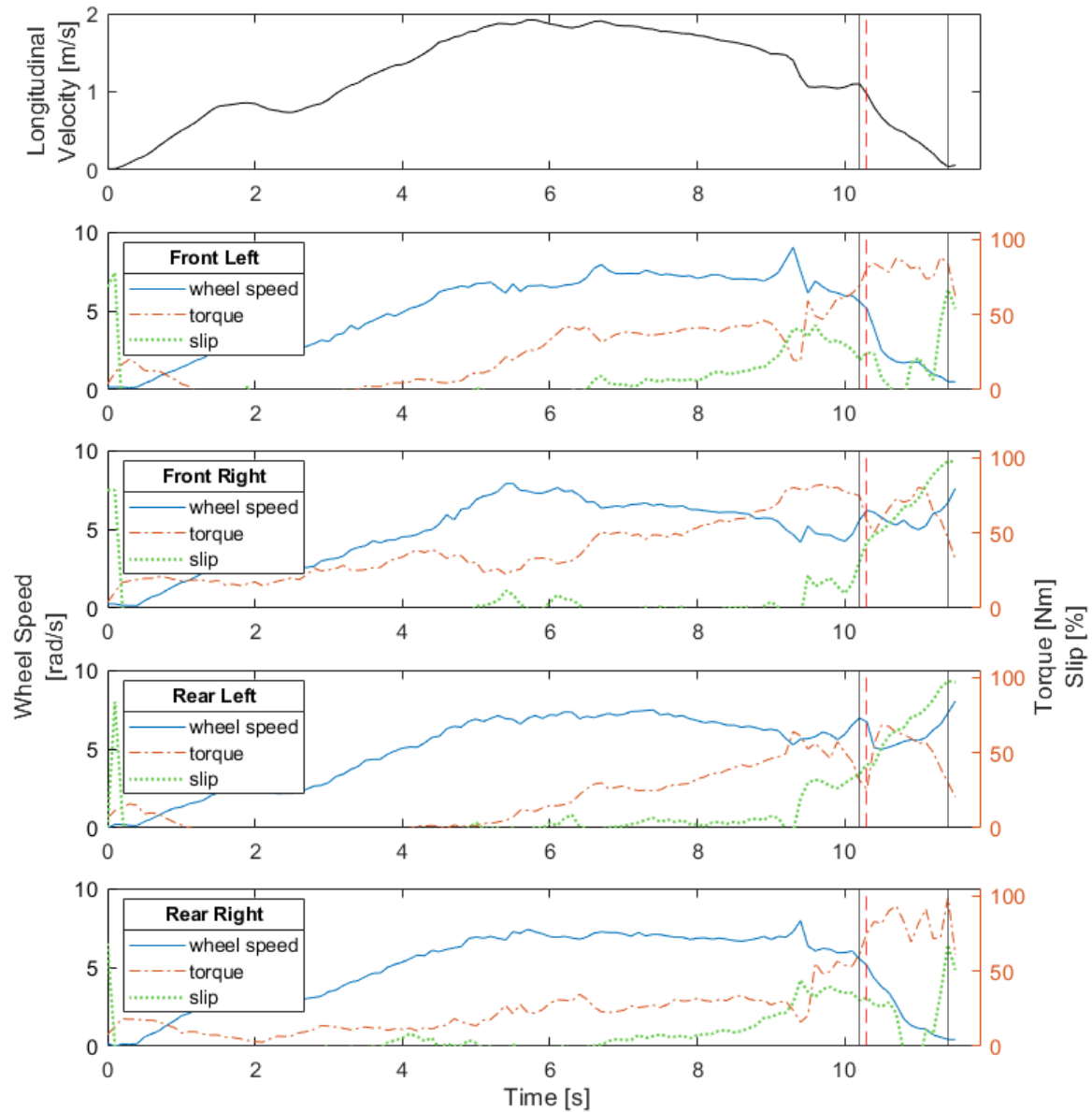
From the real and simulated data of the rover becoming immobilized, a multiple model estimation (MME) algorithm was developed that can detect immobilizing terrain underfoot by recognizing a change in the wheel motors’ operating points. This algorithm is proven to warn of an imminent loss of traction for event data collected with *FrostyBoy* and runs fast enough to be capable of real-time implementation. This algorithm’s performance is also demonstrated on simulated rover immobilizations, allowing for exploration of potential design changes and control architectures to limit its susceptibility to varying terrain. It also

opens up possibilities for how the robot would then be able to avoid immobilization once alerted of its diminished mobility, whether this involves simply releasing a towed load on a winch, backing up to find a new path, or initiating a more complex control scheme for the four wheels. Regardless, early detection is the first step in preventing rovers from becoming immobilized in patches of compressible, low cohesion snow and the MME algorithm has proven effective and reliable in this role. While there is still significant opportunity for further *in situ* testing to create and validate models of vehicle system-terrain interaction, this thesis shows the practical applications of this research.

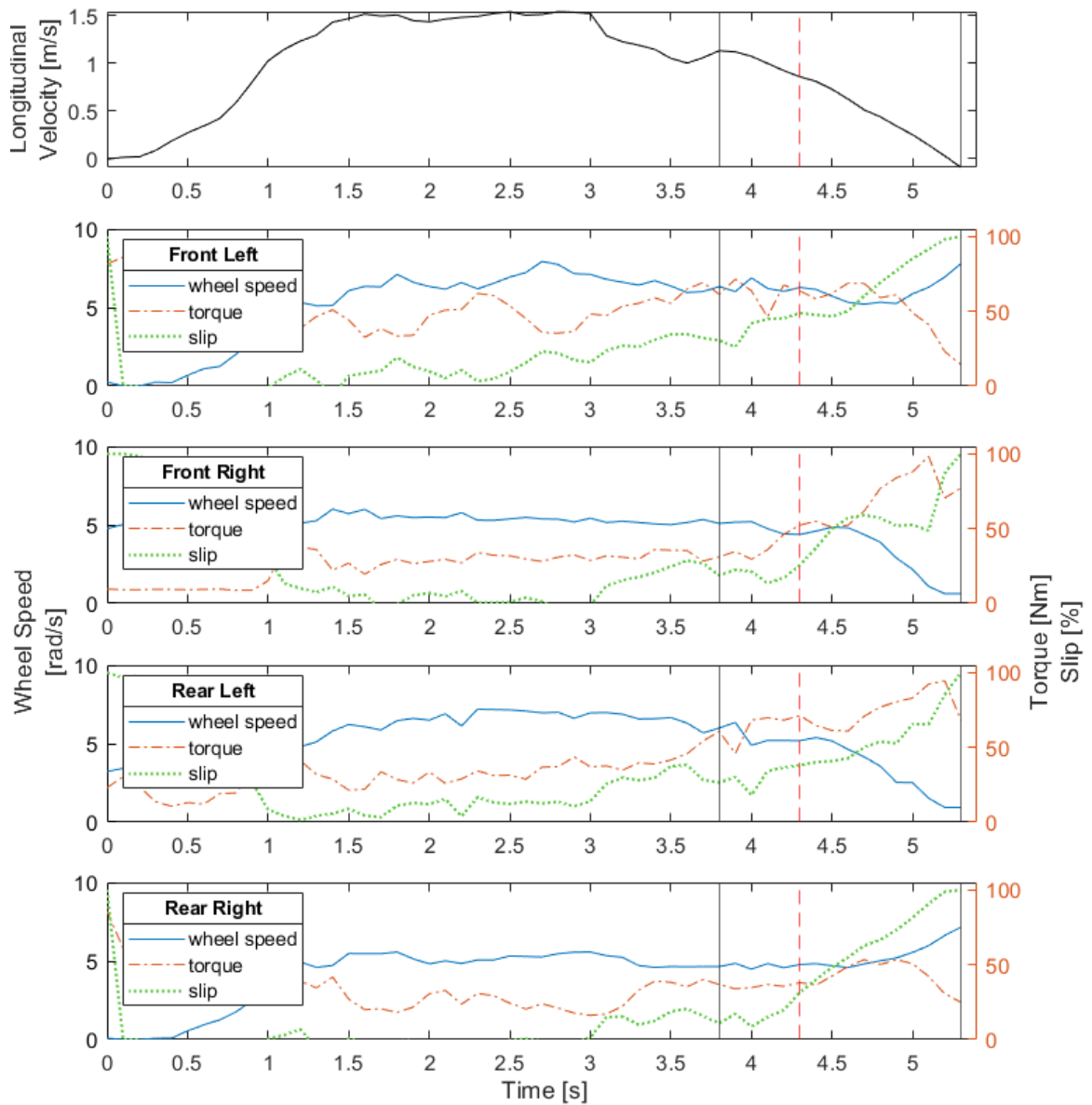
## **Appendix A**

### **Detection Results - Collected Data**

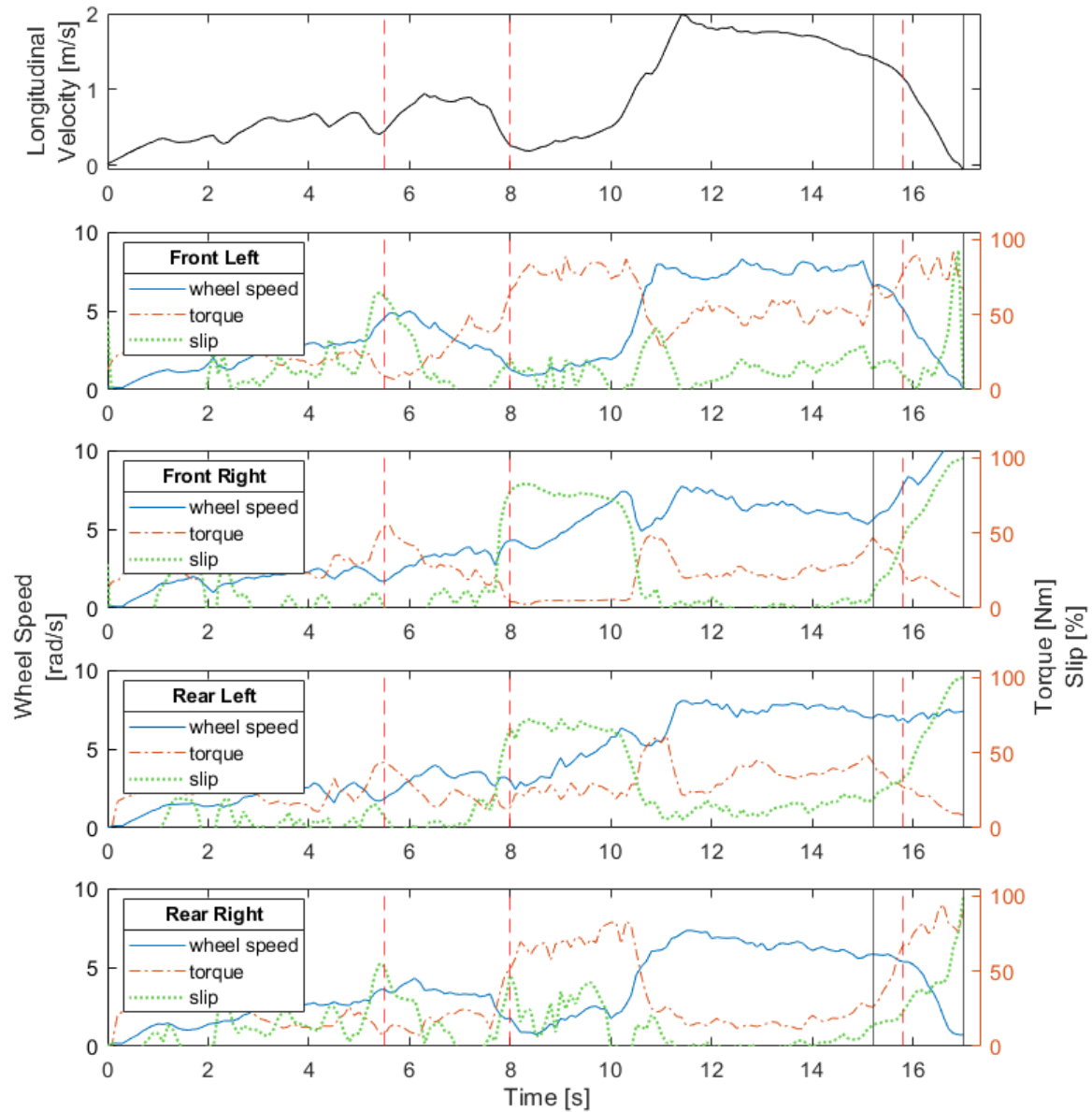
## A.1 Event 1-1



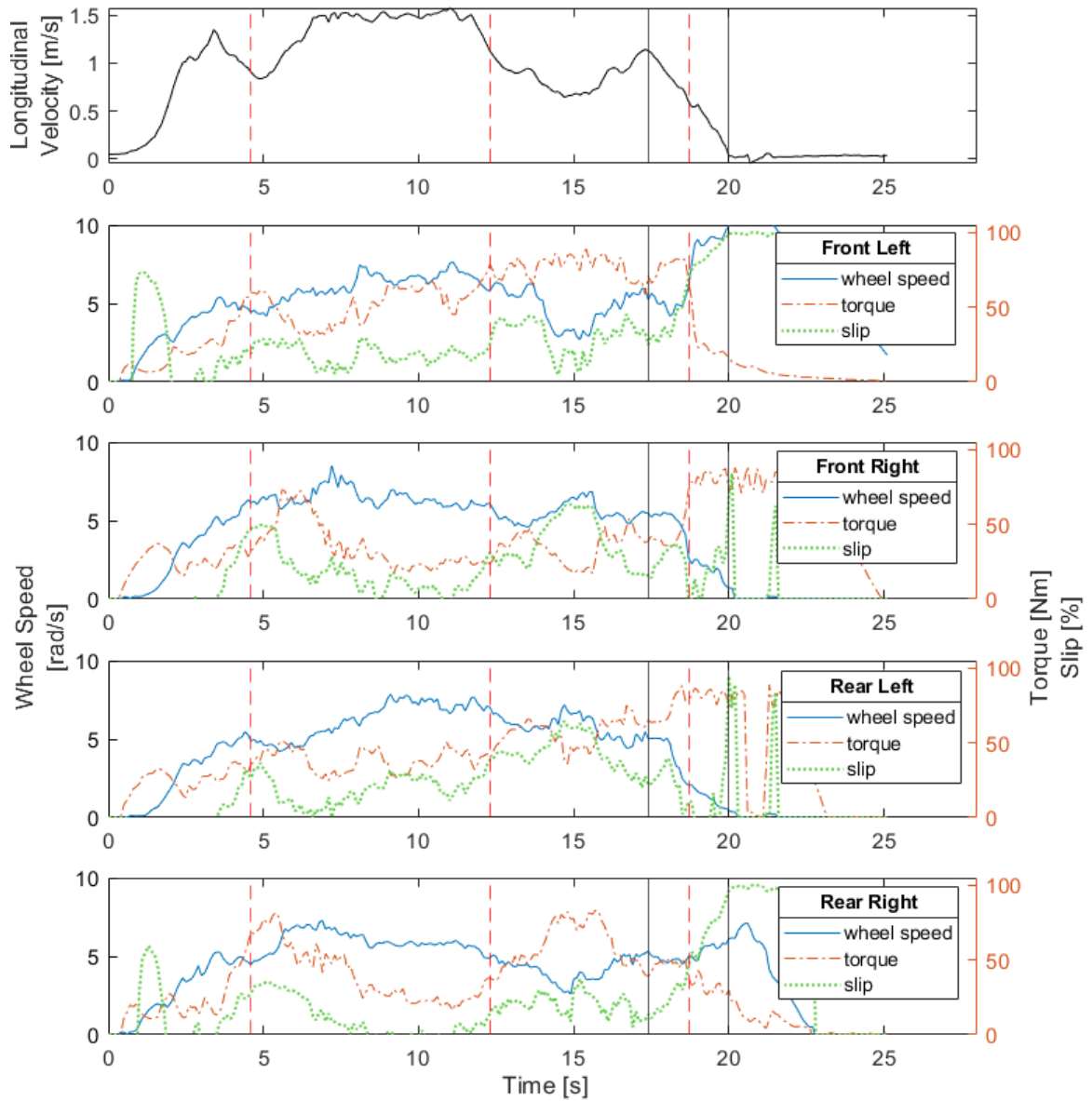
## A.2 Event 1-2



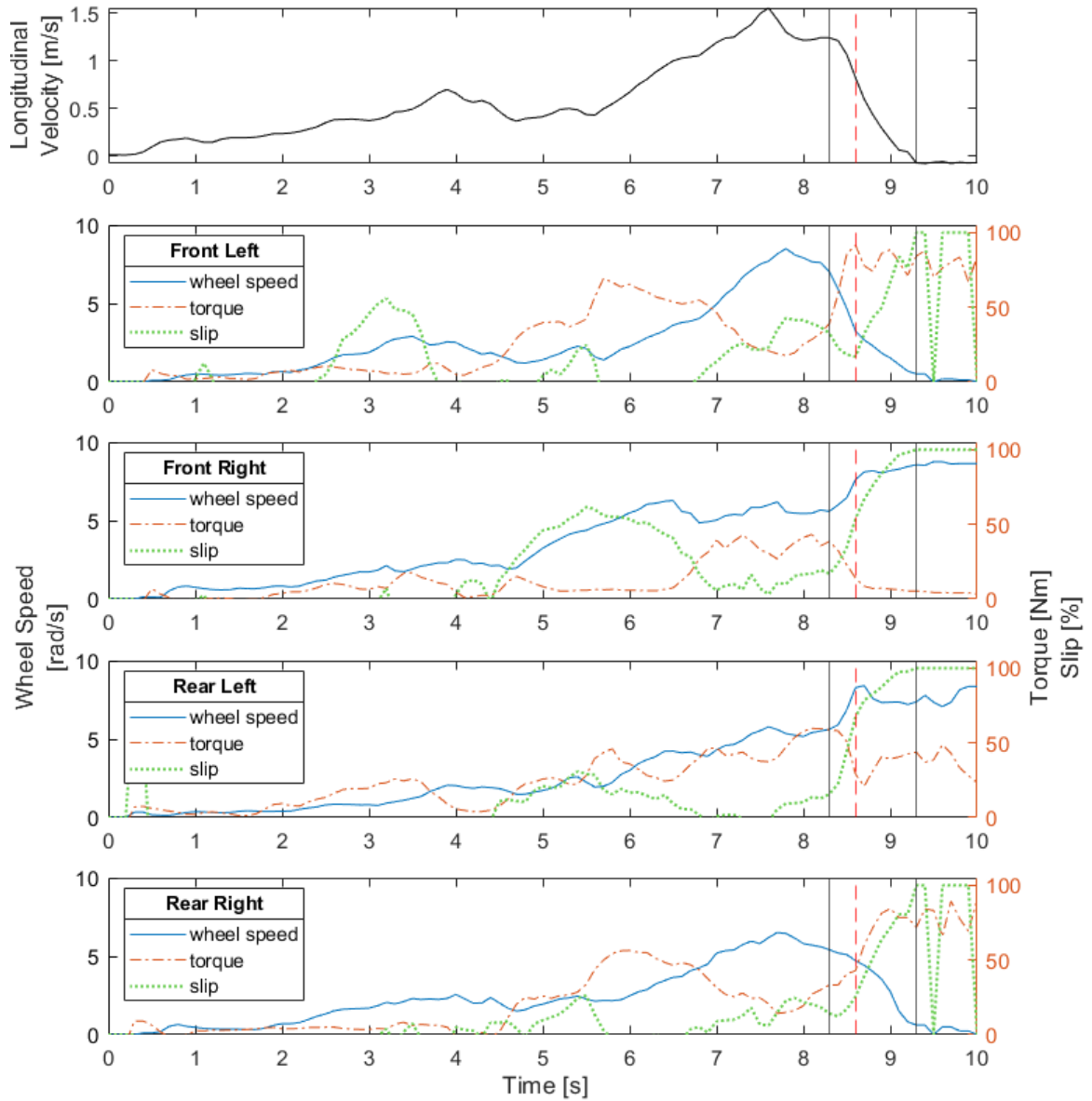
### A.3 Event 1-3



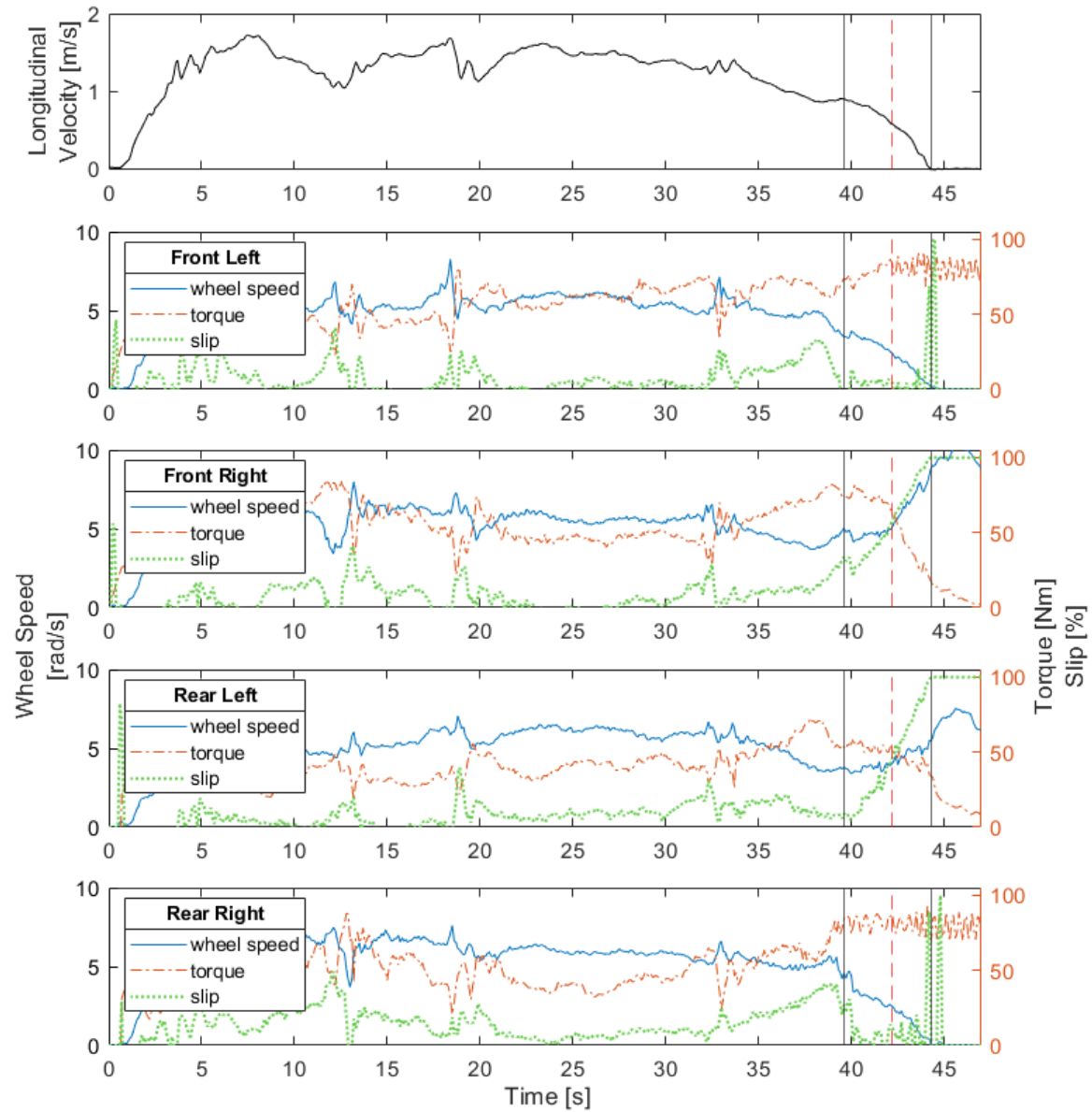
## A.4 Event 1-4



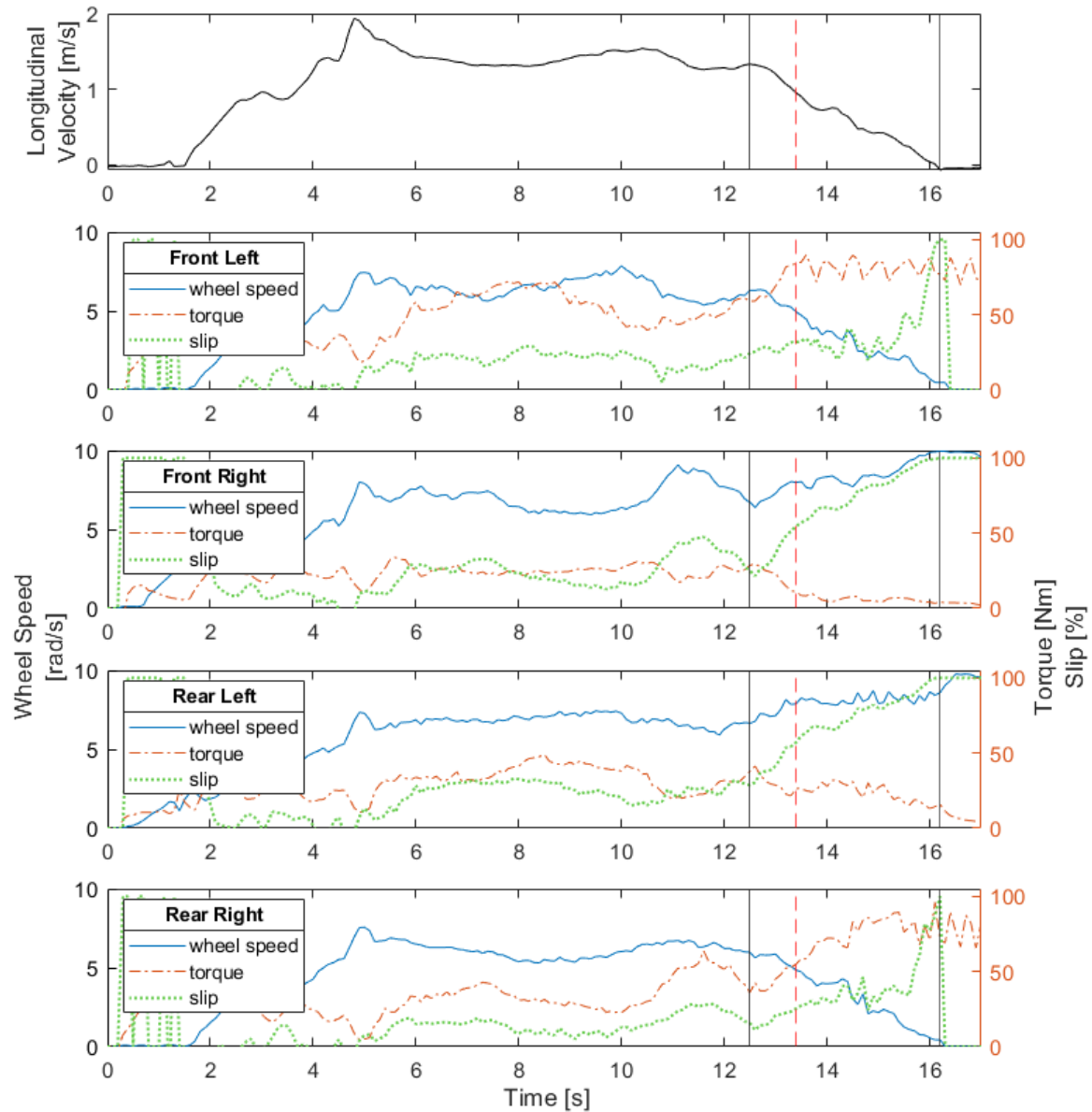
## A.5 Event 1-5



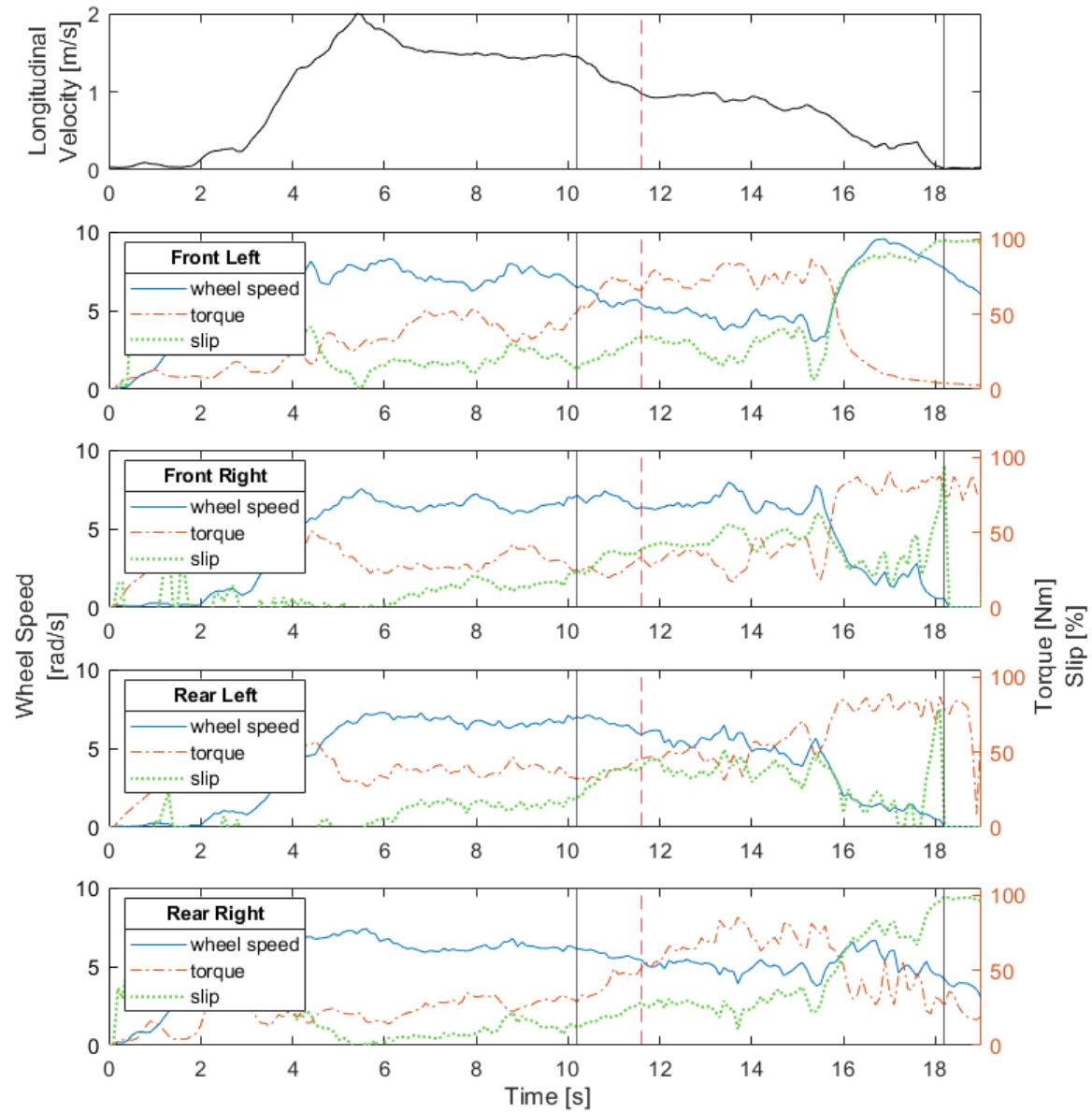
## A.6 Event 1-6



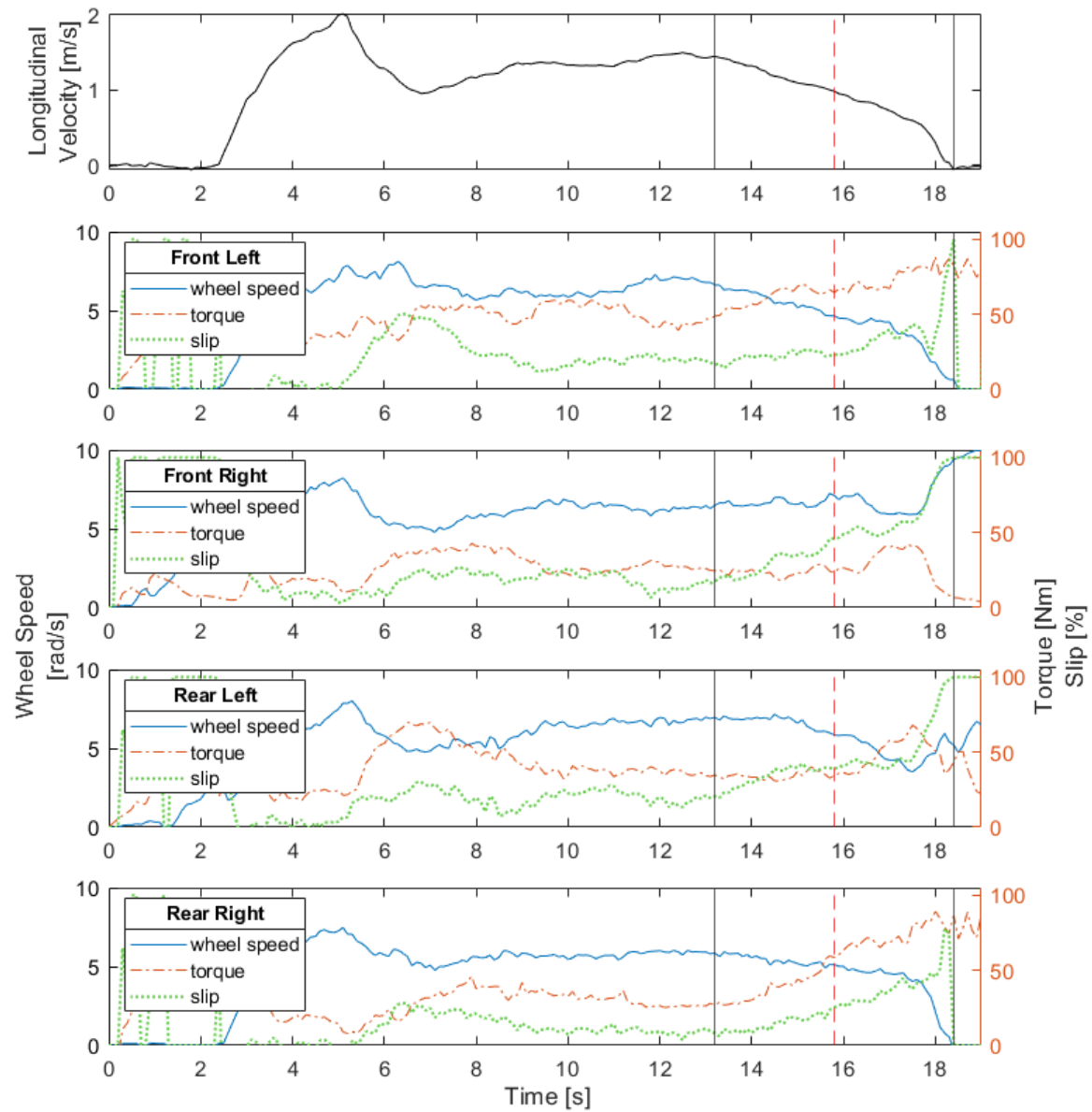
## A.7 Event 1-7



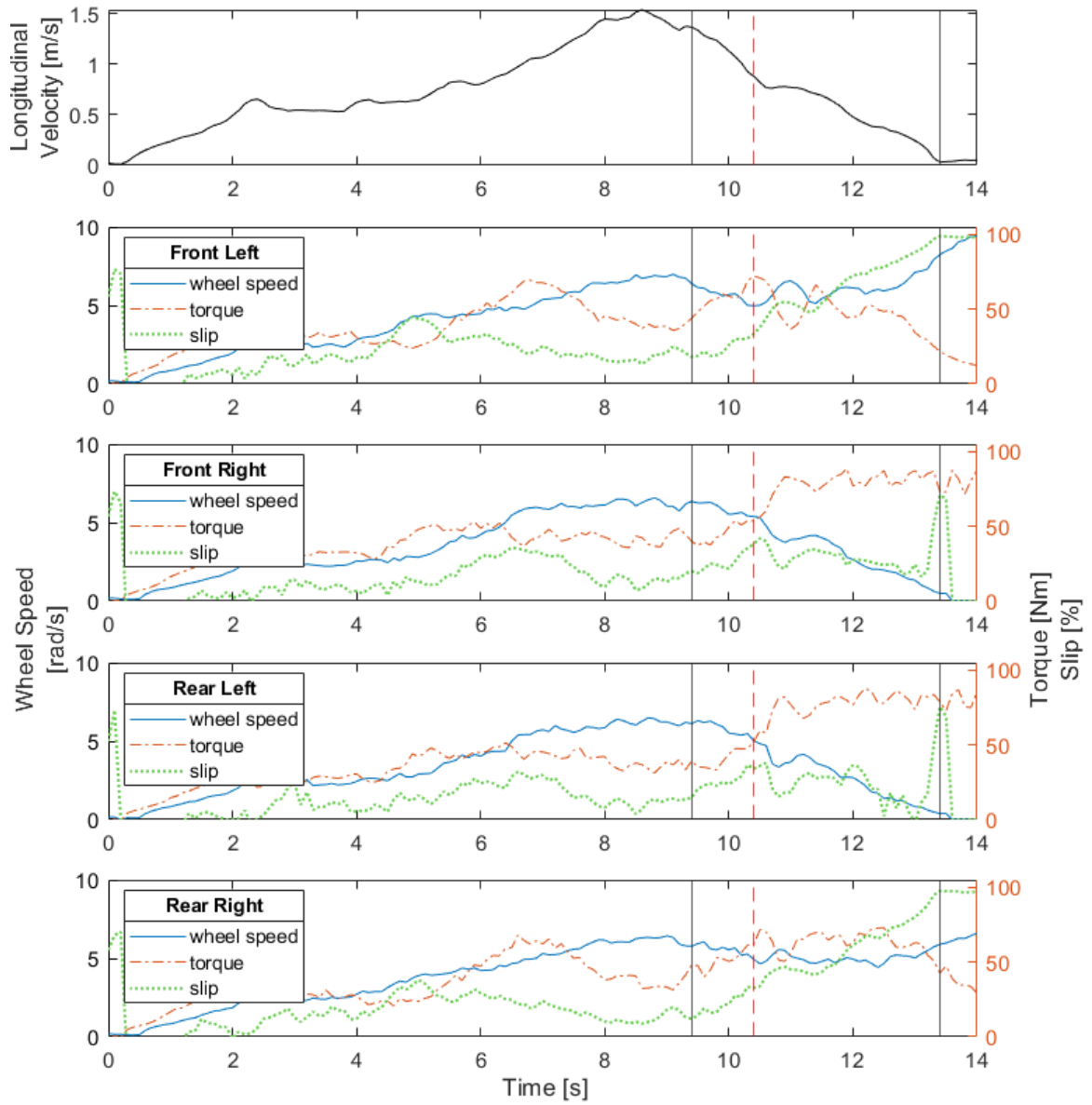
## A.8 Event 1-8



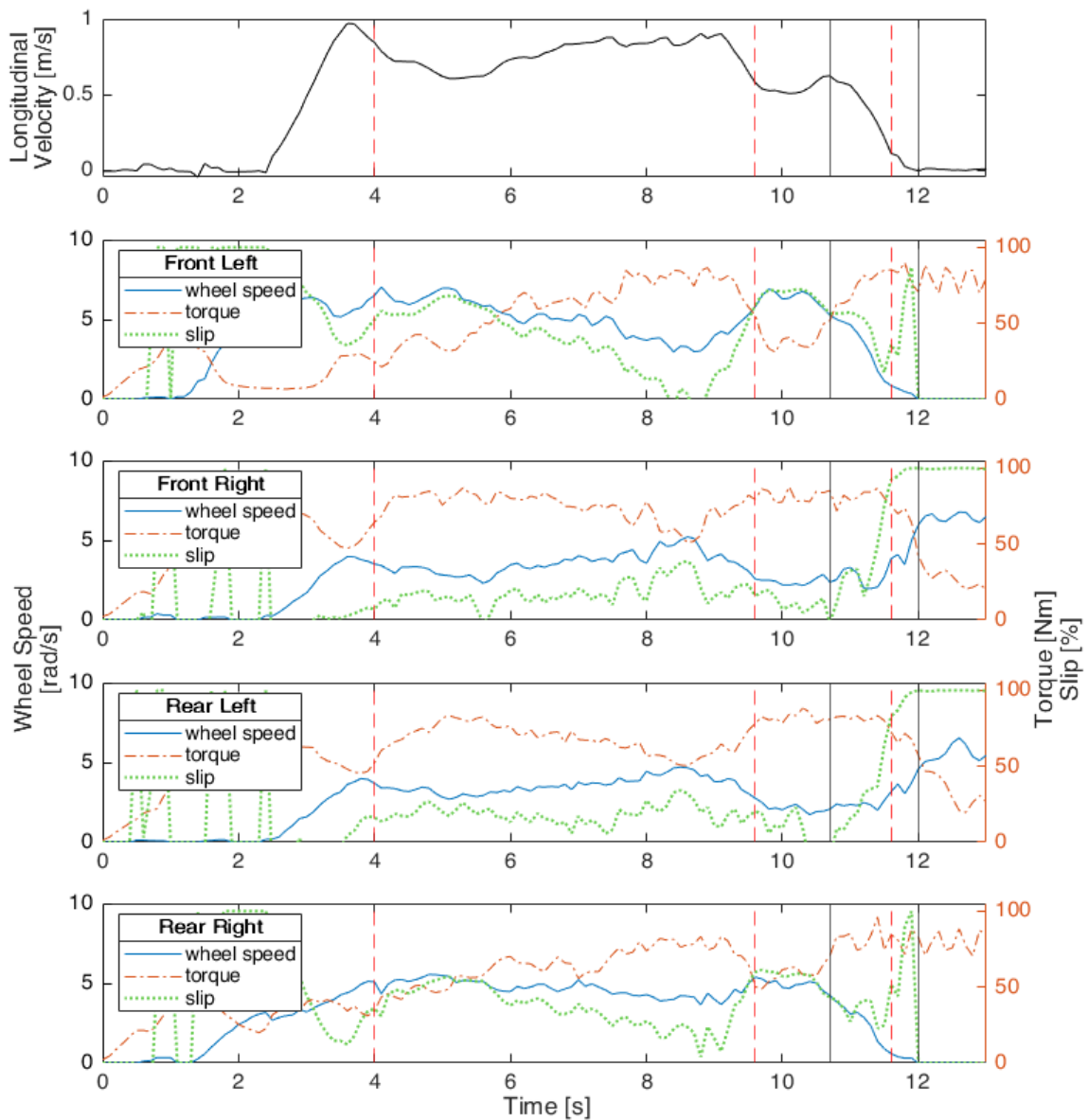
## A.9 Event 1-9



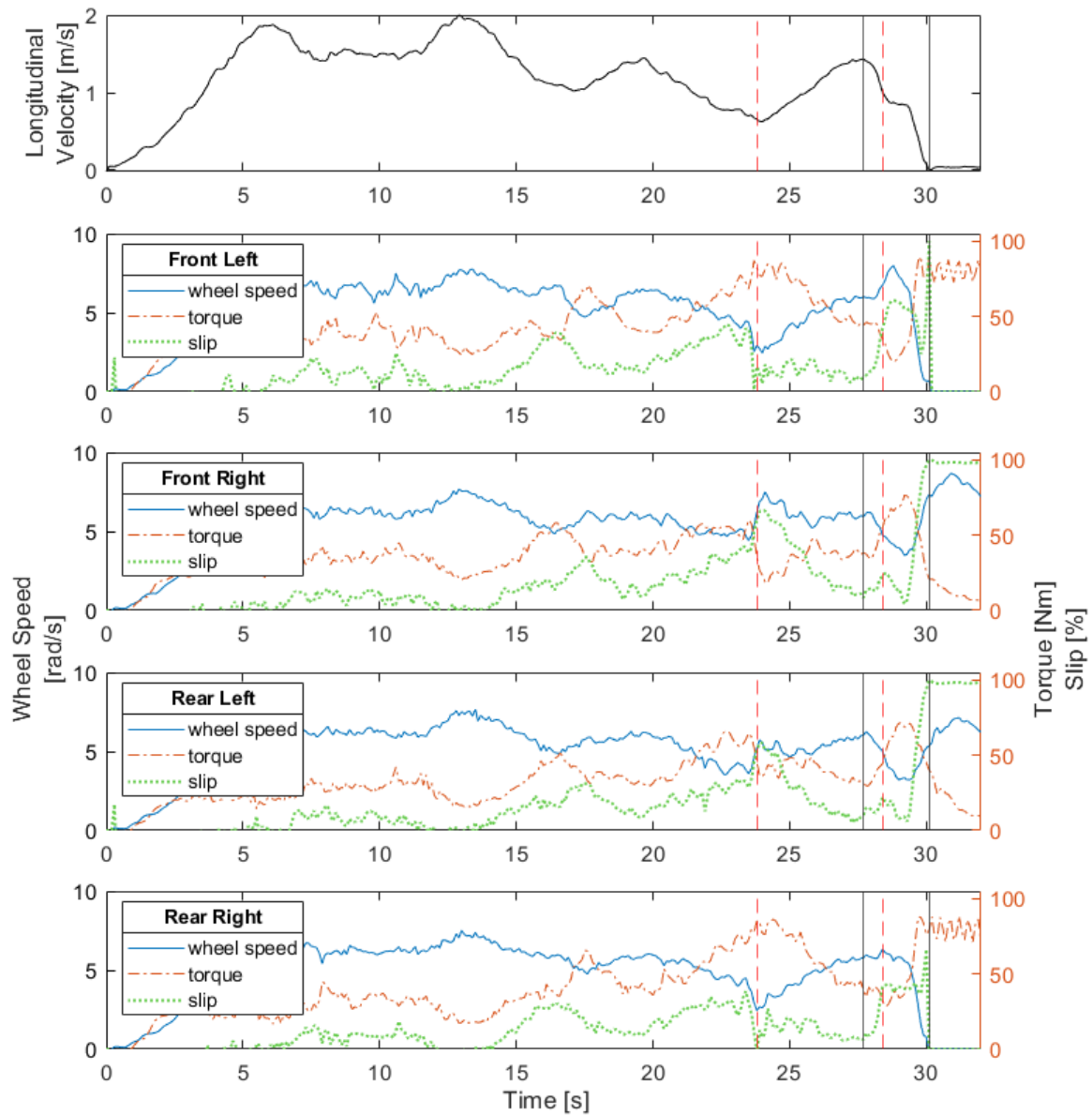
## A.10 Event 2-1



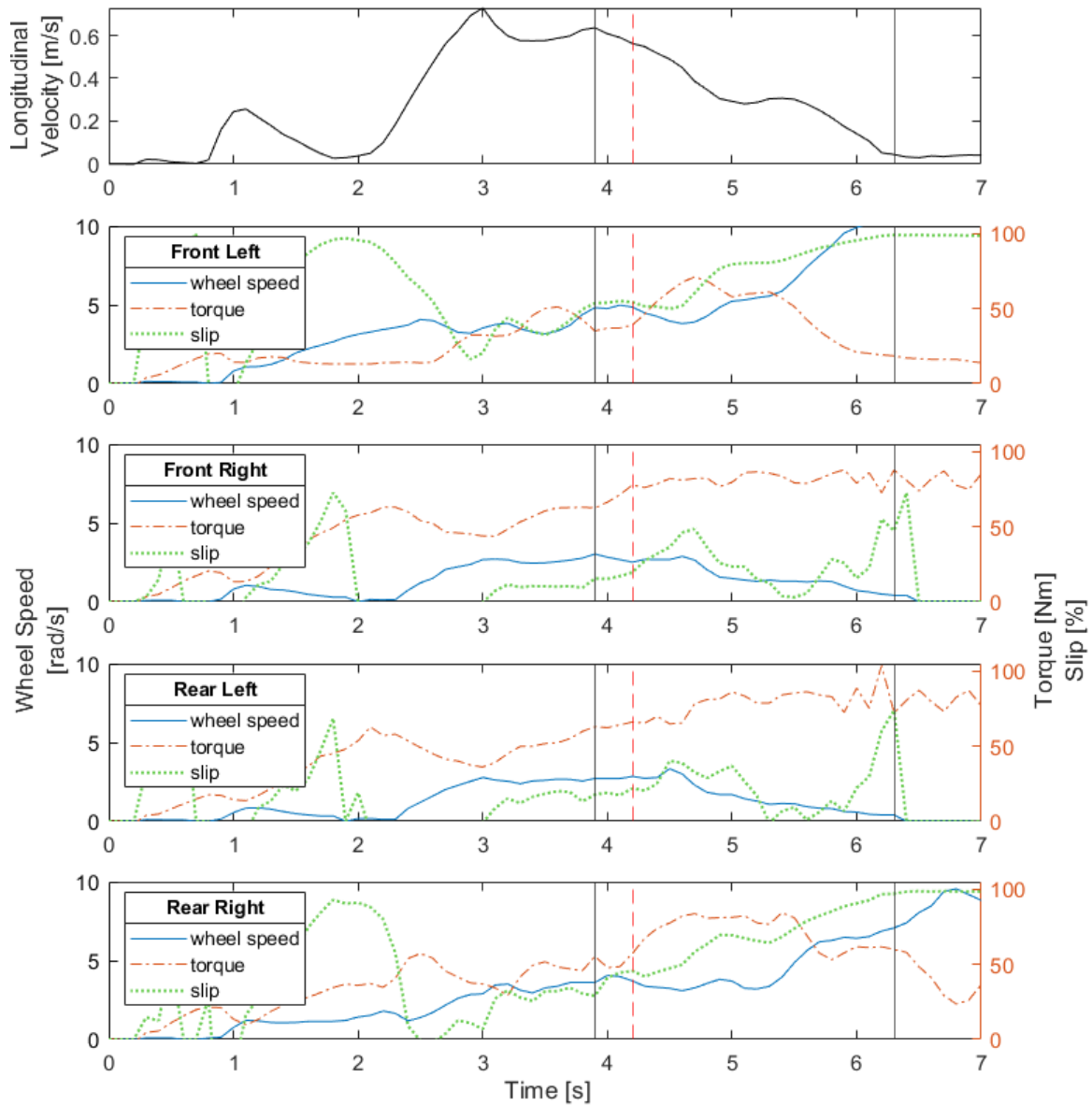
## A.11 Event 2-2



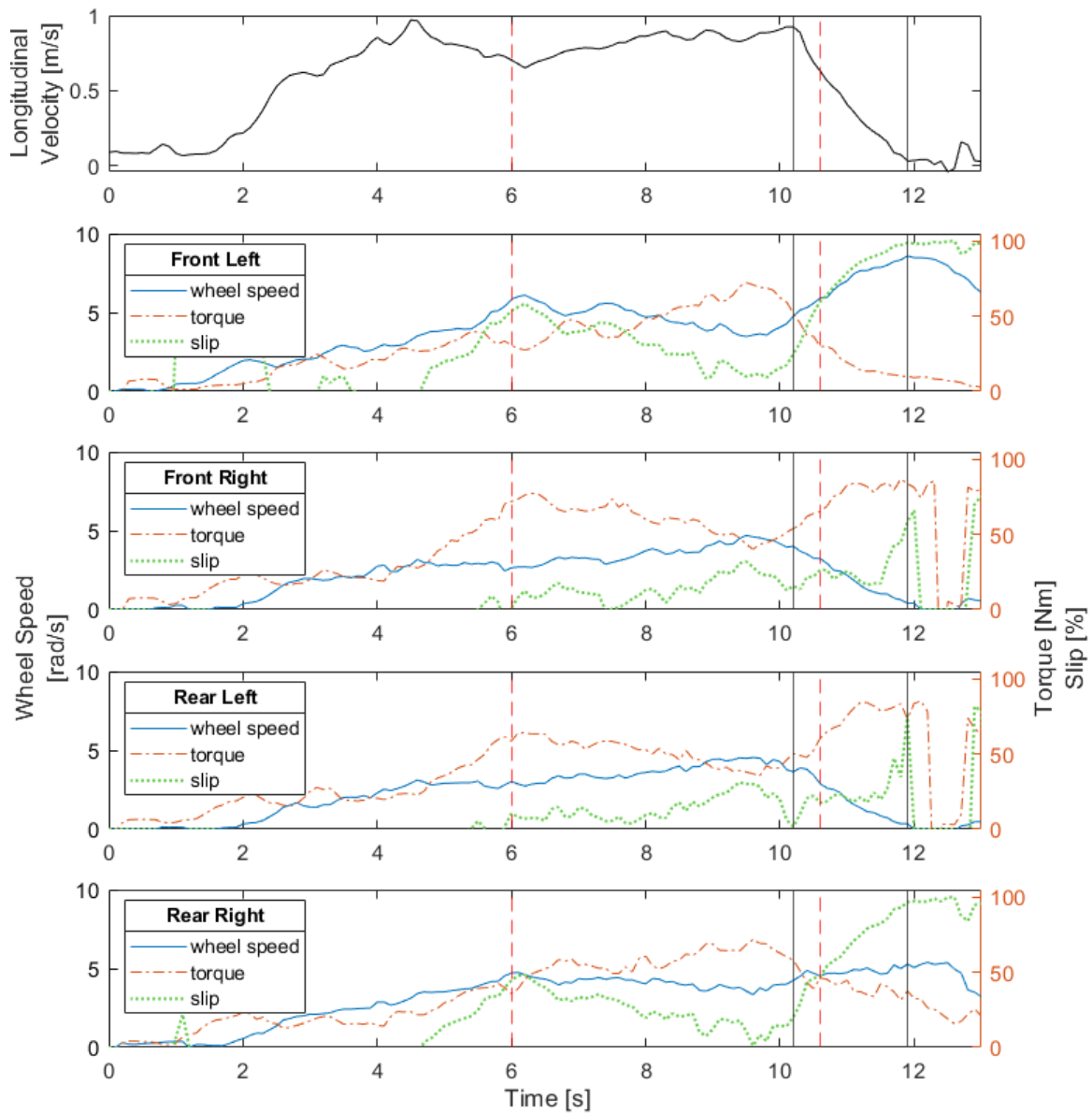
## A.12 Event 2-3



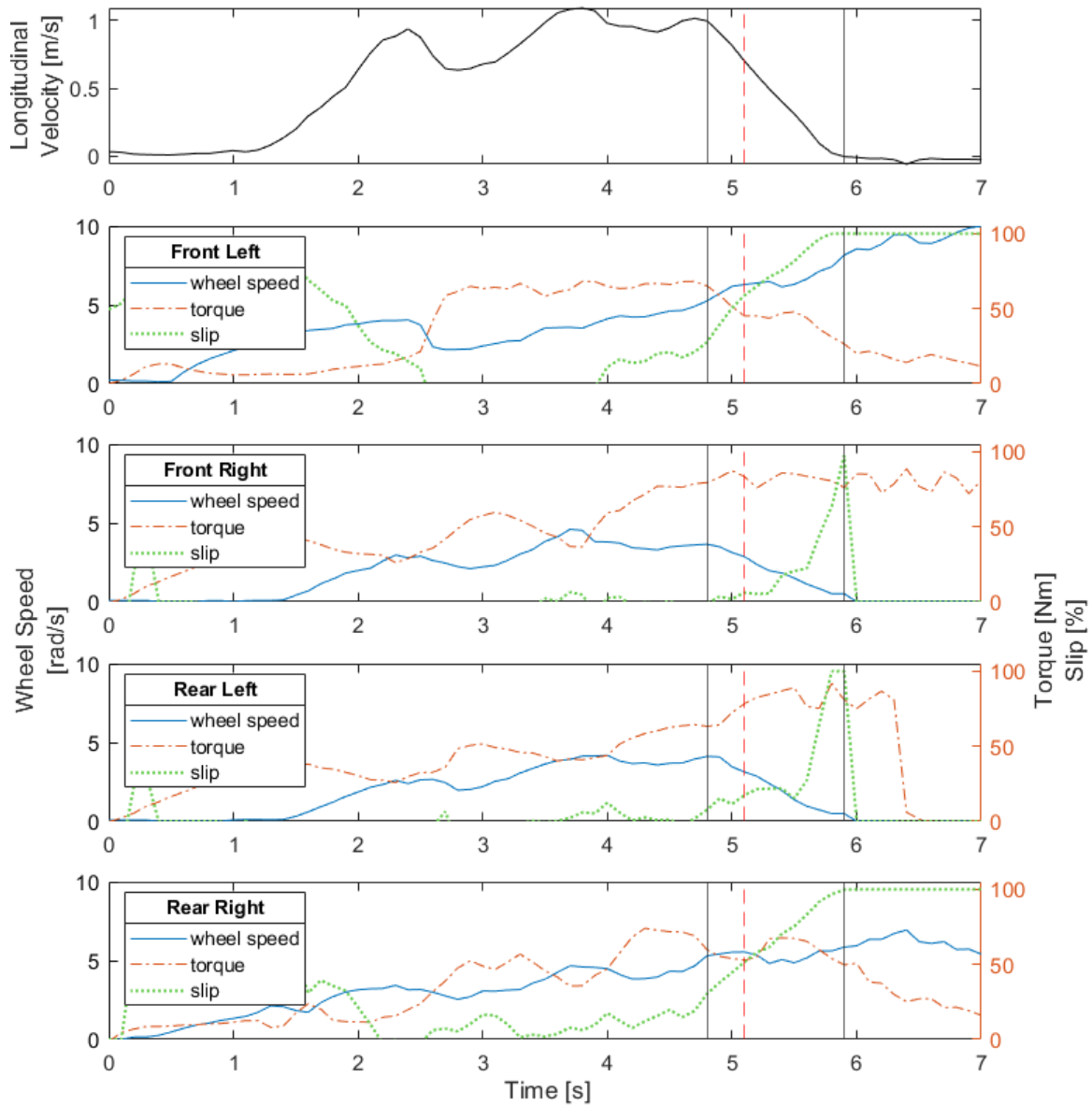
## A.13 Event 2-4



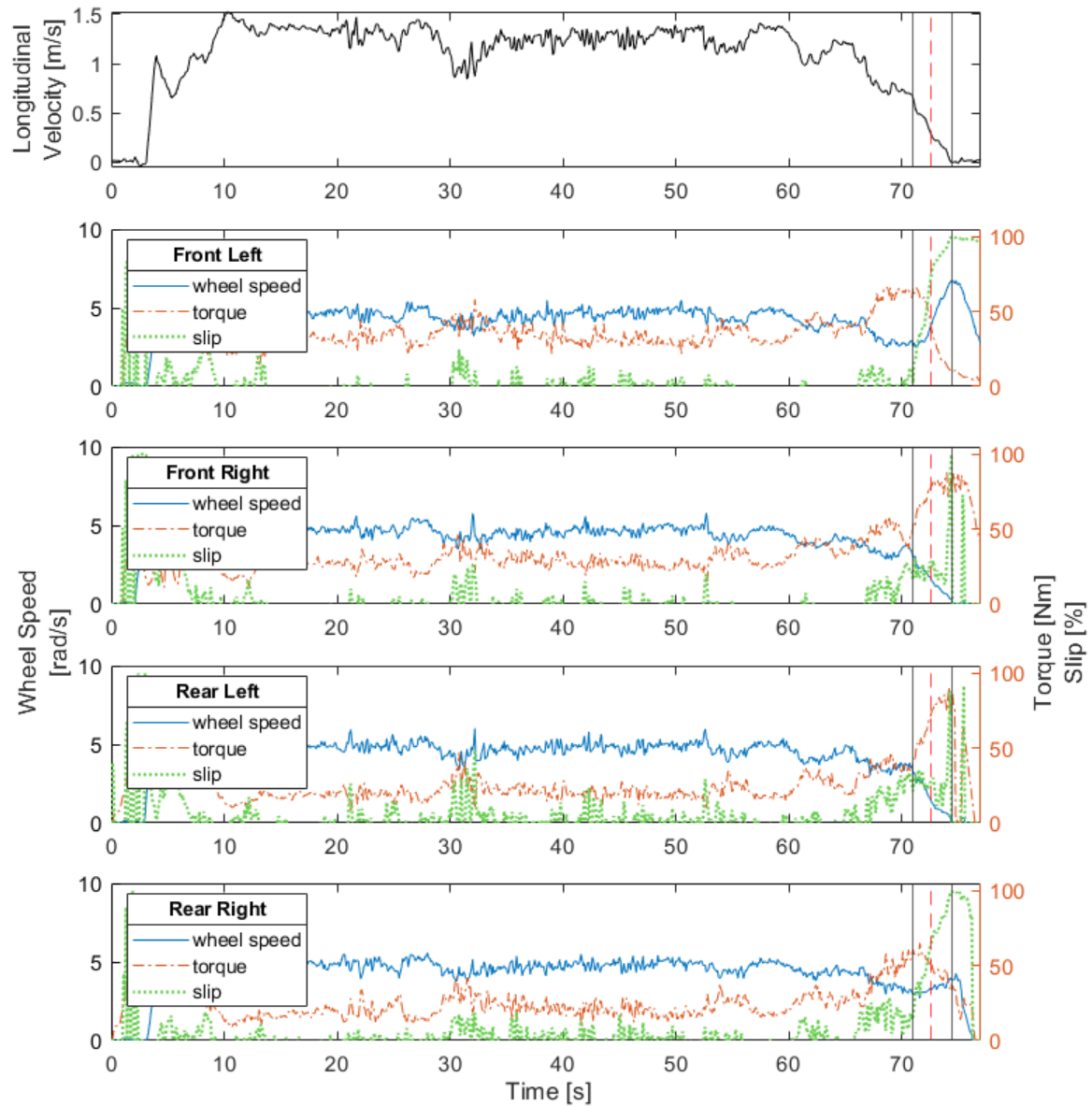
## A.14 Event 2-5



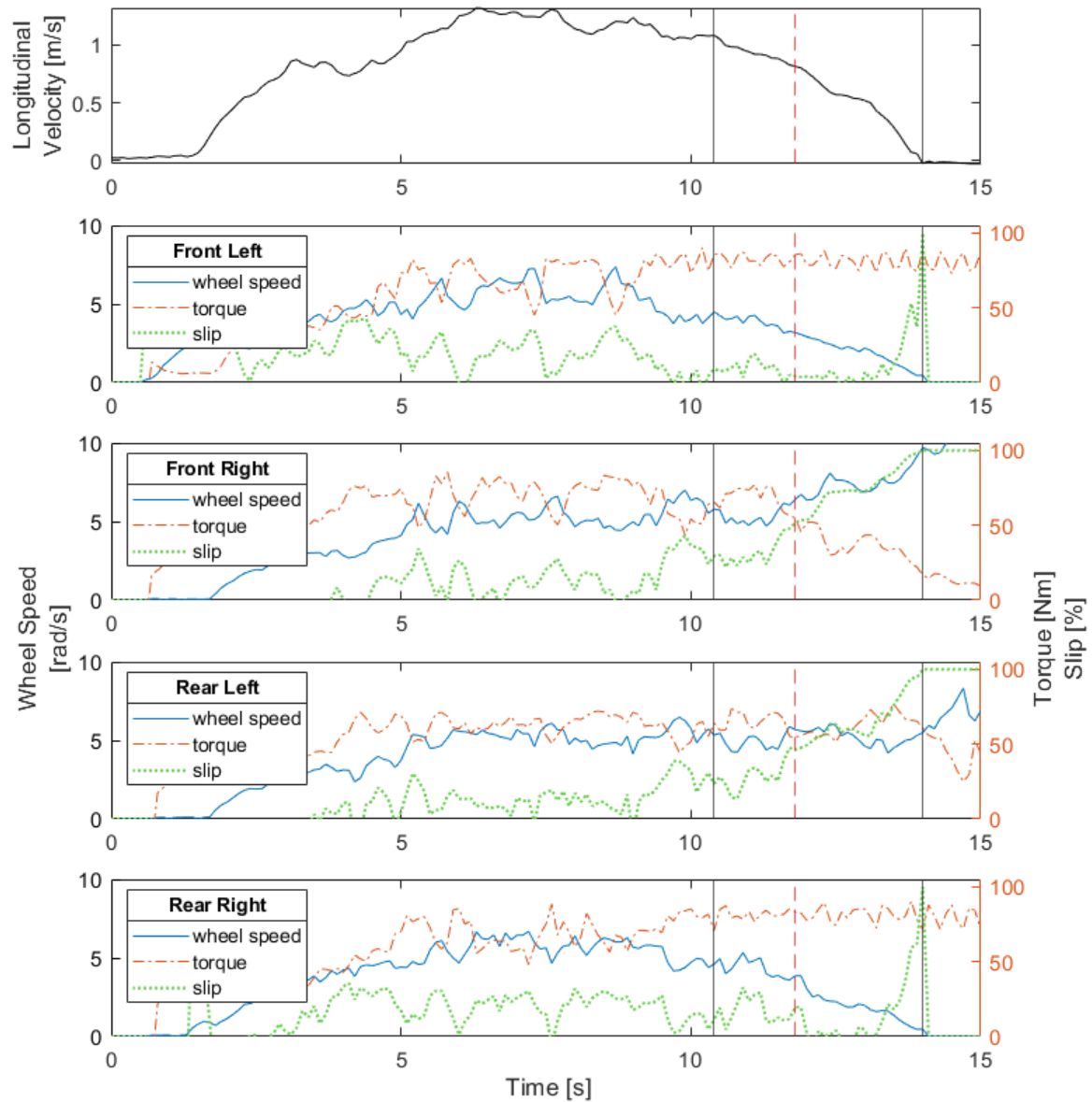
## A.15 Event 2-6



## A.16 Event 2-7



## A.17 Event 2-8



## **Appendix B**

### **Code Repository on GitHub**

The code discussed in this thesis can be found at the GitHub online code repository at:

<https://github.com/austinlines/PhD>

Within this repository, there are descriptive folder names for each collection of files and within each folder, a README.md file that serves as a guide to the uploaded code. All code is publicly available.

# Bibliography

- [1] A. Lines, J. Elliott, G. Lewis, and L. Ray, “Hybrid GPR layer picking method using average square difference function,” in *International Geoscience and Remote Sensing Symposium (IGARSS)*, Yokohama, Japan, Jul. 2019, pp. 3606–3609.
- [2] J. Y. Wong, *Theory of Ground Vehicles*, 3rd ed. New York, NY, USA: John Wiley and Sons, Inc., 2001.
- [3] W. L. Harrison, “Vehicle Performance Over Snow - Math-Model Validation Study.” Cold Regions Research and Engineering Laboratory, Tech. Rep. 268, 1975.
- [4] J. Y. Wong and J. Preston-Thomas, “On the characterization of the pressure-sinkage relationship of snow covers containing an ice layer,” *Journal of Terramechanics*, vol. 20, no. 1, pp. 1–12, 1983.
- [5] J. H. Lever, “Over-snow rolling resistance of wheeled vehicles,” in *International Society for Terrain-Vehicle Systems*, Fairbanks, Alaska, 2007.
- [6] L. E. Ray, “Estimation of terrain forces and parameters for rigid-wheeled vehicles,” *IEEE Transactions on Robotics*, vol. 25, no. 3, pp. 717–726, 2009.
- [7] L. Ding, H. B. Gao, Z. Q. Deng, and J. G. Tao, “Wheel slip-sinkage and its prediction model of lunar rover,” *Journal of Central South University of Technology (English Edition)*, vol. 17, no. 1, pp. 129–135, feb 2010.
- [8] E. Rignot, J. Mouginot, B. Scheuchl, M. van den Broeke, M. J. van Wessem, and M. Morlighem, “Four decades of Antarctic Ice Sheet mass balance from 1979–2017,” *Proceedings of the National Academy of Sciences of the United States of America*, vol. 116, no. 4, pp. 1095–1103, jan 2019.
- [9] A. Shepherd *et al.*, “Mass balance of the Greenland Ice Sheet from 1992–2018,” *Nature*, vol. 579, no. 7798, pp. 233–239, 2020.
- [10] K. M. Brunt *et al.*, “Assessment of NASA airborne laser altimetry data using ground-based GPS data near Summit Station, Greenland,” *Cryosphere*, vol. 11, no. 2, pp. 681–692, 2017.
- [11] J. A. MacGregor, M. A. Fahnestock, G. A. Catania, J. D. Paden, S. P. Gogineni, S. K. Young, S. C. Rybarski, A. N. Mabrey, B. M. Wagman, and M. Morlighem, “Radiosтратigraphy and age structure of the Greenland Ice Sheet,” *Journal of Geophysical Research: Earth Surface*, vol. 120, pp. 212–241, 2015.

- [12] K. M. Brunt, T. A. Neumann, and C. F. Larsen, "Assessment of altimetry using ground-based GPS data from the 88S Traverse, Antarctica, in support of ICESat-2," *Cryosphere*, vol. 13, no. 2, pp. 579–590, 2019.
- [13] G. Lewis, E. Osterberg, R. Hawley, B. Whitmore, H. P. Marshall, and J. Box, "Regional Greenland accumulation variability from Operation IceBridge airborne accumulation radar," *Cryosphere*, vol. 11, no. 2, pp. 773–788, 2017.
- [14] G. Lewis, E. Osterberg, R. Hawley, H. P. Marshall, T. Meehan, K. Graeter, F. McCarthy, T. Overly, Z. Thundercloud, and D. Ferris, "Recent precipitation decrease across the western greenland ice sheet percolation zone," *The Cryosphere Discussions*, vol. 2011, pp. 1–32, 2019.
- [15] L. Ray, A. Adolph, A. Morlock, B. Walker, M. Albert, J. H. Lever, and J. Dibb, "Autonomous rover for polar science support and remote sensing," in *International Geoscience and Remote Sensing Symposium (IGARSS)*, 2014, pp. 4101–4104.
- [16] L. E. Ray, J. H. Lever, A. D. Streeter, and A. D. Price, "Design and power management of a solar-powered "Cool Robot" for polar instrument networks," *Journal of Field Robotics*, vol. 24, no. 7, pp. 581–599, 2007. [Online]. Available: <http://onlinelibrary.wiley.com/doi/10.1002/rob.21514/abstract>
- [17] E. Trautmann, L. Ray, and J. Lever, "Development of an autonomous robot for ground penetrating radar surveys of polar ice," in *IEEE/RSJ International Conference on Intelligent Robots and Systems*. St. Louis, MO, USA: IEEE, Oct. 2009, pp. 1685–1690.
- [18] L. Ray, A. Adolph, A. Morlock, B. Walker, M. Albert, J. H. Lever, and J. Dibb, "Autonomous rover for polar science support and remote sensing," in *International Geoscience and Remote Sensing Symposium (IGARSS)*. IEEE, Jul. 2014, pp. 4101–4104.
- [19] A. Lines, "PhD, GitHub Repository," <https://github.com/austinlines/PhD>, *Created:* 2020-11-06.
- [20] S. A. Arcone, G. S. Hamilton, V. B. Spikes, and P. A. Mayewski, "Stratigraphic continuity in 400 Mhz short-pulse radar profiles of firn in west Antarctica," *Annals of Glaciology*, vol. 39, pp. 195–200, 2004.
- [21] R. L. Hawley, Z. R. Courville, L. M. Kehrl, E. R. Lutz, E. C. Osterberg, T. B. Overly, and G. J. Wong, "Recent accumulation variability in northwest Greenland from ground-penetrating radar and shallow cores along the Greenland Inland Traverse," *Journal of Glaciology*, vol. 60, no. 220, pp. 375–382, July 2014.
- [22] B. Medley, I. Joughin, S. B. Das, E. J. Steig, H. Conway, S. Gogineni, A. S. Criscitiello, J. R. McConnell, B. E. Smith, M. R. Van Den Broeke, J. T. M. Lenaerts, D. H. Bromwich, and J. P. Nicolas, "Airborne-radar and ice-core observations of annual snow accumulation over Thwaites Glacier, West Antarctica confirm the spatiotemporal variability of global and regional atmospheric models," *Geophysical Research Letters*, vol. 40, no. 14, pp. 3649–3654, 2013.

- [23] N. C. Kruetzmann, W. Rack, A. J. McDonald, and S. E. George, “Snow accumulation and compaction derived from GPR data near Ross Island, Antarctica,” *The Cryosphere*, vol. 5, pp. 391–404, 2011.
- [24] H. Conway, B. L. Hall, G. H. Denton, A. M. Gades, and E. D. Waddington, “Past and future grounding-line retreat of the West Antarctic Ice Sheet,” *Science*, vol. 286, no. 5438, pp. 280–283, Oct. 1999.
- [25] L. C. Sime, R. C. Hindmarsh, and H. Corr, “Instruments and Methods Automated processing to derive dip angles of englacial radar reflectors in ice sheets,” *Journal of Glaciology*, vol. 57, no. 202, pp. 260–266, 2011.
- [26] M. Fahnestock, W. Abdalati, S. Luo, and S. Gogineni, “Internal layer tracing and age-depth-accumulation relationships for the northern Greenland ice sheet,” *Journal of Geophysical Research Atmospheres*, vol. 106, no. D24, pp. 33 789–33 797, 2001.
- [27] M. Dossi, E. Forte, and M. Pipan, “Automated reflection picking and polarity assessment through attribute analysis: Theory and application to synthetic and real ground-penetrating radar data,” *GEOPHYSICS*, vol. 80, no. 5, pp. H23–H35, 2015.
- [28] V. D. P. Onana, L. S. Koenig, J. Ruth, M. Studinger, and J. P. Harbeck, “A semiautomated multilayer picking algorithm for ice-sheet radar echograms applied to ground-based near-surface data,” *IEEE Transactions on Geoscience and Remote Sensing*, vol. 53, no. 1, pp. 51–69, 2015.
- [29] S. Shoop, K. Kestler, and R. Haehnel, “Finite element modeling of tires on snow,” *Tire Science and Technology*, vol. 34, no. 1, pp. 2–37, 2006.
- [30] M. G. Bekker, *Theory of Land Locomotion : The Mechanics of Vehicle Mobility*. Ann Arbor, MI, USA: The University of Michigan Press, 1956.
- [31] J. Y. Wong and A. R. Reece, “Prediction of rigid wheel performance based on the analysis of soil-wheel stresses. Part I. Performance of driven rigid wheels,” *Journal of Terramechanics*, vol. 4, no. 1, pp. 81–98, 1967.
- [32] J. Y. Wong and A. R. Reece, “Prediction of rigid wheel performance based on the analysis of soil-wheel stresses. Part II. Performance of towed rigid wheels,” *Journal of Terramechanics*, vol. 4, no. 2, pp. 7–25, 1967.
- [33] C. Senatore and K. Iagnemma, “Analysis of stress distributions under lightweight wheeled vehicles,” *Journal of Terramechanics*, vol. 51, no. 1, pp. 1–17, 2014.
- [34] P. Jayakumar, D. Melanz, J. MacLennan, D. Gorsich, C. Senatore, and K. Iagnemma, “Scalability of classical terramechanics models for lightweight vehicle applications incorporating stochastic modeling and uncertainty propagation,” *Journal of Terramechanics*, vol. 54, pp. 37–57, 2014.

- [35] K. Nagatani, A. Ikeda, K. Sato, and K. Yoshida, “Accurate estimation of drawbar pull of wheeled mobile robots traversing sandy terrain using built-in force sensor array wheel,” in *2009 IEEE/RSJ International Conference on Intelligent Robots and Systems, IROS 2009*, dec 2009, pp. 2373–2378.
- [36] S. Moreland, K. Skonieczny, H. Inotsume, and D. Wettergreen, “Soil behavior of Wheels with Grousers for Planetary Rovers,” in *IEEE Aerospace Conference*, Big Sky, MT, USA, 2012.
- [37] H. Inotsume, S. Moreland, K. Skonieczny, and D. Wettergreen, “Parametric study and design guidelines for rigid wheels for planetary rovers,” *Journal of Terramechanics*, vol. 85, pp. 39–57, Oct. 2019.
- [38] G. Meirion-Griffith and M. Spenko, “A modified pressure-sinkage model for small, rigid wheels on deformable terrains,” *Journal of Terramechanics*, vol. 48, no. 2, pp. 149–155, 2011.
- [39] L. Ding, H. Gao, Z. Deng, Y. Li, and G. Liu, “New perspective on characterizing pressure-sinkage relationship of terrains for estimating interaction mechanics,” *Journal of Terramechanics*, vol. 52, no. 1, pp. 57–76, 2014.
- [40] G. Ishigami, K. Nagatani, A. Miwa, and K. Yoshida, “Terramechanics-based model for steering maneuver of planetary exploration rovers on loose soil,” *Journal of Field Robotics*, vol. 24, no. 3, pp. 233–250, 2007.
- [41] R. B. Haehnel and S. A. Shoop, “A macroscale model for low density snow subjected to rapid loading,” *Cold Regions Science and Technology*, vol. 40, no. 3, pp. 193–211, dec 2004.
- [42] R. A. Sommerfeld and E. LaChapelle, “The classification of snow,” *Journal of Glaciology*, vol. 9, no. 55, 1970.
- [43] D. Gee-Clough, “The effect of wheel width on the rolling resistance of rigid wheels in sand,” *Journal of Terramechanics*, vol. 15, no. 4, pp. 161–184, 1978.
- [44] K. Terzaghi, *Theoretical Soil Mechanics*. New York, NY, USA: John Wiley and Sons, Inc., 1943.
- [45] M. Lyasko, “Slip sinkage effect in soil-vehicle mechanics,” *Journal of Terramechanics*, vol. 47, pp. 21–31, 2009.
- [46] B. E. Wallace and N. S. Rao, “Engineering elements for transportation on the lunar surface,” *Applied Mechanics Reviews*, vol. 46, no. 6, pp. 301–312, 1993.
- [47] J. T. Cook, “Dynamics Modeling and Control of Autonomous Tractors for Polar Traverses,” Ph.D. dissertation, Thayer School of Engineering at Dartmouth College, 2017.

- [48] A. Talukder, R. Manduchi, R. Castano, K. Owens, L. Matthies, A. Castano, and R. Hogg, “Autonomous terrain characterisation and modelling for dynamic control of unmanned vehicles,” in *IEEE International Conference on Intelligent Robots and Systems*, vol. 1, 2002, pp. 708–713.
- [49] R. Manduchi, A. Castano, A. Talukder, and L. Matthies, “Obstacle detection and terrain classification for autonomous off-road navigation,” *Autonomous Robots*, vol. 18, no. 1, pp. 81–102, jan 2005.
- [50] N. Vandapel, D. F. Huber, A. Kapuria, and M. Hebert, “Natural terrain classification using 3-D lidar data,” in *Proceedings - IEEE International Conference on Robotics and Automation*. Institute of Electrical and Electronics Engineers Inc., 2004, pp. 5117–5122.
- [51] S. A. Shoop, W. L. Wieder, B. C. Elder, S. A. Beal, and E. J. Deeb, “Assessment of Field Methods for Measuring Mechanical Properties of Snow,” Cold Regions Research and Engineering Laboratory, Tech. Rep. August, 2019.
- [52] J. Y. Wong, “Expansion of the terrain input base for Nepean Tracked Vehicle Performance Model, NTVPM, to accept Swiss Ramsonde data from deep snow,” *Journal of Terramechanics*, vol. 29, no. 3, pp. 341–357, 1992.
- [53] S. Laughery, G. Gerhart, and R. Goetz, “Bekker’s terramechanics model for off-road vehicle research,” US Army TARDEC, Tech. Rep., 1999.
- [54] J. Y. Wong, *Terramechanics and Off-Road Vehicle Engineering*. Oxford: Elsevier Ltd., 2010.
- [55] J. Massah and S. Noorolahi, “Design, development and performance evaluation of a tractor-mounted bevameter,” *Soil and Tillage Research*, vol. 110, no. 1, pp. 161–166, sep 2010.
- [56] I. Shmulevich, D. Ronai, and D. Wolf, “A new field single wheel tester,” *Journal of Terramechanics*, vol. 33, no. 3, pp. 133–141, may 1996.
- [57] J. R. Matijevic, J. Crisp, D. B. Bickler, R. S. Banes, B. K. Cooper, H. J. Eisen, J. Gensler, A. Haldemann, F. Hartman, K. A. Jewett, L. H. Matthies, S. L. Laubach, A. H. Mishkin, J. C. Morrison, T. T. Nguyen, A. R. Sirota, H. W. Stone, and S. Stride, “Characterization of the martian surface deposits by the Mars Pathfinder rover, Sojourner,” *Science*, vol. 278, no. 5344, pp. 1765–1768, 1997.
- [58] J. H. Lever, D. Denton, G. E. Phetteplace, S. D. Wood, and S. A. Shoop, “Mobility of a lightweight tracked robot over deep snow,” *Journal of Terramechanics*, vol. 43, no. 4, pp. 527–551, 2006.
- [59] K. Iagnemma, S. Kang, H. Shibly, and S. Dubowsky, “Online terrain parameter estimation for wheeled mobile robots with application to planetary rovers,” *IEEE Transactions On Robotics*, vol. 20, no. 5, pp. 921–927, 2004.

- [60] L. Ojeda, J. Borenstein, and G. Witus, “Terrain trafficability characterization with a mobile robot,” in *Proceedings of the SPIE Defense and Security Conference, Unmanned Ground Vehicle Technology VII*, Orlando, FL, 2005.
- [61] Z. Liu, J. Guo, L. Ding, H. Gao, T. Guo, and Z. Deng, “Online estimation of terrain parameters and resistance force based on equivalent sinkage for planetary rovers in longitudinal skid,” *Mechanical Systems and Signal Processing*, vol. 119, pp. 39–54, mar 2019.
- [62] L. E. Ray, D. C. Brande, and J. H. Lever, “Estimation of net traction for differential-steered wheeled robots,” *Journal of Terramechanics*, vol. 46, no. 3, pp. 75–87, 2009.
- [63] E. Trautmann and L. Ray, “Mobility characterization for autonomous mobile robots using machine learning,” *Autonomous Robots*, vol. 30, no. 4, pp. 369–383, 2011.
- [64] K. D. Mankoff, D. Van As, A. Lines, T. Bording, J. Elliott, R. Kraghede, H. Cantalloube, H. Oriot, P. Dubois-Fernandez, O. Ruault Du Plessis, A. Christiansen, E. Auken, K. Hansen, W. Colgan, and N. Karlsson, “Search and recovery of aircraft parts in ice-sheet crevasse fields using airborne and in situ geophysical sensors,” *Journal of Glaciology*, vol. 66, no. 257, 2020.
- [65] K. Iagnemma and S. Kang, “Multi-sensor terrain estimation for planetary rovers,” *8th International Symposium on Artificial Intelligence, Robotics, and Automation in Space*, 2003.
- [66] Government of Canada, “Hourly Data Report for Matagami,” [https://climate.weather.gc.ca/historical\\_data/search\\_historic\\_data\\_e.html](https://climate.weather.gc.ca/historical_data/search_historic_data_e.html), Accessed: 2020-08-10.
- [67] S. C. Colbeck, K. A. Shaw, and G. Lemieux, “The compression of wet snow,” Cold Regions Research and Engineering Laboratory, Hanover, NH, Tech. Rep., 1978.
- [68] Z. B. Rivera, M. C. De Simone, and D. Guida, “Unmanned ground vehicle modelling in Gazebo/ROS-based environments,” *Machines*, vol. 7, no. 2, pp. 1–21, 2019.
- [69] B. Trease, R. Arvidson, R. Lindemann, K. Bennett, F. Zhou, K. Iagnemma, C. Senatore, and L. Van Dyke, “Dynamic Modeling and Soil Mechanics for Path Planning,” in *Proceedings of the ASME 2011 International Design Engineering Technical Conferences & Computers and Information in Engineering Conference*, 2011, pp. 1–11.
- [70] R. He, C. Sandu, A. K. Khan, A. G. Guthrie, P. Schalk Els, and H. A. Hamersma, “Review of terramechanics models and their applicability to real-time applications,” *Journal of Terramechanics*, vol. 81, pp. 3–22, feb 2019.
- [71] W. E. Larimore, “Canonical variate analysis in identification, filtering, and adaptive control,” in *Proceedings of the IEEE Conference on Decision and Control*, vol. 2. Publ by IEEE, 1990, pp. 596–604.
- [72] L. Ljung, *System Identification Theory for the User*. Upper Saddle River, NJ: Prentice Hall, 1999.

- [73] C. Kar and A. R. Mohanty, "Monitoring gear vibrations through motor current signature analysis and wavelet transform," *Mechanical Systems and Signal Processing*, vol. 20, no. 1, pp. 158–187, jan 2006.
- [74] G. S. Babu, A. Lingamurthy, and A. S. Sekhar, "Condition monitoring of brushless DC motor-based electromechanical linear actuators using motor current signature analysis," *International Journal of Condition Monitoring*, vol. 1, no. 1, pp. 20–32, 2011.
- [75] R. F. Stengel, *Optimal Control and Estimation*. New York, NY, USA: Dover Publications, Inc., 1986.